UNIVERSITY OF BELGRADE

FACULTY OF MECHANICAL ENGINEERING

Mohammad Sakib Hasan

ANALYSIS, MODELING AND OPTIMIZATION OF SOLAR-POWERED HIGH-ALTITUDE PLATFORM-STATION (HAPS)

Doctoral Dissertation

Belgrade, 2022

УНИВЕРЗИТЕТ У БЕОГРАДУ

Машински факултет

Mohammad Sakib Hasan

АНАЛИЗА, МОДЕЛИРАЊЕ И ОПТИМИЗАЦИЈА БЕСПИЛОТНЕ ЛЕТЕЛИЦЕ ЗА ВЕЛИКЕ ВИСИНЕ НА СОЛАРНИ ПОГОН

Докторска дисертација

Београд, 2022.

Examination Committee

Supervisor:	Dr. Jelena Svorcan Associate Professor University of Belgrade Faculty of Mechanical Engineering
Members:	Dr. Aleksandar Bengin Full Professor University of Belgrade Faculty of Mechanical Engineering Dr. Aleksandar Simonovic Full Professor University of Belgrade Faculty of Mechanical Engineering Dr. Ognjen Pekovic Associate Professor University of Belgrade Faculty of Mechanical Engineering Dr. Toni Ivanov Assistant Professor University of Belgrade Faculty of Mechanical Engineering Dr. Nikola Mirkov Research Associate University of Belgrade "VINČA" Institute of Nuclear Sciences − National Institute of the Republic of Serbia, Belgrade, Serbia
Date:	

Комисије за преглед, оцену и одбрану докторске дисертације:

Ментор:	др Јелена Сворцан ванредни професор Универзитет у Београду − Машински факултет
Чланови комисије:	др Александар Бенгин редовни професор Универзитет у Београду − Машински факултет др Александар Симоновић редовни професор Универзитет у Београду − Машински факултет др Огњен Пековић ванредни професор Универзитет у Београду − Машински факултет др Тони Иванов доцент Универзитет у Београду − Машински факултет др Никола Мирков научни сарадник Универзитет у Београду Институт за нуклеарне науке Винча
Датум одбране:	

Acknowledgment

I would like to express my sincere gratitude to my supervisor, Dr. Jelena Svorcan, for her guidance, patience and invaluable assistance in providing me with crucial advice and recommendations that helped me to complete this dissertation. It has indeed been a privilege to work under her supervision. My heartfelt thanks also go to the members of the dissertation committee for their careful assessment of my thesis and for their constructive feedback.

This dissertation could not have been concluded without the continued help of Dr. Aleksandar Simonovic, Dr. Slobodan Stupar and Dr Ljubodrag Tanovic. I would like to thank them very much for their encouragement throughout my studies. Also, thanks to all my colleagues from office “113” who supported me with tireless assistance and helpful suggestions.

The most important support is the day after day support, and for this I gratefully thank Mr. Hasan Teoman for all of his generosity, love and unconditional support throughout my studies. Thank you so much for always being there for me and believing in me even when I doubted myself.

Finally, I would like to thank my family, especially my parents, my brother and sister, my nieces and nephews for their prayers and support during all these years, and Jelena for her kindness and love.

Analysis, modelling and optimization of solar-powered high-altitude platform station (HAPS)

Abstract: High-altitude long-endurance (HALE) or High-altitude platform station (HAPS) are aircraft that can fly in the stratosphere continuously for several months and provide support to military and civilian needs. In addition, HAPS can be used as a satellite at a fraction of the cost and provide instant, persistent, and improved situational awareness. Solar energy is the primary source of energy for these types of unmanned aerial vehicles (UAVs). Solar panels mounted on the wing and empennage capture solar energy during the day for immediate consumption and conserve the remainder for use at night. The main challenges to the successful design of HAPS are finding an appropriate model to calculate airframe weight, materials for structural analysis, designing a wing and propulsion system so that they can be integrated successfully into a unique aircraft configuration and these problems need to be solved. Therefore, this thesis investigates /focuses on the concept of HAPS, optimization of the airfoil, wing design and aerodynamic analysis, experimental analysis of different materials used in the wing structure, structural analysis of the wing and design of novel optimized propeller. The topics covered in the chapters are mentioned below.

The first three chapters of this thesis deal with the introduction, review of available literature and previous relevant research, and background of existing high-altitude aircraft and their configurations. Then, in Chapter 4, the initial mission requirements, mission profile, basic characteristics of solar panels, rechargeable batteries, assessment of daily power consumption and battery mass as well as methodologies for the initial estimation of aircraft structural mass and wing loads are discussed.

Chapter 5 is dedicated to selecting and defining the appropriate airfoil by using potential flow model and the multi-criteria optimization process. The aerodynamic analysis of wings performed by computational fluid dynamics is shown in Chapter 6. Calculations of aerodynamic coefficients of the wing and the flow field around the wing are presented in this chapter.

Chapter 7 is dedicated to the structural design of high-performance slender wings. Tensile tests of a variety of 3D printed polymers and composite materials as well as the effect of ageing and heat treatment on the tensile properties of PLA are presented to investigate their mechanical characteristics. Structural analysis of the wing is presented in Chapter 8. Two different possible solutions of the aircraft's wing structure for high altitudes are presented and their performance is compared through static and modal analyses.

Chapter 9 deals entirely with the methodology for designing the optimal propeller intended for high-altitude unmanned aerial vehicles. Coupled aero-structural optimization was performed using a

genetic algorithm where input and output parameters and constraints were defined from a set of geometric, aerodynamic, and structural characteristics of the propeller. Finally, main conclusions are presented in chapter 10.

Key words: HALE/ HAPS, optimization, aerodynamic analysis, structural analysis, propeller design, 3D printed material, experimental analysis, composite material, solar cells

Scientific discipline: Mechanical engineering

Scientific sub-discipline: Aerospace engineering

UDC: 623.746-519(043.3)

АНАЛИЗА, МОДЕЛИРАЊЕ И ОПТИМИЗАЦИЈА БЕСПИЛОТНЕ ЛЕТЕЛИЦЕ ЗА ВЕЛИКЕ ВИСИНЕ НА СОЛАРНИ ПОГОН

Сажетак:

Беспилотне летелице за велике висине (ХАЛЕ, ХАПС) су авиони који могу да лете у стратосфери непрекидно неколико месеци и пружају подршку војним и цивилним потребама. Поред тога, ове летелице се могу користити и као економични сателити и обезбеђивати тренутни, стални и побољшани увид у дешавања на Земљи. Сунчева енергија је главни извор енергије овог типа беспилотних летелица. Соларни панели распоређени по крилу и хоризонталним стабилизаторима упијају сунчеву енергију током дана за тренутну потрошњу док се остатак чува за лет током ноћи. Основни изазови успешном пројектовању ХАПС летелица су изналажење одговарајућег модела за процену тежине летелице, материјала за структуралну анализу, пројектовање крила и погонског система који се могу успешно интегрисати у јединствену конфигурацију летелице и ови проблеми морају бити решени. Стога, ова теза истражује/је фокусирана на концепт ХАПС-а, оптимизацију аеропрофила, дизајн и аеродинамичку анализу крила, експерименталну анализу различитих материјала коришћених у структури крила, структуралну анализу крила и дизајн нове оптимизоване елисе. Теме обрађене по поглављима наведене су у наставку.

Прве три главе ове тезе баве се уводом, прегледом доступне литературе и претходних релевантних истраживања, као и прегледом постојећих ХАПС летелица и њихових конфигурација. Затим, у глави 4, разматрани су полазни захтеви и мисија, основне карактеристике соларних панела и пуњивих батерија, процена дневне потрошње енергије и потребне масе батерија, као и методологије за почетну процену масе конструкције авиона и оптерећења крила.

Глава 5 посвећена је одабиру и дефинисању одговарајућег аеропрофила коришћењем модела потенцијалног струјања и вишекритеријумског оптимизационог поступка. Аеродинамичка анализа крила спроведена методом прорачунске механике флуида приказана је у глави 6. Овде су такође приказани и прорачунати аеродинамички коефицијенти крила као и струјно поље око крила.

Глава 7 посвећена је унутрашњој структури високоперформантних витких крила. Описана су спроведена мерења затезних карактеристика различитих 3Д штампаних полимера и композитних материјала, као и ефекти старења и термичке обраде на механичке карактеристике 3Д штампаних епрувета. Структурална анализа крила представљена је у глави

8. Приказана су два различита могућа решења структуре крила авиона за велике висине и упоређене су њихове перформансе кроз статичку и модалну анализу.

Глава 9 се у целости бави методологијом пројектовања оптималне елисе намењене беспилотној летелици за велике висине. Овде је спроведена спрегнута аеро-структурална оптимизација помоћу генетског алгоритма где су улазни и излазни параметри и ограничања дефинисани из скупа геометријских, аеродинамичких и структуралних карактеристика елисе. Коначно, основни закључци дати су у глави 10.

Кључне речи: ХАЛЕ/ХАПС, оптимизација, аеродинамичка анализа, структурална анализа, пројектовање елисе, 3Д штампани материјали, експериментална анализа, композитни материјали, соларне ћелије

Научна област: Машинство

Ужа научна област: Ваздухопловство

УДК: 623.746-519(043.3)

Table of Contents

List of Tables

List of figures

1. Introduction

1.1 Subject and goal of research

A remotely controlled or self-piloted aircraft that may carry payloads such as cameras, sensors, and communications equipment as well as perform all flying operations (including takeoff and landing) without the use of a human pilot onboard is known as an unmanned aerial vehicle (UAV). The total market for unmanned aerial vehicles (UAV) is growing rapidly because of its wide range of applications and according to a new market analysis conducted by Research and Markets [1], the worldwide UAV market is expected to reach USD 58.4 billion by 2026 from 27.4 billion in 2021, growing at a compound annual growth rate (CAGR) of 16.4 per cent from 2021 to 2026. Figure 1-1 illustrates the market forecast of UAV.

Figure 1- 1: Market forecast of Unmanned Aerial Vehicle (UAV) [1]

It is hard to achieve a unique classification for UAVs since it differs between countries. There are many types of UAVs in operation around the world that can be classified depending on different parameters such as application, size, weight, mission, flight range, endurance, wing, etc. For example, Micro Air Vehicles (MAV) weighing less than 500 g to UAVs weighing more than 20000 kg. UAV categorization in the United States military is mostly based on a tier system. Tier I is for low-altitude and long endurance missions, tier II is for medium altitude long endurance missions, and tier III is for high-altitude long-endurance missions. They can also be distinguished according to their functions: tactical drones, strategic drones and combat drones (Unmanned Combat Air Vehicle UCAV). Moreover, the type of gear can also differentiate them: fixed-wing, rotary wings and hybrid

system. Based on application, the UAV industry has been divided into four categories such as military, commercial, government & law enforcement, and consumer. A detailed classification of UAV is presented in chapter three. The military segment of the UAV market is expected to increase at a compound annual growth rate (CAGR) of 9.0 percent from 2021 to 2026, growing from USD 12,760 million in 2021 to USD 19,641 million in 2026. The commercial segment of the market is predicted to grow at the quickest pace of 28.0 % during the forecasted period; this segment's growth may be ascribed to advances and breakthroughs in drone technology [1]–[5].

High Altitude Long-Endurance (HALE) is a form of unmanned aerial vehicle (UAV) that operates for extended periods of time at stratospheric altitude (over 17 km above sea level) which is capable of staying in the air for a couple of months to a whole year. HALE (high-altitude long-endurance) are intended primarily as Low-Earth-orbit satellites and their primary purposes also include surveillance, monitoring, communication, atmospheric and space measurements, etc. After Qinetiq's Zephyr 7's two-week flight in the stratosphere, HALE UAVs have gotten much attention and are being developed all over the world for use as low-earth-orbit satellites, with the advantages of being less expensive, closer to sea level, and being able to perform tasks with more flexibility. Aside from that, these UAVs have the ability to supply communications networks, including 5G, as well as providing other services like surveillance, weather research and forecasting, environmental monitoring, and so on. Airbus recently conducted an 18-day flight in the stratosphere, 23 km above the surface, to test the 'High Altitude Platform Station' (HAPS) UAV. According to Airbus, the test was conducted in collaboration with NTT DOCOMO, a Japanese mobile provider. It could one day lead to super-fast broadband in rural places without the need to launch a fleet of satellites into low Earth orbit. It included an onboard radio transmitter that allowed it to imitate future systems that will convey internet signals between the UAV and a computer by providing a datalink [6]. Solar cells are now the only method to reach ambitious goals such as extended endurance or continuous flight. Photovoltaic cells would absorb solar energy throughout the day to power the engine and electronics, as well as store enough energy to fly in the dark or through clouds.

Although much investigation has already been performed on HALE UAV, many challenges still remain to be solved. The subject of the thesis is not only aerodynamic or structural analysis of drone components for high altitudes but a multidisciplinary, coupled process of analysis, modelling and optimization of the aircraft, which includes optimal mass ratio, optimized airfoil and wing of the aircraft as well as the propeller, the lightest wing structure (made of composites, plastic parts and high tech film-Mylar) as the basic lifting surface, the estimation of daily power requirements, fluid-structure interaction analysis, modal analysis of wings etc.

1.2 Brief history of high altitude and solar powered aircraft

Using solar power to sustain the aircraft has been a part of interest for aviation enthusiasts for the past four decades. However, the first-ever photovoltaic cell was demonstrated by Edmund Becquerel way back in 1839. He experimented with electrolytic cells and found that these cells create electricity when they are exposed to light and this is the main basis of all solar technology. The first photovoltaic (PV) cell capable of harnessing the sun rays to power "everyday electrical devices" was invented by Daryl Chapin, Calvin Fuller, and Gerald Pearson in 1954, marking a significant leap in solar technology [7]. The efficiency of the first photovoltaic cell, which was invented in the Bell Labs, was 4 % and later achieved 11 % efficiency [8]. However, the efficiency of solar cells has gradually improved over the past few decades. More details on solar cells, their working principle and efficiency are presented in chapter 4.

On November 4, 1974, at Camp Irwin, California, the first-ever solar-powered flight took place. The aircraft, designed by Astro Flight Inc. and named Sunrise I, flew for 20 minutes at an altitude of 100 m during the flight [9], [10]. The Sunrise I had a wingspan of 9.8 m, 4.4 m in length, a wing area of 8.4 m^2, and a gross weight of 12.3 kg. Sunrise I was later able to fly for more than three hours, but the aircraft's career ended after it was damaged in a sandstorm. The company later built Sunrise II, which was built and tested on September 12 1975, weighed 13 % less than the previous version (10.2 kg) and was able to output more power in comparison to the Sunrise I. Sunrise II was able to deliver 600 [W] compared to Sunrise I which delivered 450 [W], thanks to their 14% efficiency. The Sunrise II was expected to reach 15.2 [km] but only reached 5.2 [km] because the command-and-control system failed. As a result, the aircraft was severely damaged and the test flight program was terminated. Five years later, the solar panels of the Sunrise II were removed and attached to the Gossamer Penguin, another manned, solar-powered airplane. Regardless, the history of solar flight was enacted, and the first demonstration was carried out [11], [12]. Figure 1-2 depicts the historic flight of the Sunrise II in 1975.

Figure 1- 2: The Sunrise II demonstration (1975) [12]

AeroVironment, Inc. (founded in 1971 by ultralight airplane pioneer Dr Paul MacCready) has been experimenting with solar-powered aircraft since 1980, frequently in collaboration with NASA's Dryden Flight Research Center in Edwards, CA. They completed a crossing of the English Channel with the human-powered Gossamer Albatross on June 12, 1979, after demonstrating sustained and maneuverable human-powered flight with the Gossamer Condor on August 23, 1977. Following these successes, Dupont backed Dr. MacCready's attempt to modify a smaller Gossamer Albatross, called Gossamer Penguin, into a man carrying a solar plane. R.J. Boucher of Astro Flight Inc. served as a key consultant on the project. They provided the motor and the solar cells that were taken from the two damaged versions of Sunrise. On May 18 1980, the Gossamer Penguin, with 13 years old MacCready's son Marshall on board, realized what can be considered as the world's first piloted, solar-powered flight.

Figure 1- 3: Gossamer Penguin and Gossamer Albatross [13][14]

On the other hand, the Gossamer Penguin was not safe for a pilot flying higher than a few feet off the ground. The Gossamer Penguin's success inspired the Dupont Company to fund MacCready's development of a new solar plane that could cross the English Channel. The Solar Challenger was a high-wing monoplane with a 14.2 m wingspan and 16128 solar cells that produced 2500W at sea level. On July 7, 1981, it flew in 5 hours 23 minutes from Puntoise-Cormeilles near Paris to Manston RAF Base near London, covering 262.3 kilometers at a mean speed of around 49 [km/h] with solar energy as its primary source of power and no onboard energy storage device [13][15].

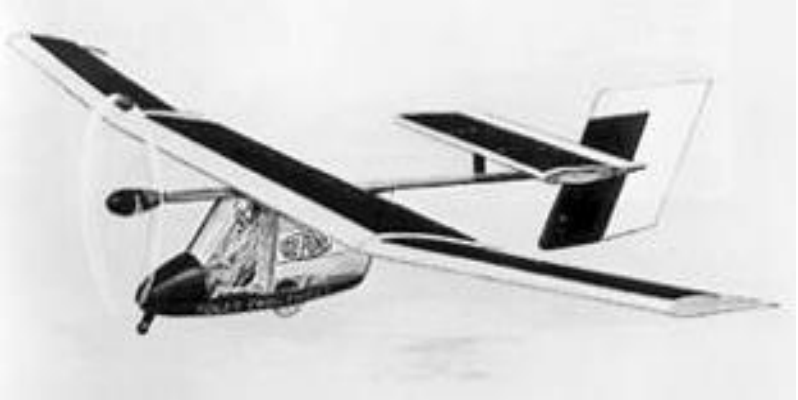

Figure 1- 4: Solar Challenger [14]

In late 1993, NASA-industry alliance created the Environmental Research Aircraft and Sensor Technology (ERAST) project funded by the United States (US) government, AeroVironment, to further mature Gossamer Penguin and the Solar Challenger. The ERAST program's main goals were to develop UAV capabilities for flying at extremely high altitudes and for long periods of time, demonstrate payload capabilities and sensors for atmospheric research, address and resolve UAV certification and operational issues, demonstrate UAV utility to scientific, government, and civil customers, and foster the growth of robust UAV industry [14].

The Pathfinder, a flying wing with a wingspan of roughly 30 m and six battery-operated electric motors, was the first-generation HALE vehicle. The landing gear, batteries, instrumentation system, and flight control computer were all housed in two underwing pods on the vehicle. Pathfinder established a solar-powered altitude record of 15.4 km at the DFRC on September 11, 1995, with the addition of solar cells covering the whole upper surface of the wing. The Pathfinder was transported to the US Navy's Pacific Missile Range Facility (PMRF) on the Hawaiian island of Kauai after further upgrades. The Pathfinder set a new altitude record for solar-powered flight in the spring of 1997, reaching 21.5 kilometers.

The Pathfinder Plus was the ERAST project's second-generation solar-powered airplane. The Pathfinder Plus's wingspan was 36.9 m with a longer center section and two sections on each side of

the center section. The Pathfinder Plus's final flight at the PMRF on August 6, 1998, set a new altitude record of 24.4 km. Furthermore, the Pathfinder-Plus was powered by eight electric motors, two more than the preceding Pathfinder model. The motors are marginally more efficient than the original Pathfinder motors because they were designed for Centurion.

Figure 1- 5: Pathfinder and Pathfinder-Plus [14]

Centurion, like its predecessors Pathfinder and Pathfinder-Plus, is a solar-powered and remote-controlled flying wing that demonstrated solar energy technology for long-haul flights at high altitudes. It was promoted as a technology demonstrator for a future fleet of solar-powered aircraft that may stay in the air for weeks or months on scientific sampling and imaging missions or as telecommunications relay platforms. The original ERAST objectives were to build two airframes: one to demonstrate a Centurion high-altitude (30.5 km altitude) mission and the other to demonstrate a Helios long-endurance (96 hours at 15.24-km altitude) mission. The Centurion had a wingspan of 63.1 m, nearly double that of the Pathfinder. The Centurion made three demonstration flights utilizing battery power at low altitudes at NASA's DFRC in late 1998 to verify the design's handling qualities, performance, and structural integrity.

Figure 1- 6: Centurion During its Low Altitude Flights and HP01 High-Altitude Configuration[16]

NASA and AV concluded in early 1999 that the best approach to proceed was to use a single airframe to demonstrate both of the ERAST aims due to a limited budget that could only fund one aircraft. Based on this proposal, the Centurion was converted from a 5-wing panel to a 6-wing panel aircraft and to demonstrate the ERAST goal of sustained flying approaching 30.5 km by replacing the center wing panel with two new stronger center wing panels and adding a fifth landing gear. The wingspan was enlarged to 75.3 meters as a result of this alteration. The aircraft's 14 electric motors were retained, with the four center motors being relocated to the new center wing panel. The aircraft's designation was changed from Centurion to Helios Prototype due to these changes, making it the fourth configuration in the series of solar-powered flying wing demonstrators. At the PMRF on August 13, 2001, the high-altitude prototype Helios HP01 achieved a world record for continuous horizontal flight by a winged aircraft reaching an altitude of 29.5 kilometers. Unfortunately, on June 26, 2003, the long-range prototype Helios HP03 was destroyed during a flight test at the PMRF due to turbulence and structural failure [17][15].

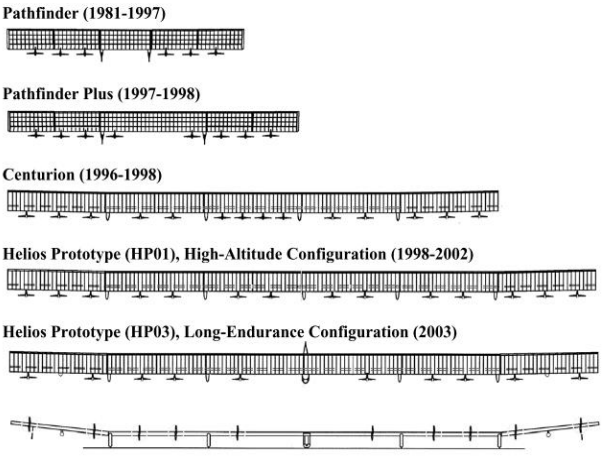

Figure 1- 7: Solar airplanes evolution through ERAST project [15]

In Europe, many projects were also conducted and one of them was the Helipat project. It was the first European, very-long endurance, stratospheric unmanned aerial vehicle (UAV). The Helipat project, which ran between January 2000 and March 2003, aimed at designing an integrated network based on HALE (High Altitude Long Endurance) unmanned solar platforms. The target of the project was to study the feasibility of a solar-powered high-altitude platform of 73m wingspan and 750 kg named Helipat, which can remain aloft for an extremely long period (approximately nine months). There were eight brushless motors, a twin-boom tail, and two rudders on this monoplane. The Helipat was planned to fly at altitudes ranging from 17 to 25 kilometers in the stratosphere, with the goal of delivering information aid services in the Mediterranean Sea region. The project brought together eleven European partners and resulted in the fabrication of a scale model of the structure with a

wingspan of 24 m. Due to a lack of funding, only a tiny portion of the research was accomplished, although a scale-sized solar-powered prototype was built [18][19][20].

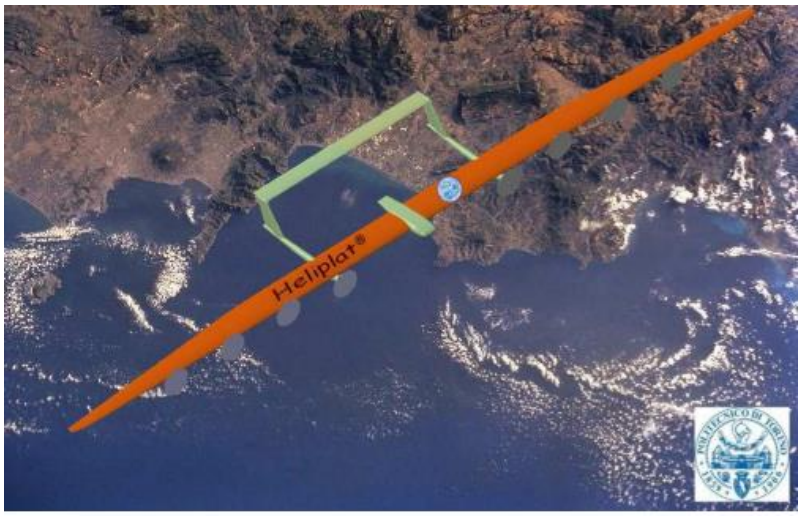

Figure 1- 8: A concept photo of Helipat [14]

AC propulsion is a small R&D and manufacturing company established in 1991, specializing in electric drives and vehicles. The SoLong was funded by the founder and chief engineer of AC propulsion Alan Cocconi. The company's main goal was to produce a small, cheap and rugged UAV that could fly for several days by solar power. The SoLong was a one-of-a-kind electric-powered platform that could be used for a range of remote sensing applications. It was a realistic alternative to other available UAVs due to its moderate size, silent and clean electric propulsion, and GPS navigation. Some of the key specifications of the SoLong were: wingspan- 4.75m; mass- 12.8kg, battery mass- 5.6kg [Sanyo 18650 lithium-ion (Li-ion) batteries with 220 Wh/kg], Max motor power- 800W. The SoLong has flown for several hours at night and landed with only runway marker lights in gusts of up to 48 km/h. On June 1-3, 2005, SoLong flew nonstop for 48 hours and 11 minutes, showing the viability of solar-powered flight [21].

Figure 1- 9: Alan Cocconi with SoLong in California [21]

The Solar Impulse idea was born in the early morning of March 21 1999, when Bertrand Piccard flew 20 days nonstop around the world in a balloon. The idea was supported by the Swiss Federal Institute of Technology (EPFL) with the goal of flying around the world in a solar-powered airplane on November 28 2003 [22]. The first prototype Solar Impulse 1 (*Si1)* which was designed to fly continuously was finally unveiled in front of 800 people in Dübendorf, Switzerland, on June 26 2009. The Si1 had a wingspan of 63.4 m (same wingspan as an Airbus A340) and weighed around 1600 [kg]. It was powered by four 7.45 [kW] electric engines, 11628 solar cells distributed mostly on the wing and horizontal stabilizers were the main power sources for the engines [23]. June 7 2012, was a historic day of this project as Solar Impulse 1 landed in Rabat (Morocco) after 19 hours airborne and became the first intercontinental flight in a solar plane. On April 23 2013, Si 1 started its Across America mission and flew over San Francisco's iconic symbol: The Golden Gate.

Figure 1- 10: Flight demonstration of Si 1 over the Golden Gate, San Francisco [22]

The second-generation Solar Impulse Si 2 airplane flew five consecutive days and nights and landed in Nanjing on April 21 2015. Bertrand Piccard and André Borschberg completed the 2015-2016 First Round-The-World Solar Flight after setting eight world records with the Solar Impulse prototype, which became the first solar airplane to fly across two continents, and across the United States. On April 24 2016, after three days and two nights, Solar Impulse 2 crossed the Pacific from Hawaii to San Francisco. The first Atlantic solar flight was achieved on June 23 2016, by crossing the Atlantic from New York to Seville [22].

Figure 1- 11: Solar Impulse was welcomed by the Swiss and Iberian colored smoke of the Spanish Air Force team [22]

The Zephyr project began in 2001 to film an attempt to break the world altitude record in a balloon, and the UAV's development has continued since then. Zephyr 2, a proof-of-concept aircraft weighing less than 7kg that could fly in both free and tethered modes, was launched in 2001. Following this successful first research, the program progressed, and in 2002, the Zephyr 3 UAV, measuring 12 meters in length and weighing 15 kilograms, was launched. It was planned to fly tied to a manned balloon seeking a world record height of 40.2 km, but due to a technical issue with the balloon, neither the balloon nor the aircraft flew. The Zephyr 4 had the same wingspan as the previous model, but it weighed around 17kg and was designed to be launched using a helium balloon. Zephyr 4 performed a test flight in Woomera, South Australia, in February 2005, where it flew for an hour after being launched at 9.1 km by the balloon. The Zephyr 5 project, which comprised two aircraft, the Zephyr 5-1 and Zephyr 5-2, continued the risk reduction and development efforts. Apart from the power supplies, both aircraft were identical. Zephyr 5-1 used both battery and solar power (weighing 31kg) and Zephyr 5-2 used only battery power (25kg). Because Zephyr 5-2 only had primary non-rechargeable batteries, it could only fly for one night. The two aircraft flew for four and six hours, respectively, in December 2005 in New Mexico, proving successful ground launch, ascent, cruise, and descent. The two aircraft were flown again in the United States in July 2006, with Zephyr 5-1 reaching 11000 m after an 18-hour journey that included a 7-hour overnight flight. The two airplanes have a total flight time of 35 hours [23].

The Zephyr 6 weighed less than 30 kg and had an 18-meter wingspan. It was built of ultra-light carbon fiber. The Zephyr 6 flew for 54 hours in New Mexico in July 2007, achieving a maximum height of

17.7 kilometers. The Zephyr 6 flew for 87 hours in Yuma, Arizona, in August 2008, achieving a maximum height of 18.3 kilometers. In July 2010, the Zephyr UAV set three world records. On July 9, 2010, the Zephyr 7 was launched for flight testing and lasted aloft for 14 nights (336 hours 21 minutes) at the height of 21.56 km over the Yuma Proving Ground in Arizona and it landed on July 23, 2010.

The Zephyr program was purchased by Airbus's high altitude pseudo-satellite (HAPS) program in 2013, which had been under development since 2008. Airbus claims it bridges the gap between satellites and unmanned aerial vehicles by running entirely on solar power and flying at high altitudes above the weather and regular air traffic. Airbus announced the beginning of the Zephyr 8 (Zephyr S) program on April 23, 2014, to build the next generation Zephyr unmanned aerial system (UAS). Figure 1-12 shows all the Zephyr projects from 2001 to 2014.

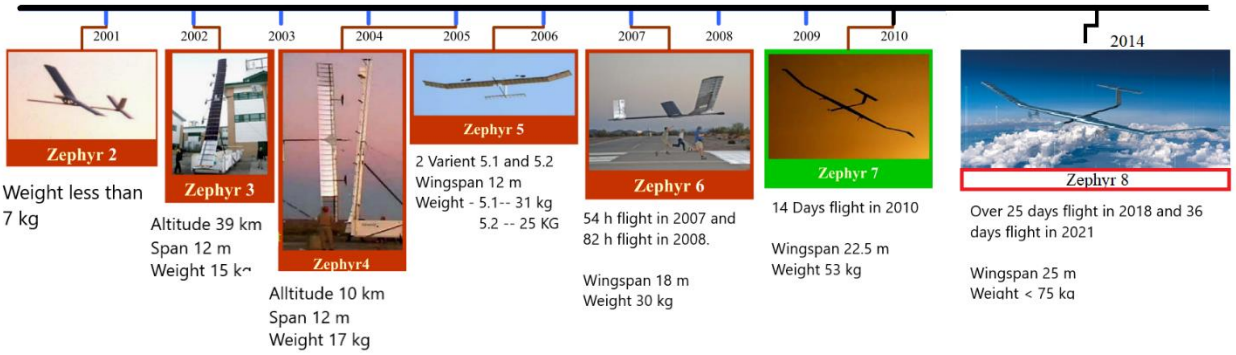

Figure 1- 12: The evolution of Zephyr project [15][24], [25]

In July 2018, the Kelleher facility, a Zephyr S HAPS serial production line near Farnborough, was launched, where the first production examples were built. In the same month, Zephyr 8 (wingspan 25 m and weight less than 75 kg), the first production aircraft, took to the skies for the first time, setting a new world record for flight endurance of over 25 days. In October 2021, Zephyr S achieved 36 days of stratospheric flight across two 2021 flights, proving Zephyr's status as the only HAPS able to perform at length in the stratosphere and also set a new world record for absolute altitude for this class of UAV at 23.19 km [24], [26][27][28][28].

The Defense Advanced Research Projects Agency (DARPA) is a United States Department of Defense research and development agency in charge of developing new technologies for military application. One of their projects was The Very high altitude, Ultra-endurance, Loitering Theatre Unmanned Reconnaissance Element (Vulture) Program [30]. The purpose of the Vulture program was to develop a high-altitude airplane with the ability to remain in flight for five years, with a

payload of 454 kg, which consumes 5kW. This platform would be employed in Intelligence, Surveillance and Reconnaissance (ISR) and communication missions.

The program's initial phase began in 2008 with conceptual investigations that lasted 12 months. This phase was awarded to three companies: Boeing (3.84 million dollars), Lockheed Martin (4.27 million dollars), and Aurora Flight Sciences (3.64 million dollars). The second phase (Risk Reduction Demonstration — RRD) began in 2012 and involved the development of a subscale vehicle as well as the demonstration of a three-month flight. For the second phase, three firms presented concepts for solar aircraft. Aurora's design is named "Odysseus," and it uses solar energy during the day and stored solar energy at night to power the plane. The Odysseus from Aurora takes a "modular shuttling" method, employing three UAVs with 49-m wingspans that can dock and detach in the air. This facilitates take-off and altitude flying while also giving choices in the event that one of the three vehicles has to be recalled for maintenance or replaced. Odysseus will stay in the air thanks to solar power and fuel cells, and the three-vehicle design can switch from a Z-shaped configuration to absorb more sunlight during the day to a straight wing configuration for reduced drag at night. With the 122 m wingspan SolarEagle and an 89-million-dollar contract, Boeing won the second phase with the 122 m wingspan SolarEagle. The maiden flight was supposed to take place in 2014. For Phase 2 of the Vulture Program, DARPA estimated a budget of 155 million dollars [29].

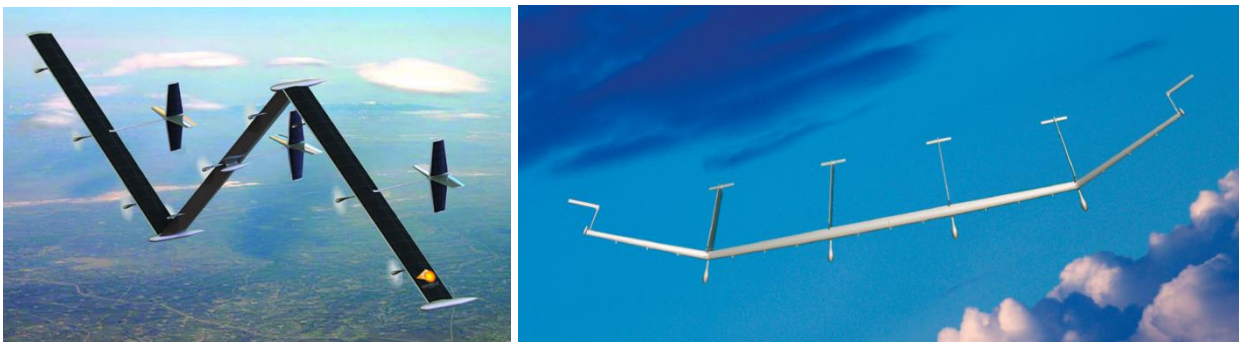

Figure 1- 13: Proposals for Phase 2: Boeing (SolarEagle), Lockheed Martin, Aurora Flight Systems (Odysseus) [29]

SolarEagle research was halted in 2012. The Vulture Program was reorganized to focus solely on solar energy (Photovoltaic Cells) and energy storage (RFC) technologies. There is no current information regarding the Vulture Program or the SolarEagle Project [30].

Solara 50 UAV was unveiled by Titan Aerospace at the Association of Unmanned Systems International (AUVSI) conference and exhibition held in Washington in August 2013. The aircraft had a wingspan of 50 m and a total weight of 159 kg, with 32 kg payload. It is expected that the Solara 50 will be capable of flying at 20 km for up to 5 years.

Figure 1- 14: Solara 50 [31]

In May 2015, the prototype of the Solara 50 was destroyed in an accident on its first flight, shortly after takeoff, in a test area in New Mexico, US. Although the accident was caused by structural failure of the wing due to airflow (thermals) at low altitude, Google announced that it will continue the development of the Solara 50.

In March 2014, Facebook announced the purchase of the British company Ascenta, a Somerset, England-based company with staff that participated in the development of Zephyr at QinetiQ, in a deal valued at 20 million dollars. The Aquila UAV, developed by Facebook's Connectivity Lab, is a flying wing with a wingspan of 42 m and a total weight of about 400 kg. The aircraft has four propellers driven by electric motors, with power supplied by solar cells during the day and rechargeable batteries at night. On June 28th, Aquila completed the first successful flight in Yuma, Arizona. The initial plan was to fly Aquila for 30 minutes, but things went well and it ended up flying for 96 minutes. During landing, however, the plane came to a stop short of the planned landing zone, causing structural damage [32]

Figure 1- 15: The Facebook Aquila [25]

Following the crash, the prototype Aquila was upgraded with spoilers, propeller feathering capability, and external surface refinement; the second flight took place on May 22, 2017, and the one-hour, 46-minute flight was deemed successful. The Aquila and the "high altitude platform station broadband connectivity system" (HAPS) project were launched in November 2017 as part of a collaboration with Airbus. In the same month, the Victoria & Albert Museum announced that Aquila will be included in the spring 2018 "The Future Starts Here" exhibition [32]. As aircraft manufacturers began to design and build HAPS, Facebook decided to halt its program to collaborate with partners like Airbus on HAPS connectivity and technologies such as flight control and high-density batteries in June 2018. Facebook and Airbus have scheduled test flights in Australia utilizing the latter's Zephyr drone technology, according to reports from 2018. Zephyr is similar to Aquila in that it is powered by solar energy [32].

The BAE Systems Persistent High Altitude Solar Aircraft (PHASA-35) is a HALE unmanned aerial vehicle (UAV) made in collaboration with Prismatic. The aircraft, which can stay aloft for up to 12 months and is designed as a cheaper alternative to satellites, may be used for surveillance, border control, communications, and disaster assistance. Engineers from BAE Systems and Prismatic started development on the plane in 2018, with a first flight scheduled for 2019. A quarter-scale model known as the PHASE-8 has already conducted a successful first flight in 2017. BAE Systems purchased Prismatic as a subsidiary in September 2019 [33] .

Figure 1- 16: The Phasa-35 full-scale prototype is being tested at Wharton [34]

The aircraft flew for the first time on February 17, 2020, at the Woomera Test Range in Australia, after less than two years of development with support from the UK's Defence Science and Technology Laboratory and the Australian Defense Science and Technology Group. More trials began, and the aircraft completed an endurance test while carrying a sensor payload in October 2020. The aircraft

was put through its paces for 72 hours while in a simulated stratospheric environment [26]. Following "strong increasing interest" in the aircraft from across the US Department of Defense and federal agency customer base, BAE Systems announced intentions to conduct a flying demonstration in the United States in January 2021 but it was cancelled due to bad weather [34].

1.3 Starting hypotheses

The previous section demonstrates just how challenging, costly and ambitious task is the development of a HAPS. Numerous well-developed companies and research institutes tried, and some of them even failed. Therefore, the study and modeling of high-altitude unmanned aerial vehicles necessitates a wide range of statistical and numerical models, optimization approaches, and experimental methodologies, as well as their mathematical foundations. The following are the beginning points for the research:

- Certain properties of the drone subsystem (e.g. mass, aerodynamic characteristics, or structural response) are estimated using statistical models and different prediction approaches;
- For optimizing the wing airfoil as well as the propeller blades, two-dimensional flow considerations as well as simpler flow models (e.g. potential flow model corrected by semi-empirical corrections) are considered as starting point;
- The spatial flow of wings in the stratosphere is accurately depicted using computational aerodynamics and current turbulent models based on Reynolds averaging of the Navier-Stokes equations and the concept of isotropic turbulence;
- For flow issues and structural analyses of aircraft elements, metaheuristic and evolutionary optimization methods can be utilized;
- The finite element technique is used to show the behavior of the wings under the influence of aerodynamic loads with adequate precision;
- Numerical experiments provided a variety of usable results and can significantly speed up and improve further design phases (detailed design), as well as future experimental research,
- The results of experimental testing of material characteristics served as a good basis for a detailed analysis of the behavior of aircraft structures.

1.4 Scientific research methods

The scientific methods that are applied within the dissertation are as follows.

Inductive and statistical approaches are used to present some broad findings after evaluating and systematizing the available literature and the data obtained thus far.

Then, these conclusions were further applied by deductive methods to the individual case of a HA unmanned aerial vehicle as well as to its subsystems. The numerical study of the flow around the wing and its structural behavior is divided into discrete, simpler cases that are solved independently utilizing analysis and synthesis methods.

Following that, using the principles of concretization and generalization, an integral (coupled) numerical computation was done. The complex problem of unmanned aerial vehicles for high altitudes is simply described by description methods, and then modeled by various mathematical (statistical), numerical (e.g. finite volume method and finite element method) and experimental methods.

The achieved numerical results are verified in relation to the available experimental and numerical data of other authors using comparative methods. The process of selecting the final (optimal) solution is carried out using different (evolutionary, metaheuristic) optimization methods (in particular; genetic algorithm).

1.5 Achieved scientific contribution

As this is an extremely modern, ambitious and multidisciplinary scientific research topic, it is possible to formulate the following achieved scientific contribution of this dissertation:

Developing an appropriate preliminary design for a drone that can fly at high altitudes and for a long time using solar power, which includes:

- Accurate estimation of aircraft empty mass based on different weight estimation models used for solar-powered aircraft;
- Implementation of detailed and validated numerical calculations of the flow around individual components (airfoils, wings, propellers);
- Conducting various optimization analyses;
- Improving the aerodynamic efficiency of the lifting surfaces of the aircraft for high altitudes;
- Carrying out detailed and validated numerical calculations of the behavior of the high aspect ratio wing structure of the aircraft for high altitudes;
- Selection of appropriate materials after conducting numerical and experimental studies.

1.6 Research plan and work structure

Following a thorough examination of the available bibliographic units that serve as references for the subject area of high-altitude unmanned aerial vehicle research, systematization of analytical, numerical, and experimental approaches and results is carried out, along with the classification of the presented guidelines for future research.

Further research plan was classified into the following main chapters:

Chapter 2: A review and standardization of the current scientific literature on unmanned aerial vehicles at high altitudes;

Chapter 3: Background and overview of existing high-altitude aircraft and their configurations;

Chapter 4: Breakdown of the conceptual design of the high-altitude aircraft into phases;

Chapter 5: Airfoil selection through XFLR5 and by defining (multidisciplinary, multicriteria) optimization problems, as well as developing, implementing, and deploying optimization techniques;

Chapter 6: Wing design and aerodynamic analysis;

Chapter 7: Wing structural design and experimental study of selected materials;

Chapter 8: Fluid Structure Interaction analysis and modal analysis of wings;

Chapter 9: Propeller blade design through optimization and blade structural analysis;

Chapter 10: Discussion with conclusions and recommendations for future research.

2. Review of available literature and previous relevant research

Many studies have been conducted in order to build this novel type of aircraft. Some researchers focused on the aircraft's aerodynamics, which is one of the most important design variables for developing any new UAVs, while others focused on the propeller's performance and the entire UAV design, particularly solar energy. However, having a larger picture of all the HALE UAVs that have been built to date is crucial. A very clear and useful overview of the different types and purposes of high-altitude unmanned platforms is given in [35]. Despite their development began in the 1990s, the majority of technical advancements have happened in the recent ten years, as huge corporations whose primary business is dependent on worldwide communication have begun to show an increasing interest in their growth and improvement. Although their relatively standard configurations (most resembling sailboats or balloons), they face a number of challenges during the design process (some are: the need for terribly low mass; very high aspect ratio; aeroelastic structures exposed to increased radiation; aerodynamic shapes of the UAV for the stratospheric region and low Reynolds numbers; new concepts of propulsive system; photovoltaic cells as efficient as possible; planning and achieving the mission of the aircraft; safe operation of the aircraft, etc.). As a result, as demonstrated by the number of doctorates published throughout the world, a thorough and comprehensive approach to this issue is necessary [35][36].

Such complex flying systems require the simultaneous consideration of a number of diverse disciplines, especially aerodynamics and structural analysis. Estimation of vehicles empty weight is one of the main tasks at the preliminary stage of aircraft design. Gudmundsson[37] described how to calculate the empty weight by using historical data of sailplane. D.W. Hall described the first method of defining a good structural weight or empty weight model in NASA contactor report [38]. W. Stender proposed another method in 1969 based on statistical data for sailplane with twin boom tail which was later adopted by Rizzo [39]. Two kinds of prediction were adopted by Rizzo in his paper. A. Noth [13] created a database by using both Stender's and Rizzos's model and then proposed a new empirical model which is mainly effective for very light solar-powered UAV model. The development of a software platform for the conceptual design of high-altitude spacecraft is described in [40]. Although it is an excellent tool of satisfactory reliability, the models used are simple (e.g. the flow model is based on potential flow) and provide the possibility of further improvement. Some useful data on the capabilities (and limitations) of one of the first successful flying wing type aircraft are given in [16], while in [16][41]descriptions of optimization procedures performed to increase aerodynamic efficiency or decrease mass of the wings can be found, respectively.

The papers [42]–[45] primarily deal with the optimization of the shape of the airfoil and / or the high aspect ratio wing aircraft for high altitudes, by multi-criteria optimization procedures based on panel methods of computational fluid mechanics. For this purpose, it is necessary to adopt an adequate way of describing the geometry of the wing that allows a large number of repetitions of the calculation as well as to form an appropriate iterative optimization procedure. As the result of multi-criteria optimization is usually a set of optimal solutions, the final choice of the best geometry strongly depends on the designer, as well as the purpose and working conditions of the aircraft. For this reason, for certain initial requirements, it is necessary to conduct optimization procedure that will help in selecting the most appropriate wing geometry (the basic element of the high-altitude aircraft that provides the lift).

The selection of appropriate materials to get low structural weight by not compromising the structural integrity is essential to increase flight endurance. In solar airplanes, complex composite materials with exceptionally lightweight characteristics have been used to provide outstanding mechanical qualities such as strength, torsion, flexion, and vibration. However, 3D printed plastic materials in certain airframe structures are also gaining popularity. Today, the aerospace industry contributes roughly one-fifth of revenue to the additive manufacturing industry [46]–[52].

The shape of high aspect-ratio wing experience significant deformation due to aerodynamic, gravitational and inertial loads as well as other sudden effects such as gust, turbulence etc. Interaction of fluid flow exerts forces on a solid structure during flight which generates deformation of wing [53], [54]. This phenomenon is known as fluid structure interaction (FSI). L. Zhang [55] discussed the impact of temperature and pressure in the flow field (simulated at various Mach numbers) on the natural properties of various aircraft wing materials by using 1-way FSI analysis. S. Son [56] used the loose coupling or one-way FSI analysis and Kriging method to find the optimized shape of a high-aspect ratio wing. Z. Qu [57] analyzed the aeroelastic response of a high-altitude propeller by using the loose coupled or 1-way FSI method.

On the other hand, considerable attention needs to be paid to the design of the propeller of a high-altitude aircraft whose main purpose is to provide sufficient thrusts. Again, the operating conditions of these rotating surfaces are quite specific. The air density at an altitude of 20 km is almost 14 times lower than the one at zero altitude, while the cruising speed of these aircraft is low (so the advance ratio is low). The optimization procedure can also be performed to find the best propeller geometry, as shown in [58][59].

3. Background and overview of existing high-altitude aircraft and their configurations

The history of unmanned aerial vehicles (UAVs) dates back to 1916, when Elmer Sperry of the Sperry Gyroscope Company (together with Peter Hewitt) created an automatic control system for the Curtiss Flying Boat. Following the United States' entry into WWI in 1917, moneys was made available to create a flying bomb and the US Navy has placed an order for five bomber planes. After that, numerous UAVs have been built to date, and they can be classified into many types based on various parameters such as size, endurance, weight, and so on.

Micro UAVs (MAVs) are UAVs with a wingspan of less than 150 mm. They have a flight time of less than an hour and a weight around 10 grams, whereas mini-UAVs have the same flight time as micro-UAVs but can fly at a greater altitude and weigh between 500 g and 1 kg. Small UAVs are characterized by an endurance of a few hours, weighing between 2 and 10 kg, can fly for up to 2 hours and can fly at altitudes ranging from 300 to 1500 meters. These UAVs can only be launched by hand and must fly gently within buildings in urban areas [5].

Tactical drones (TUAV) are medium-range drones with a range of 100 to 300 kilometers and an endurance of ten hours. They fly at an altitude of less than 5,000 meters and have a range of 100 to 300 kilometers. Land and naval troops commonly employ these vehicles, which are utilized to assist military applications. Medium-range TUAVs act as communication relays. They aren't generally utilized in formation fleet flight, but they can work together as a team.

The MALE UAVs fly at an altitude of 5000 – 15000 m and have a 24-hour endurance. These types of drones are more focused on short-range missions. The American Predator, which was used to drop missiles in Afghanistan in 2001, is a well-known MALE drone.

The Hale UAVs fly at height of over 15 000 meters and can stay in the air for several days. HALE are the heaviest unmanned aerial vehicles (UAVs), weighing up to 12 000 kilograms. They are used in long-range tasks for the army, including as reconnaissance and surveillance. The American Global Hawk, is a well-known military UAV with 35 hours of endurance [3]–[5]. Table 1 represents the different types of UAVs that are designed till date.

Table 1 Classification of different types on UAVs [4], [5]

Class	Mass [kg]	Operating altitude [m]	Endurance[h]
Micro	< 0.01	<15	<1
Mini	0.5-1	<30	<1
Small	2--10	300-1500	0.5-2
Medium	45-450	3000-4500	3--10
TUAV	100-500	3000-9000	5--12
MALE	450-4500	5000-15000	20-40
HALE	>50	>15000	24+

Number of existing high-altitude long-endurance (HALE) or high- altitude pseudo satellite (HAPS) UAVs relevant to the present study in addition to the research activities carried out in the areas of structural and aerodynamic analysis are surveyed in this section. Most of the vehicles from this list are in operation either in defense or in the civil sector.

Table 2: Number of existing high and medium altitude UAVs

Aircraft	**Wingspan (m)**	**Gross Weight (kg)**	**Propulsion**	**Endurance**	**Service Ceiling (km)**	**AR**
Consumable fuel HALE						
Phantom Eye	46	4561	Hydrogen	4 days	19.8	n/a
Global Observer	79	1805	Hydrogen	7 days	19.8	n/a
RQ-4 Global Hawk	39.9	14628	Turbofan	32 h	18.28	25
Condor 1989	31.4	18500	Turbofan	80 h	21.30	n/a
Theseus	42.67	2495	Piston engines	30 h	18.2	n/a

MALE						
Bayraktar	12	650	Rotax 912	27 h	8.29	n/a
IAI Heron	16.60	1150	Rotax 914	52 h	10	19.9
MQ-1B Predator	16.8	1020	Rotax 914F	24 h	7.60	19
Solar powered HALE						
Pathfinder	30.00	252	6 electric motors	n/a	21.5	n/a
Pathfinder Plus	36.30	315	8 electric motors	15 h	24.4	15
Centurion	61.80	861	2 electric motors	14 h	26.82	26
Helios	75.30	930	14 electric motors	several months	30	30.9
Zephyr S	25	75	2 electric motors	25 days 23h	21.33	30.4
PHASA-35	35.00	150	2 electric motors	n/a	21.336	17.5

Table 2 represents some worth mentioning high altitude and medium altitude aircraft along with their wingspan, gross weight, propulsion system, service ceiling, endurance and aspect ratio. First seven UAVs are powered by consumable fuel and the remaining others are solar-powered aircraft. Information of solar powered aircrafts are collected from various websites which are already referenced in the previous section.

First seven drones from Table 2 are powered by several different types of engines which are in general four or six-cylinder modified piston types. The Phantom Eye was Boeing's concept to satisfy the US military's requirement for unmanned drones capable of sophisticated intelligence and reconnaissance operations, as a result of the fighting circumstances in Afghanistan. Thanks to its engine which employs liquid hydrogen as fuel, Phantom Eye has endurance of around four days [60]. Global Observer, which is also propelled through liquid hydrogen, can fly continuously for seven days. The

payload fraction of these two vehicles is about 10% and 5% of the overall weight, respectively. Boeing Condor is a close rival to the Global Observer and the Boeing Phantom Eye, although its endurance is only around 58 hours. It is powered by a six-cylinder opposed turbocharged liquid-cooled engine with two turbochargers. The Theseus aircraft was built and operated by Aurora Flight Sciences Corporation. The drone's wingspan was 42.67 m, and it was mostly made of composite materials. Theseus was planned to fly autonomously at high altitudes, with takeoff and landing under the active control of a ground-based pilot in a ground control station "cockpit." It was powered by two 59.65 [kW] turbocharged piston engines that drove twin 2.74 meters-diameter propellers. The RQ-4B Global Hawk has a significantly bigger payload than the other vehicles and has the greatest payload of any UAV. Its operational ceiling is about 18.28 kilometers. From Table 2, it is clear that hydrogen-fueled engines are the optimum propulsion choice for long endurance and high payloads. NASA research came to the same result, stating that among the engines examined for a future generation of UAVs, the liquid hydrogen internal combustion engine would give the most endurance [61].

Figure 3- 1: High- altitude long endurance drones: the Phantom Eye, the Global Observer, the RQ-4B Global Hawk, the Theseus aircraft by Aurora Flight Sciences Corporation [62][63][64][65]

Although Bayraktar, IAI Heron and MQ-1B Predator are not HA drones, they are in this list because of their long endurance ability. Bayraktar is a 6.5 m long Turkish medium-altitude long-endurance (MALE) unmanned combat aerial vehicle which has a blended wing body design with its inverse V-Tail structure. In June 2020, Bayraktar TB2 became the first domestically produced aerial vehicle in the country to accomplish the milestone of 200,000 operational flight hours [66]. The Heron is a strategic and tactical unmanned aerial system (UAS) with a Medium Altitude Long Endurance

(MALE) capability globally operated in both strategic and tactical operations for customers all over the world. The Heron can conduct operations for up to 45 hours at a height of 10.67 km. Heron is presently serving more than 20 global leading clients in a wide range of mission types, and it is robust and combat proven with hundreds of thousands of operational flight hours[67]. The MQ-1B Predator is a multi-mission, medium-altitude, long-endurance remotely piloted aircraft that is used primarily for information gathering and secondly for executing dynamic targets. It has a unique capacity to execute strike, coordination, and reconnaissance (SCAR) against high-value, fleeting, and time-sensitive targets due to its considerable loiter time, wide-range sensors, multi-mode communications suite, and precise weaponry [68].

Figure 3- 2: Mediul-altitude long endurance (MALE) drones: Bayraktar, Heron and MQ-1B [66][67][68]

3.1 HALE UAV configuration

The design of an unmanned aerial vehicle system, particularly the airborne element, is similar to that of a manned aircraft system in that it attempts to accomplish the required performance while maintaining the required integrity and dependability while minimizing life-cycle costs (i.e. cost of initial procurement plus the costs of operating it). As a result, the methods used to attain these goals are comparable and, for the most part, employ similar technology.

Many research works have been done till now to increase the aerodynamic efficiency or structural performance of HALE aircraft. One of the main groundworks was done by NASA using a multi-disciplinary optimization tool [69]. In the beginning, sixteen possible HALE UAV configurations were developed. Those were grouped in heavier-than-air (HTA) and lighter-than-air (LTA) concepts. UAVs from the both concepts were also classified into two groups; consumable fuel and solar-powered or solar regenerative aircraft. Each proposal was designed to focus on two distinct operational missions: hurricane science and communications relay. Each aircraft's weight was calculated using a combination of analytical and empirical approaches, with the weight of some of the components presumed constant. The amount of material that could sustain the expected loads was used to size the wing structure.

Concept 6 was the starting point for the solar powered aircraft. The all-wing design had roots in the AeroVironment family of solar-electric planes created before and during NASA's ERAST program (Pathfinder, Pathfinder Plus, Helios).

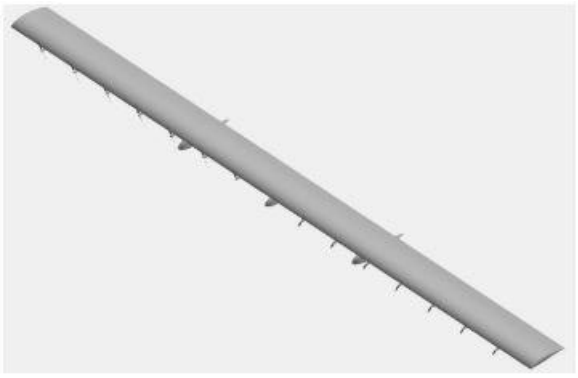

Figure 3- 3: Concept 6: All-wing configuration with solar powered propulsion system [61]

Although Concept 6 borrows significantly from Helios heritage, the vehicle size is much larger. Best overall performance of the design was obtained at the maximum allowed wingspan (100 m). Despite the large wingspan, the wing aspect ratio is relatively low compared to Helios.

The primary difference between Concept 7 – All-Wing Configuration with Solar Secondary Battery Propulsion and Concept 6 was the type of energy storage technology used. Instead of storing energy

in the form of H_2 and O_2, energy was stored in rechargeable batteries in Concept 7 (also referred to as secondary batteries). Li-S secondary battery energy storage was assumed for the remaining solar powered concepts due to the greater overall performance of the secondary batteries for the study missions and their simplicity.

Concepts 8–10 were an attempt to move beyond the Helios-like all-wing configuration and employ more unorthodox designs to overcome some of the acknowledged faults with previous HALE SR vehicles. The Helios design's high degree of flexibility was a well-known flaw. For the analysis of alternatives measures that were evaluated, Concept 8 (Trussed-Wing Configuration) did not indicate a benefit over the more traditional Concept 7 design. Both the communications relay mission and the hurricane science mission had a slim chance of succeeding. One disadvantage of the Concept 8 design is the truss structure's drag, which reduces aerodynamic performance.

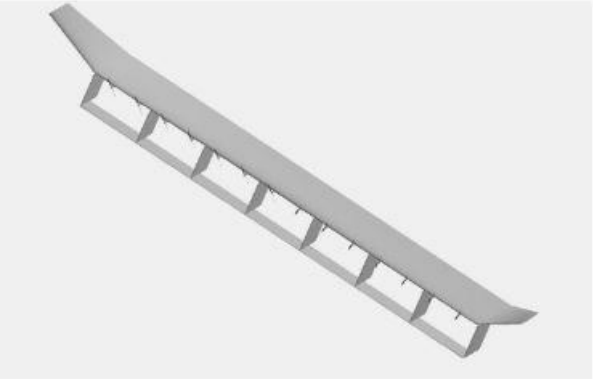

Figure 3- 4: Concept 8: Trussed-wing configuration [61]

Another unusual layout studied was concept 9, which was a joined-wing structure. In comparison to the all-wing arrangement, the joined-wing was projected to give increased structural rigidity and possibly a reduction in total structural mass. The joined-wing technique was also motivated by the desire to get a big quantity of solar array area in a smaller package. Figure 3-5 shows how the joined-wing method is implemented in an aircraft. Using the existing analysis tools to model this type of architecture necessitated a lengthy list of simplifying assumptions. Overall, the results for Concept 9 make it the least desirable SR concept.

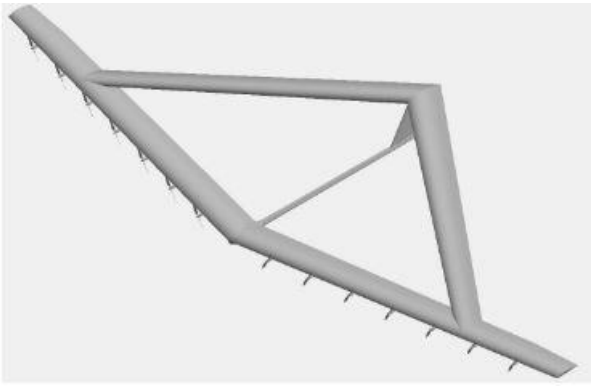

Figure 3- 5: Concept 9: Joined-wing configuration[61]

Concept 10 – Multi-Surface Configuration with Solar Secondary Battery Propulsion. Non-optimal array orientation reduces the amount of solar energy collected during the day. Concept 10 was created in an attempt to solve the problem of solar array orientation (see Figure 3-6). The primary idea behind this notion was to have arrays that re-orient themselves throughout the day and throughout the loiter pattern to optimize the solar energy collected (the arrays only vary in roll angle, not pitch and yaw). Auxiliary surfaces are employed in Concept 10 that are not meant to contribute to vehicle lift or control, but rather to be positioned for optimal energy collection. Unfortunately, the net impact of this kind of configuration is relatively small despite such a large improvement in solar energy collection.

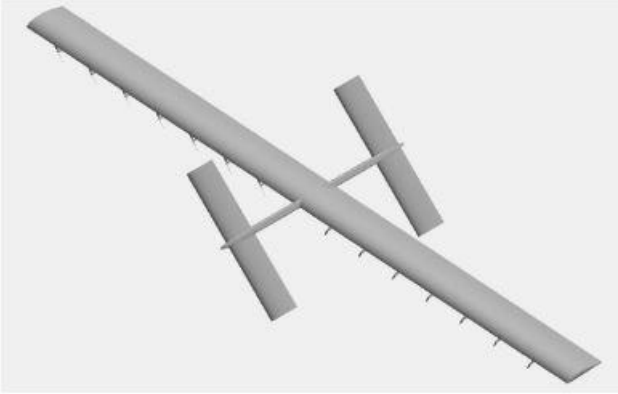

Figure 3- 6: Concept 10: Multi-surface configuration[61]

The overall study of different configurations of UAVs also showed that the characteristics of the storage system and the efficiency of the solar cells were key to enhancing the aircraft performance to meet the requirements [61].

HALE UAV ITB (Institut Teknologi Bandung) is being developed to meet the demand for a dependable autonomous vehicle that can monitor Indonesian country borders and natural resources and be controlled remotely from a ground station. ITB has a three-year development plan for the

HALE UAV, which is broken down into three parts. Figure 3-7 shows the first stage, which generated a 12 m wingspan prototype with four boom configurations and four electric propulsion systems for a flight altitude of roughly 6000 m.

Figure 3- 7: First generation of HALE UAV-ITB prototype 2 [70]

The first prototype experienced issues with side wind effect, which resulted in a large bending moment, destroying the wing. The second stage, which is presently under construction, will have a 16-meter wingspan and be able to fly at a height of 6000 m. Figure 3-8 shows the second prototype, which will use a single boom with twin electric motors, which will obviously be lighter than the four-boom design. Because the induced drag created is smaller, a greater wingspan indicates a larger aspect ratio, which should result in a spanwise lift distribution that is more akin to the rectangular lift distribution approach [70].

Figure 3- 8: Second prototype [70]

A conceptual design approach to design a basic geometry for a solar-powered HALE UAV was presented in [71]. The process was based on logical reasoning and analytical restraints, such as environmental considerations and structural limitations, to recommend the airplane geometry. The aerodynamics, flight performance, and power requirements during flight are then calculated using analytical equations with fractions to account for power losses in aircraft subsystems. The case study investigated the energy requirements of a rectangular braced-wing configuration, as shown in Figure

3-9, to carry a 100 kg payload. The results showed that this configuration is capable of year-round continuous flight at an altitude of 21.3 kilometers and up to 10° N latitude. Year-round flight at these latitudes, on the other hand, would necessitate a regenerative fuel cell unit with a 94 % efficiency.

Figure 3- 9: An artist's impression of the braced wing concept [71]

Rizzo and Frediani presented a study that defines a mathematical model for preliminary solar-powered aircraft design that is valid regardless of the aerodynamic arrangement. To imitate Helios, a preliminary investigation is carried out, and the results are compared to those obtained from the flights of this aircraft. A flying wing, a conventional aircraft, a twin boom aircraft, and a biplane aircraft are among the four aircraft configurations compared using the proposed mathematical model (figure 3-10). The authors concluded that the reinforced-biplane configuration is the most efficient configuration as it is the best compromise between structural stiffness and energetic efficiency. This solution is stiffer than a flying wing, and its structural weight is approximately 80% that of a flying wing. Furthermore, as compared to a flying wing with the same wing surface, the wingspan is reduced by around 15%, and the tip deflection is roughly 40% of a flying wing with the same wingspan and wing surface. Another significant finding was, when a biplane and a monoplane with the identical lifting surfaces are compared, the bending stiffness of one wing of the biplane is substantially lower than that of the same monoplane, but the biplane's stiffness is higher comparing to the monoplane [39].

Flying wing Reinforced biplane

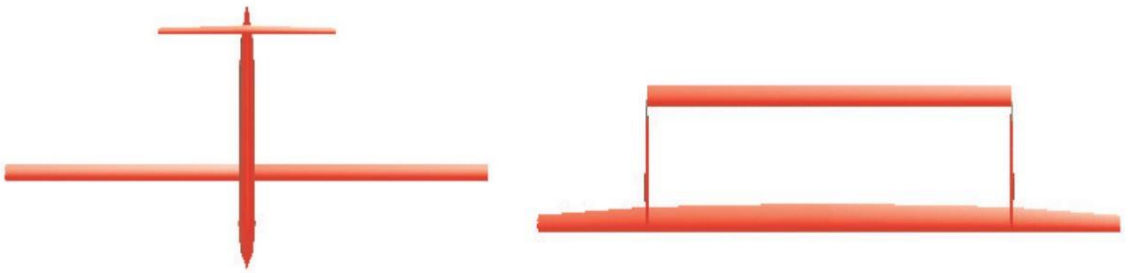

Conventional configuration Twin boom

Figure 3- 10: Four configuration proposed by Rizzo and Frediani [39]

Mattos, Secco, & Salles describe a multi-disciplinary design and optimisation framework to develop a high-altitude, solar-powered UAV. The aircraft baseline configuration that the framework is able to handle is very similar to that of Zephyr, which is developed by the UK based company QinetiQ. Aerodynamics, structures, stability, weight, and systems were all taken into account and incorporated into a modeFrontier® process, resulting in a very simple yet extremely realistic airplane sizing. The optimization target was chosen to lower the plane's required power and weight. As can be seen in Figure 3-11, the final configuration is pretty similar to the baseline aircraft [72].

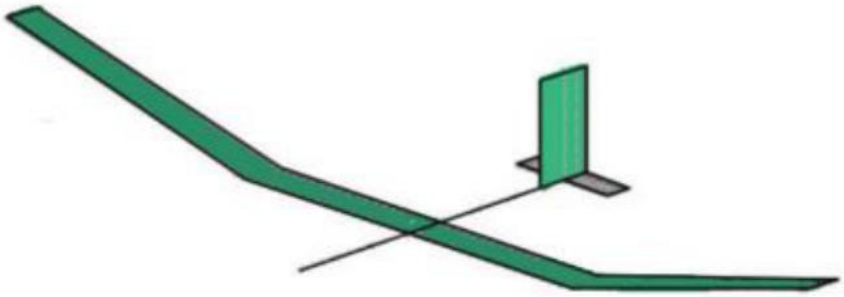

Figure 3- 11: Optimal airplane configuration from the mono- objective simulation[72]

Bryan Morrisey and Dr. Rob McDonald from California Polytechnic State University developed a multi-disciplinary tool to design a solar-powered, very-large aspect ratio, unswept, pinned-wing configuration of HALE UAVs. The application of wingtip coupling to a flying wing HALE aircraft is a game-changer in the field. Each part of the flying wing would theoretically lift its own weight and form a self-sufficient aircraft system. Stringing together a number of moderate aspect ratio wing segments to produce an extreme aspect ratio platform allows each segment to benefit from lower structural stresses while also reaping the benefits of a planform with an exceptionally high aspect ratio. When wing thickness to chord ratio, aspect ratio, wing loading, and power to weight ratio are incorporated as optimizer-controlled design factors, the integrated design environment demonstrates

the potential for a 17.3 % weight reduction. The approach did, in fact, allow for lower structural weight, minimal wing loading, and optimal aspect ratios in the upper 30s to low 40s, according to the researchers. Many of the same advantages can be achieved with advances in energy storage technologies, extremely efficient propulsion components, and a careful spanwise mass distribution applied to a one-piece flying wing. The increased complexity and risk involved with a pinned wing arrangement detract from the potential benefits [73]

Figure 3- 12:. Extreme aspect ratio concept [73]

4. Concept of HAPS

The development of design is an iterative process. It starts with a carefully selected set of criteria based on the best outcomes of any previous conceptual or experimental research. UAVs like Zephyr and Phasa-35 mission requirements were combined to create the HALE requirements. Although many different configurations are investigated and offer some benefits (like increased stiffness or exposure to sun rays), the conventional configuration where both wing and tail surfaces operate in a relatively clean aerodynamic environment still stands out as most reliable (we have the greatest amount of data, computation is more reliable than with double wings, etc.) and likely to succeed. That is why it is adopted in the current research.

4.1 Mission requirements

Maximum Take of Weight

Maximum take of weight of the UAV should be around 150 kg which is same like Phasa-35 by BAE system and Airbus's future HAPS aircraft Zephyr T.

Payload

The payload for this aircraft consists of the equipment necessary to supply communications networks, including 5G, as well as providing other services like surveillance, weather research and forecasting. The maximum weight of payload that will be allocated for this equipment is not to exceed 15 kg.

Endurance

The maximum endurance for this aircraft will be at least a couple of months at the cruising altitude

Cruise Speed

The maximum cruise speed for this aircraft is 25 m/s. This value was chosen based on a comparison of similar aircraft.

Cruise Altitude

The maximum cruise altitude will be 20000 meters.

4.2 Mission profile

The mission profile is shown in Figure 4-1. Details of each phase of the mission are as follows:

- Phase 1: The UAV will be launched by hand and will preferably climb continually with a fully charged batteries until it reaches a cruise altitude of 20000 meters.
- Phase 2: During the day, the UAV's solar cell will absorb the sun's energy and charge the battery and hover till dusk.
- Phase 3: When there is no more sunlight, the UAV will begin descending but will not descend below 15000 m altitude, and following sunrise, it will resume ascending to its operational altitude.
- Phase 4: Identical to Phase 2.
- Phase 5: It will descend to the land for maintenance after a few months of flying in the sky.

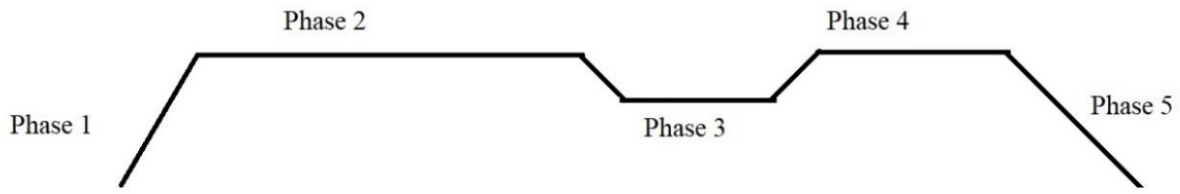

Figure 4- 1: Mission profile of solar powered UAV

4.3 Solar power collection, storage and uses

One of the main design requirements of the investigated HAPS is to remain airborne for several months over certain regions, e. g. Serbia or Bangladesh, where it could be used to improve global communication or observance capabilities. For that purpose, the HAPS propulsion system must incorporate (specially designed) propellers (section 9) connected to electric motors and a controller. Solar panels, which mostly cover the top surface of the wing but may also cover other portions of the UAV such as the tail or fuselage, are made up of solar cells connected in a certain configuration. During the day, they absorb and convert solar energy into electrical energy. The Maximum Power Point Tracker, or MPPT, is a converter that first supplies power to the propulsion group and onboard electronics then uses the excess energy to charge the lithium-ion battery. The battery supplies various energy-consuming parts during the night, and the battery must endure until the following day. Figure 4-2 depicts the energy flow of the solar aircraft. It should also be mentioned that the amount of collected power depends on many factors, such as the efficiency of solar cells, geographic location, time of year, weather conditions, etc.

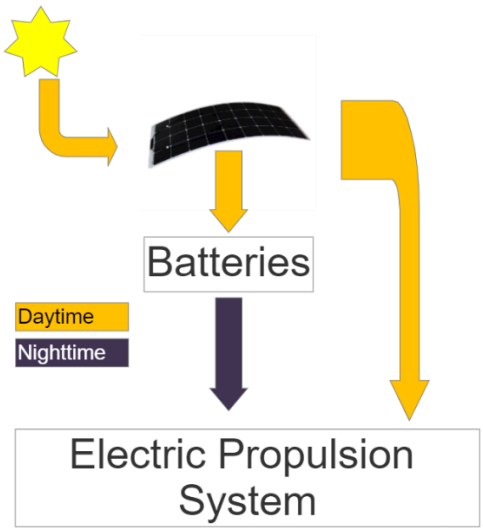

Figure 4- 2: Solar aircraft energy flow system

4.3.1 Solar cells and its working principle

A solar cell, also known as a photovoltaic cell, is a device that uses the photovoltaic effect to convert light energy into electrical energy directly. The vast majority of solar cells are made of silicon, which has improved in efficiency and cost as the materials have progressed from amorphous (noncrystalline) to polycrystalline (polycrystalline) and monocrystalline (single crystal) silicon forms. Monocrystalline uses completely pure semiconducting material, which provides a high-efficiency level but at a high cost. In contrast, polycrystalline is made up of crystal formations of various sizes

and silicon film is placed on glass or another substrate material to create amorphous solar cells. This layer has a thickness of less than 1 μm[74], [75].

From 1976 until the present, the National Renewable Energy Laboratory (NREL) keeps track of the highest proven conversion efficiencies of solar technologies (figure 4-3). The efficiency of the devices in this chart representing the current state of the art has been verified by independent, recognized test labs. Multijunction cells, single-junction gallium arsenide cells, crystalline silicon cells, thin-film technologies, and developing photovoltaics are among the semiconductor families whose efficiency figures are presented [76], [77]. Although research cell efficiencies were supposed to reach 50% by 2021, only a few companies have successfully produced solar cells with more than 25% efficiencies for commercial use. The Solar Impulse 2 plane was powered by solar cells manufactured by Sun Power, a Silicon Valley company, because they had the highest industry-leading efficiency (22.7%) [78].

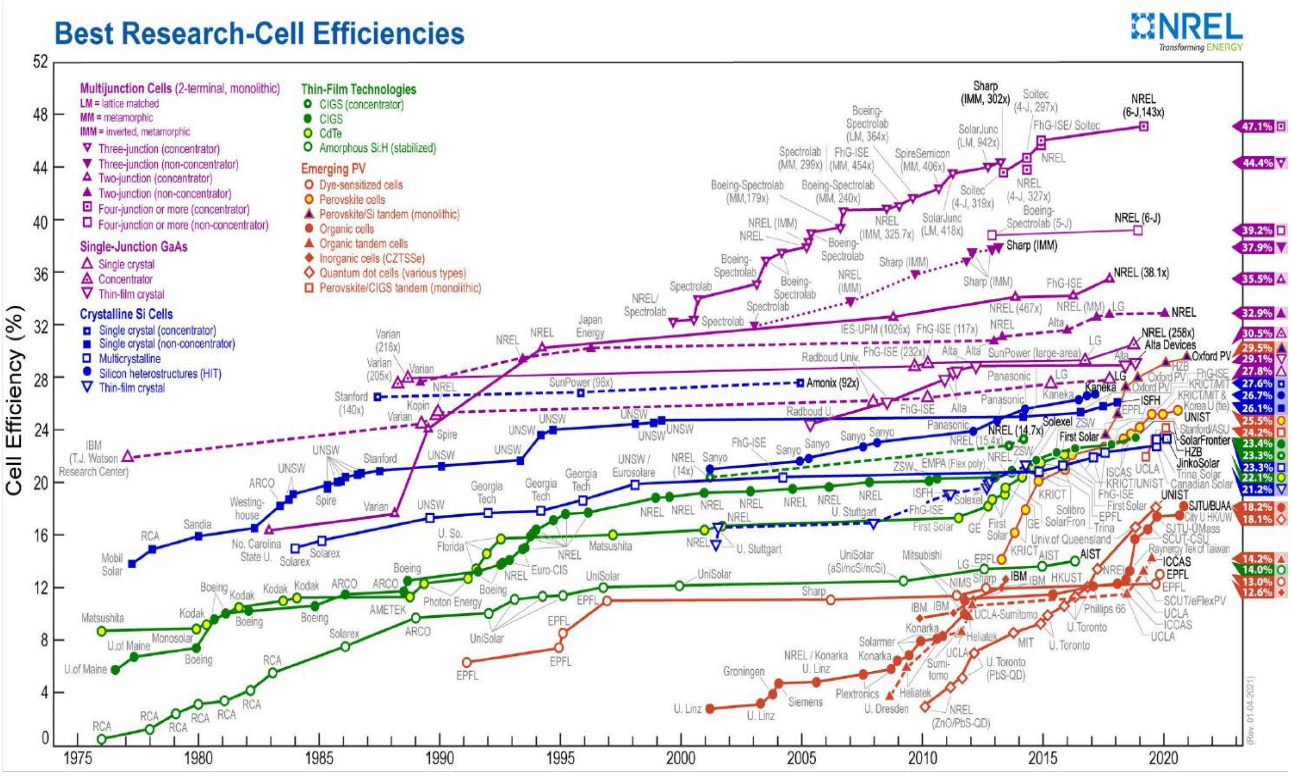

Figure 4- 3: Best research cell efficiencies [77]

Many manufacturers are working to enhance the efficiency of solar cells, and MicroLink is one of them. They've agreed to build high-efficiency solar cells with Airbus under a contract. MicroLink's epitaxially lifted off (ELO) solar cells have a maximum specific power of >2000 W/kg and a high efficiency of over 30%. MicroLink's ELO solar cells are suitable since they are less expensive to produce and produce more energy[79]. The Zephyr S UAV, which is powered by MicroLink's

lightweight and flexible high-efficiency solar sheet technology, has flown for over 25 days without refueling, setting a new long endurance flying record in 2018 [80].

Figure 4-4 shows the basic principle of a solar cell. Chemical components are used to create two layers: a p-conductive layer with a surplus of positive charge carriers and an n-conductive layer with an excess of negative charge carriers. An inner electrical field forms on the barrier layer as a result of this imbalance, resulting in charge separation at light incident. The charge carriers released during this process can be conducted through metal contact and utilised as direct current (DC) by an electrical device, or they can be sent into the network as alternating current (AC) by an interconnected inverter [81].

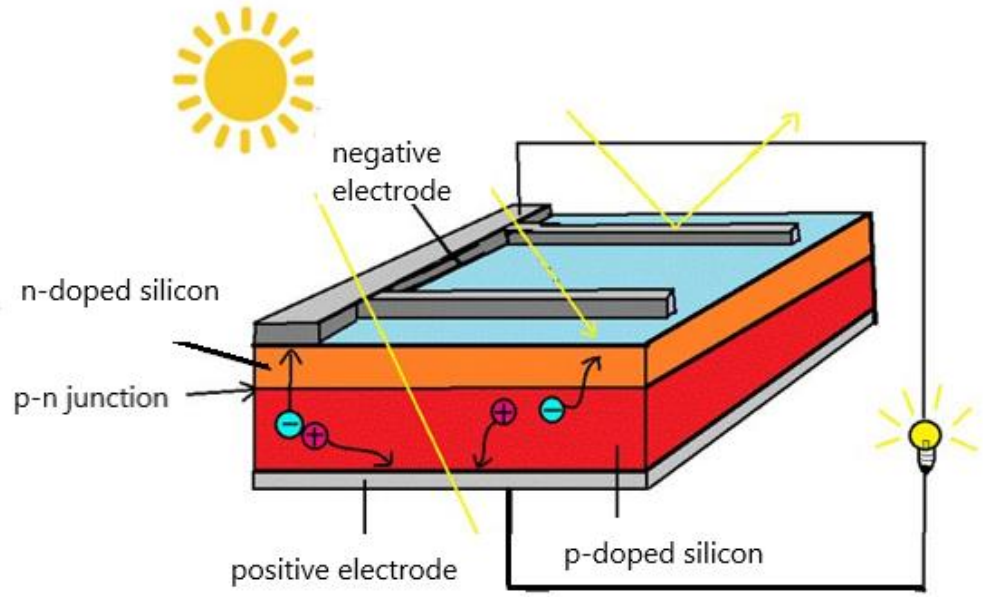

Figure 4- 4: Working principle of solar cell [82]

4.3.2 Rechargeable Batteries

In order to maintain continuous flying at high altitudes, solar-powered airplanes must have rechargeable batteries. The energy collected by the solar cells during the day is stored in the on-board batteries for consumption at night. However, the low energy density of batteries is one of the key drawbacks of solar-powered aircraft. As a result, high-energy-density storage devices are inevitable.

Several different combinations of chemicals are commonly used in rechargeable batteries. Lead-acid, Nickel-Cadmium (*NiCd*), Nickel-Metal-Hydride (*NiMH*), Lithium-ion (*Li-ion*) and lithium-ion polymer (*LiPo*) are some of them. Table 3 depicts the use of several types of batteries on various types of solar-powered aircraft, as well as their specific energy.

Lead-acid

Lead-acid batteries are the oldest type of batteries, invented by Gaston Plante in 1859. They are very cheap and mostly used in motor vehicles, but they are large in size and their performance decreases as temperature increases.

Nickel- Cadmium (NiCd)

This type of battery has both Nickel and Cadmium electrodes in Potassium Hydroxide solution. It has a higher energy density (40 to 60 Wh/kg) than Lead-acid. However, Nickel-Cadmium is relatively expensive and pose a charging problem during variance in temperature.

Nickel-Metal-Hybrid Battery (NiMh)

Nickel-Metal-Hybrid Battery is very similar to Nickel-Cadmium battery, but negative electrodes use a hydrogen-absorbing alloy instead of cadmium. As a result, it can have two to three times more capacity than NiCd while having the same size.

Lithium-Ion batteries

In Lithium-ion batteries, lithium-ions move from the negative electrode (made of carbon) to the positive electrode during discharge and back when charging. The electrolyte is a lithium salt in an organic solvent and the positive electrode is a metal oxide. They are one of the most popular types of rechargeable batteries and battery manufacturer Amprius is supplying lithium-ion cells to Airbus's Zephyr program. Amprius's developed the application of silicon for Li-ion anodes and enabled hundreds of cycles with specific energies of over 435 Wh/kg [83].

Lithium-Ion Polymer Batteries

The main difference from Lithium-ion batteries is that electrolyte is made of the solid polymer composite, not a conventional liquid solvent. As a result, LiPo has a number of advantages over lithium-ion batteries, including potentially cheaper manufacturing costs, scalability to a wide range of packaging forms, reliability, and robustness. However, their main disadvantage is that they have a lower charge capacity.

Table 3: Application of different batteries on solar-powered aircraft [84]

Name	Year	Battery	Specific Energy [Wh/kg]
Sunrise I [11]	1974	Li-ion polymer	145
Sunrise II[11]	1975	Li-ion polymer	145
Gossamer Penguin	1983	Nickel Cd	50
Solar Challenger	1981	Nickel Cd	50
Sky Sailor [13]	2004	Li-ion polymer	172.8
Solar Impulse I	2009	Li-ion polymer	240
Zephyr 7	2010	Lithium-sulphur	400-600
Solar Impulse II	2104/2016	Li-ion	260
Zephyr 8 [83]	2018	Lithium-ion	435

4.3.3 Estimation of daily power requirement and battery mass

The HAPS wing design process should begin with solar cell dimensioning and performance estimation, as this directly impacts the success of the entire aircraft. The HAPS mission is expected to be highly difficult. During the daytime, a 150 kg aircraft should be able to rise to its cruise height (i. e., within a time limit of 8 h). Afterwards, it should be able to repeat the daily cycles of descending and climbing between the elevations of 20 km and 15 km. (during the day- and night-time). Short daylight intervals and/or considerable decreases in direct normal solar irradiation (DNI) were not taken into account in this study. Belgrade, which is located at around 45 degrees north latitude, was instead considered during the summer months. In comparison, March is the month with the highest DNI in Dhaka (approximate northern latitude 24°), as indicated in Figure 4-5 [85]. All data on irradiance are freely accessible at [85].

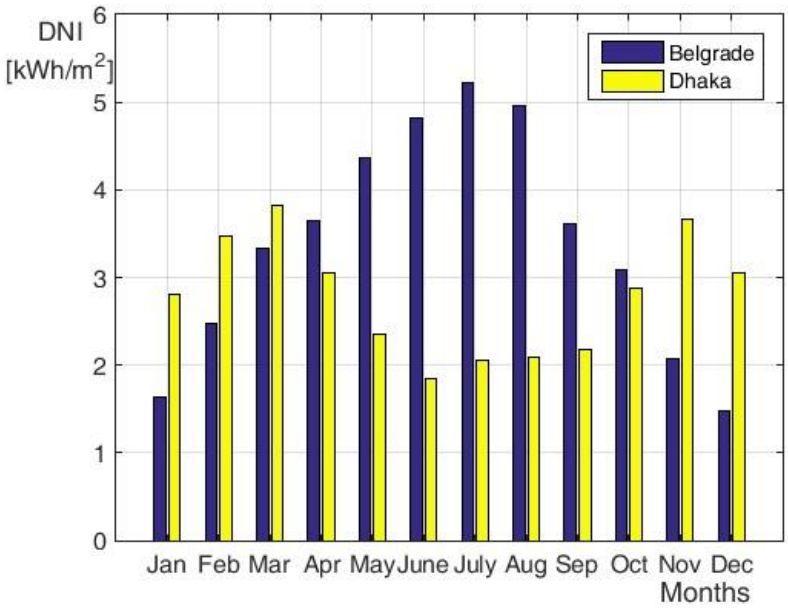

Figure 4- 5: Averaged yearly direct normal solar irradiation above Belgrade and Dhaka [86]

It is expected that solar module arrays cover 75% of the wing suction surface, or around 35 m^2. The root and leading edge are tiled first, followed by the trailing edge and wing tips. Because of its thin thickness, the wing's remaining surface area is either preserved for the control surfaces or ignored entirely. Additionally, it is expected that the aircraft will be able to position itself normal to the oncoming sun (through modest pitching, rolling, or yawing manoeuvres similar to those described in [40]) during the daylight will help it get the most solar power. The total mass of solar panels is projected to be 9 kg as the product of their reference area and solar cell density of 0.3 kg/m^2, with an approximated solar cell efficiency of 23-31 % (a lower value is for Belgrade, higher for Dhaka, as will be explained in continuation).

Figure 4-6 depicts simulations of a 24-hour flight in ideal working conditions for Belgrade and Dhaka, respectively (during a month with the shortest nighttime duration and greatest available DNI). Collected solar power is denoted by P_{solar}, power required for flight by P_{req}, while their difference ΔP is used to charge (or deplete) the batteries. The power system's first responsibility during the day is to maintain a steady flight at 20 km, power the electric motors, and deliver any excess power to the batteries. To save energy after the Sun sets, the aircraft may be allowed to glide to a (minimum) height of 15 km, where it must continue to cruise. During the daytime, batteries will be used to store energy for this part of the operation. As the Sun rises again, the solar panels continue to supply electricity and charge the batteries, the airplane returns to its upper cruising altitude of 20 km, and the cycle begins again. The amount of power needed to (cruise and) climb is determined by the formula:

$$T = D;\ \ L = W \tag{1}$$

$$P_{\text{req}} = TV_{cr}/\eta + LV_c, \tag{2}$$

where T is thrust force, D = drag force, lift force is L and aircraft weight is W, assumed climb speed is V_c = 0.83 m/s (which corresponds to the maximal glide ratio) and propeller efficiency η = 0.8.

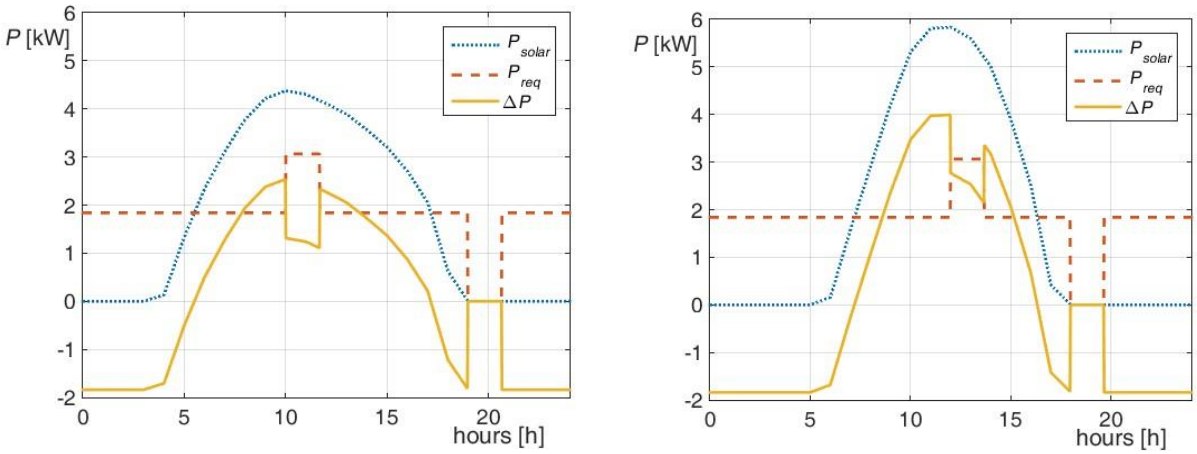

Figure 4- 6: Estimated daily power requirement[86]

A single-day flight above Belgrade in July will use about 43 kWh of energy, which can be found by integrating the power curves for each day, out of that, about 17 kWh must be stored in batteries for nighttime flight. With a battery specific energy density of 400 Wh/kg [87], the total needed mass of batteries is roughly 42 kg, accounting for 28 % of the overall HAPS mass.

Since available solar irradiation levels are significantly lower in Dhaka and the number of daytime hours is lower, the assumed wing design is capable of flight only if solar panels of higher efficiency are assumed. Therefore, with the value of 31%, presented HAPS shall be able to cruise above Bangladesh in March only if energy of 22 kWh per day can be accumulated, i. e. with the necessary battery mass of 55 kg corresponding to 37% of total aircraft mass [86].

4.4 Empty weight or UAV's airframe weight

The estimation of the vehicle's empty weight is one of the most crucial elements in the aircraft design process. While this task normally does not necessitate the use of complex mathematical tools, it can present significant challenges to the engineer. One of the difficulties is that underestimating or overestimating the empty weight of an airplane might have disastrous effects on the complete research project. Before embarking on serious development of a new aircraft, it is vital to evaluate the empty weight of aircraft being in the same class as the proposed design. The formulation that follows is referred to as historical relations because such a study concentrates on historical airplanes. It is crucial to know the aircraft's gross weight before calculating the empty weight using historical data. We will utilize the sailplane formula because we are dealing with high-altitude aircraft, which are commonly referred to as sailplanes because they both have high aspect ratio wings [37].

$$\frac{W_e}{W_0} = 0.3255 + 0.0386 \cdot \ln W_0 \tag{3}$$

Equation 3 is the formula to obtain empty weight if the gross weight is already known. W_e denotes the aircraft's empty weight, while W_0 denotes its gross weight.

Defining a good structural weight or empty weight model for solar-powered aircraft is quite difficult. Even the two widely used methods in the literature for solar airplanes seemed inadequate at a scale of a couple of meters.

The first method was described by D.W. Hall in a NASA contractor report [38], where he described a structural weight estimation model in which the mass of all the elements that make up the airframe, such as the spar, leading and trailing edges, covering, ribs, control surfaces, fuselage, and tail, was calculated as a function of total mass, aspect ratio, and wing area. Though the method is very detailed, its applicable to airplanes whose weights are between 453 and 1360 kilograms. W. Stender proposed the second method in 1969, which is based on statistical data for sailplanes with twin boom tails. Where W_{af} is aircraft's airframe weight, *S* surface area and *AR* aspect ratio;

$$W_{af} = 8.763\, n^{0.311}\, S^{0.778} AR^{0.467} \tag{4}$$

This model was adopted by Rizzo [39], who also suggested his own mathematical model for UAVs. His paper adopted two kinds of predictions to define a good structural weight. The first one was based on statistical data for sailplanes with twin booms, whilst the second one was obtained by interpolating the data published for the NASA prototypes (Pathfinder, Centurion, Helios). Rizzo's first weight

model was preferred for manned vehicles, so we are not going to discuss that, but the second model which is preferred for UAV's is:

$$W_{af} = 1.548\, S^{0.656} AR^{0.6514} \quad (5)$$

These models could give reasonable weight estimations for conventional or twin-boom aircraft but not in the case of a biplane or multi- plane configurations. Rizzo's model was validated by comparing with the data of Helios aircraft, which was designed to fly at 24km of altitude with a payload of 330 kg. So, this model will give better results for UAVs with a payload of more than 100 kg. Ahmad Alsahlani also used this model for his Swept-Wing High-Altitude Long-Endurance UAV [88], which can carry a 100 kg payload.

To verify these models, A. Noth [13] created a database of 415 sailplanes of various sizes. The Stender and Rizzo models were shown on a graph with two alternative aspect ratios of 15 and 30. As a result, Rizzo's equation approaches the best sailplane models, which is understandable given that it was generated from data from unmanned solar airplanes. However, it is unsuitable for small models due to its pessimistic nature. Stender's equation is significantly over-optimistic for manned airplanes, while it is far too pessimistic for small-scale models.

A. Noth also proposed a new empirical model based on the realized 415 sailplanes database. First, he divided the aircrafts into two groups: those that are lighter and those that are heavier than the mean weight model, in order to achieve a model of just the greatest quality sailplanes. He then presented a conditional mathematical model that produced 260 airframes that were lighter than the mean model, indicating that their weight construction quality was superior to the half. After several iterations, he came up with 19 of the greatest sailplanes, accounting for 5% of the 415 initial airframes. He then referred to them as the top 5% aircraft weight prediction model.

$$W_{af} = 0.44\, S^{1.55} AR^{1.30} \quad (6)$$

Although this model proved effective for his 2.5 kg UAV, several large solar aircraft differed significantly from his developed model. The Helios, for example, has an aspect ratio of 30.85, which weighs 20 times less than the best 5% model would predict. Table 4 shows how significantly equations 3, 4, and 5 differ from one another. However, as previously said, Rizzo's model is suited for payloads greater than 100 kg, and NASA's UAVs empty weight is very near to the airframe weight derived by Rizzo's model, while Stender's model is suitable for payloads less than 100 kg, and Noth's model is applicable for UAV's which weight less than 10 kg.

Table 4. Airframe weight of different Solar powered HALE aircraft using Noth, Stender and Rizzo's equation.

UAV's	Span b [m]	Aspect ratio, *AR*	Surface area, s [m^2]	Empty weight [kg]	Noth *Waf* [kg]	Stender *Waf* [kg]	Rizzo *Waf* [kg]	Empty wt. (eq 3). [kg]
Pathfinder	30	12.3	73.17	207	908.62	81.36	132.56	135.81
Pathfinder Plus	36.3	15.1	87.26	247.5	1558.65	102.69	170.06	172.48
Helios	75.3	30.4	186.52	600	12564.05	257.10	441.40	548.08
Centurion	61.8	25.8	148.03	533	7094.85	198.95	340.88	504.86
Zephyr -S	25	22.3	28.02	30	444.96	50.91	104.05	31.10
Phasa -35	35	17.5	70.00	60	1341.64	92.68	161.99	77.84
BS Solar HALE	33	22	49.50	60	1055.77	78.76	149.78	77.84

Because the empty weights of the Zephyr -S and Phasa-35 are close to those of Stender's model and equation 3 (sailplane empty weight formula), we can simply use this model to determine the empty weight of our HAPS. However, according to many researchers, the empty weight of HAPS aircraft will be around 60 kg, which is 40-45 % of the MTOW. One of the key reasons for using Phasa-35 and Zephyr as role models for our research is that it is the first of its kind. To the author's knowledge, no investigation of these types of HALE or HAPS has been conducted. Currently, only Airbus and BAE systems are involved in this project. We decided to take on the challenge because HAPS is substantially less expensive than a standard platform station, and we wanted to learn how to design such UAVs.

4.5 Wing loading estimation

The wing loading of a solar-powered aircraft is one of the first tasks that must be completed while developing a solar-powered aircraft. The stalling speed, the rate of climb, the runway distance, the drag coefficient, and other essential properties are all affected by this parameter. Stalling speed is the minimum speed at which the lift coefficient is maximum. The maximum lift coefficient and wing loading are shown in Equation 7, which was derived from the steady-level flight equation [89].

$$W = L \tag{7}$$

$$W = mg = C_L \frac{\rho}{2} S v^2 \tag{8}$$

$$C_L \cdot q = \frac{W}{S} \tag{9}$$

where C_{Lmax} is the maximum lift coefficient, q is the dynamic pressure and $\frac{W}{S}$ is the wing loading. Aircraft mass 150 [kg], density of the air at 20 [km] altitude (ρ) and velocity (v= 25 [m/s]) are already known. As a result, the level flight equation simply has two unknowns: surface area and design lift coefficient (eq. 9).

If the surface area of the wings is known, the wing loading may be estimated. Likewise, the surface area can be calculated if the lift coefficient (C_L) is known. One of the most important factors of solar aircraft is having a high lift coefficient as it will give higher glide ratios and long endurance. During the literature review, it is observed that solar-powered airplanes have a very high lift coefficient, ranging from 0.8 to 1.4. Here, the wing surface area is calculated by varying C_L from 0.8 to 1.2 and eventually wing loading from the surface area. Table 5 shows the surface area and wing loading for different lift coefficients.

Table 5. Estimation of wing loading by varying lift coefficient in eq. 9.

By varying C_L cruise		
C_L	**S [m^2]**	**W/S [N/m^2]**
0.8	66.86	22.01
0.85	62.93	23.38
0.9	59.43	24.76
0.95	56.30	26.14
1	53.49	27.51
1.05	50.94	28.89
1.1	48.63	30.26
1.15	46.51	31.64

1.2	44.57	33.01

Another way to find wing loading is by using Rizzo's equation (eq. 10) for solar powered aircraft. Where Rizzo uses the following equation to predict the wing loading of the aircraft

$$W/S = 63.24W^{-0.524}AR^{0.992} \quad (10)$$

As we already defined the weight of the aircraft (150 kg) from the historical data in the previous section, we will use equation 10 to find the wing loading *(W/S)* for various aspect ratios. Table 6 shows wing loading *(W/S)* and surface area *(S)* of the wing for different aspect ratios.

Table 6. Estimation of wing loading by using Rizzo's equation

Rizzo Model			
AR	***W/S* [N/m^2]**	***S* [m^2]**	***b* [m]**
16	21.66	67.95	32.97
17	23.00	63.98	32.98
18	24.34	60.46	32.99
19	25.68	57.30	33.00
20	27.02	54.46	33.00
21	28.36	51.88	33.01
22	29.70	49.54	33.01
23	31.04	47.41	33.02
24	32.38	45.45	33.03
25	33.72	43.64	33.03

NASA's technical paper about design consideration of Solar-powered aircraft stated that the wing loading should greater than 15 [N/m^2] and the regions of feasible operations occur in the range of 15 to 30 [N/m^2] [90]. Before deciding on the final aspect ratio and wing loading, the author opted to examine wing geometry for different airfoils by altering the aspect ratio and taper ratio of the wing [89].

5 Airfoil selection

During all phases of flight, the airfoil influences cruise speed, takeoff and landing distances, stall speed, handling qualities (particularly near stall), and overall aerodynamic efficiency. It is essential to design high-lift airfoils for solar-powered high–altitude aircraft, as it can result in increased endurance, payloads, shorter takeoff and landing distances, and lower stall speeds.

First of all, it is crucial to have a good knowledge of airfoil geometry. The key geometric parameters of an airfoil are depicted in Figure 5-1. An airfoil's appropriate horizontal reference axis begins at the "leading edge" and ends at the "trailing edge." One of the important parameters of an airfoil is its chord length. It is the distance along a straight line from the leading edge to the trailing edge. The front of the airfoil is defined by a leading-edge radius, tangent to the upper and lower surfaces. The leading-edge radius (LE) has a significant impact on aerodynamics, such as lift, drag, and stall characteristics. The leading-edge radius in Figure 5-1 is significantly exaggerated. Real ones are substantially smaller and only come into contact with the airfoil at the very front. They mathematically define the curvature precisely at the point of minimal radius (usually the LE). Another very important parameter of the airfoil is angle of attack (AOA).

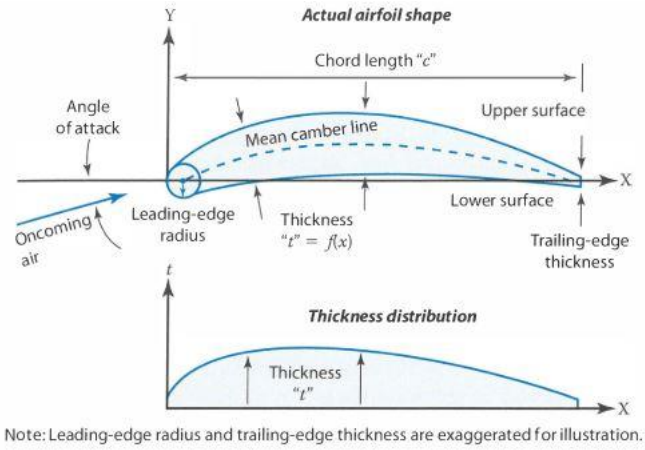

Figure 5- 1: Airfoil geometry [2]

The air flow of initial freestream velocity v along the airfoil contour provides a distinct pressure distribution on the upper and lower sides of the airfoil, which can be represented as two forces, lift and drag. The following formulae can be used to compute these forces:

$$F_L = C_L \cdot \frac{\rho}{2} v^2 \cdot S \tag{11}$$

$$F_D = C_D \cdot \frac{\rho}{2} v^2 \cdot S \tag{12}$$

C_L and C_D are the lift and drag coefficients, respectively, where ρ is the air density, S the wing area, and v the relative airspeed. The C_L and C_D are strongly influenced by the airfoil, the angle of attack, surface quality (smooth/rough) and the Reynolds number *Re*. Figure 5-2 illustrates the lift dependence on the angle of attack. Increasing it raises the C_L, but it also initiates the flow separation from the trailing edge, which assists in the creation of a turbulent zone, therefore raises the C_D. At the stall, the lift is maximum, but the drag is high too. After this point, the behaviour becomes more difficult to predict or simulate, yet the drag continues to rise accompanied by a decline in lift. Thus, for an airplane, the intriguing and safe zone is just before the stall point, and for gliders, it's at the point where the glide ratio C_L/C_D is at its highest.

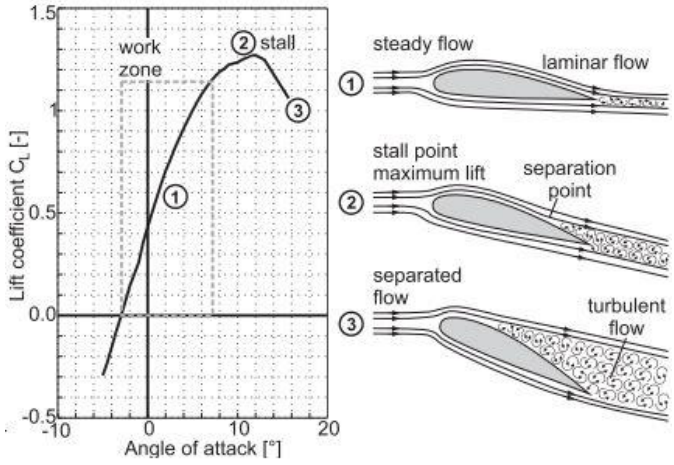

Figure 5- 2: Lift coefficient depending on the angle of attack [13]

The priority of the parameters that we take into account when choosing an airfoil can vary from one category of aircraft to another, so it is difficult to prescribe a universal methodology.

The flight profiles of HALE UAVs at low air density and moderate flight speeds correspond to low Reynolds number operating conditions. Each airfoil is designed with a specific Reynolds number in mind. When an airfoil is used at a substantially lower or higher Reynolds number (half an order of magnitude or so), the section properties can be very different from what is expected. Reynolds number *Re*, which represents the ratio of inertial to viscous forces, can be written in the following formulae

$$R_e = \frac{\rho v c}{\mu} \tag{13}$$

Here, μ is the dynamic viscosity that once divided by the air density gives the kinematic viscosity and *c* represents the chord length. Table 7 depicts the Reynolds numbers which are determined by using different aspect ratios and taper ratios.

Table 7. Reynolds numbers for different taper ratios and aspect ratios

AR	Span, b	Taper ratio	Root Chord, Cr	Tip Chord, Ct	MAC	Re
18	32.99	**0.6**	2.29	1.37	1.87	2.87E+05
19	33.00	**0.6**	2.17	1.30	1.77	2.72E+05
20	33.00	**0.6**	2.06	1.24	1.68	2.59E+05
21	33.01	**0.6**	1.96	1.18	1.60	2.47E+05
22	33.01	**0.6**	1.88	1.13	1.53	2.35E+05
23	33.02	**0.6**	1.79	1.08	1.47	2.25E+05
24	33.03	**0.6**	1.72	1.03	1.40	2.16E+05
25	33.03	**0.6**	1.65	0.99	1.35	2.07E+05
26	33.04	**0.6**	1.59	0.95	1.30	1.99E+05
27	33.04	**0.6**	1.53	0.92	1.25	1.92E+05
28	33.05	**0.6**	1.48	0.89	1.20	1.85E+05

AR	Span, b	Taper ratio	Root Chord, Cr	Tip Chord, Ct	MAC	Re
18	32.99	**0.8**	2.04	1.63	1.84	2.83E+05
19	33.00	**0.8**	1.93	1.54	1.74	2.68E+05
20	33.00	**0.8**	1.83	1.47	1.66	2.55E+05
21	33.01	**0.8**	1.75	1.40	1.58	2.43E+05
22	33.01	**0.8**	1.67	1.33	1.51	2.32E+05
23	33.02	**0.8**	1.60	1.28	1.44	2.22E+05
24	33.03	**0.8**	1.53	1.22	1.38	2.12E+05
25	33.03	**0.8**	1.47	1.17	1.33	2.04E+05
26	33.04	**0.8**	1.41	1.13	1.28	1.96E+05
27	33.04	**0.8**	1.36	1.09	1.23	1.89E+05
28	33.05	**0.8**	1.31	1.05	1.19	1.82E+05

AR	Span, b	Taper ratio	Root Chord, Cr	Tip Chord, Ct	MAC	Re
18	32.99	**1**	1.83	1.83	1.83	2.82E+05
19	33.00	**1**	1.74	1.74	1.74	2.67E+05
20	33.00	**1**	1.65	1.65	1.65	2.54E+05
21	33.01	**1**	1.57	1.57	1.57	2.42E+05
22	33.01	**1**	1.50	1.50	1.50	2.31E+05
23	33.02	**1**	1.44	1.44	1.44	2.21E+05
24	33.03	**1**	1.38	1.38	1.38	2.11E+05
25	33.03	**1**	1.32	1.32	1.32	2.03E+05
26	33.04	**1**	1.27	1.27	1.27	1.95E+05
27	33.04	**1**	1.22	1.22	1.22	1.88E+05
28	33.05	**1**	1.18	1.18	1.18	1.81E+05

Compared to more conventional lower-altitude aircraft, the required lift coefficient for solar aircraft is high. As a result, the airfoil section must be optimized to operate at high lift coefficients while generating the least amount of drag. These are airfoils at the root and at the end of the wing, which with their aerodynamic parameters, directly affect other evolutionary profiles along the wingspan and global characteristics of the wing. In practice, airfoils from the same family are most often chosen, so the parameter of local evolutionary airfoils can be estimated with satisfactory accuracy by linear interpolation of the values of basic airfoils. Gliders are the most inspiring models for long-distance flight. When performance calculations are carried out, it becomes evident that anyone constructing a HALE UAV should examine the glider's airfoils before selecting the most suitable airfoil.

Following factors are crucial in selection of airfoils for HALE UAVs.

- An airfoil's key distinguishing feature is that it must be designed for a low Reynolds number. Because the solar-powered aircraft will be flying at low speeds, the mission will generate a low Reynolds number; hence an airfoil with ideal properties at low speeds should be chosen. M. Selig [91] proved that low Reynolds number airfoils can be designed through the design philosophy to

achieve lift coefficients much higher than previously possible. By applying his philosophy, he successfully designs an airfoil that achieved a $C_{lmax} = 2.2$ at $Re = 2 \times 10^5$.

- The airfoil with the highest maximum lift coefficient (C_{lmax}).

- The glide ratio corresponds to the maximum distance that can be flown from a given height in non-motorized flight (glider), which is e.g. of primary importance in the design of gliders or long-endurance aircraft. Therefore, the choice of airfoil with the highest possible value of maximum glide ratio C_l/C_d will contribute to the overall increase of the maximum glide ratio of the wing and the entire aircraft.

- The maximum climbing factor or C_l^3/C_d^2 is also an element to consider. Flight at the lift coefficient that corresponds to the maximum of this parameter gives the longest length of non-motorized flight, in addition to the most efficient ascending (for sailboats).

- The airfoil with the lowest minimum drag coefficient (C_{dmin}).

While it is important to have a good understanding of the factors that influence airfoil selection, an aircraft designer should not spend too much time in the early stages of conceptual design trying to pick the perfect airfoil. Later trade studies and analytical design tools will determine the desired airfoil characteristics and geometry.

5.1 Airfoil selection through XFLR 5

The XLFR 5 is an analysis tool for airfoils, wings and planes operating at low Reynolds numbers which includes XFoil's direct and inverse analysis capabilities, wing design and analysis capabilities based on the Lifting Line Theory, on the Vortex Lattice Method, and on a 3D Panel Method to predict lift and drag values of the airfoils and wings. Three low Reynold's number airfoils (Eppler 387, S1210, and s1223) (Figure 5-3) were examined for five different Reynolds numbers ranging from 150000 to 300000 with an increment of 50000 by using XFLR5 [92]. Using XFLR5 software, a graph of *l/d* vs angle of attack was created, shown in Figure 5-4. As the figures show, these airfoils have a high lift-to-drag ratio and they also have a wide range of operating angle of attack where the lift-to-drag ratio is optimum [89].

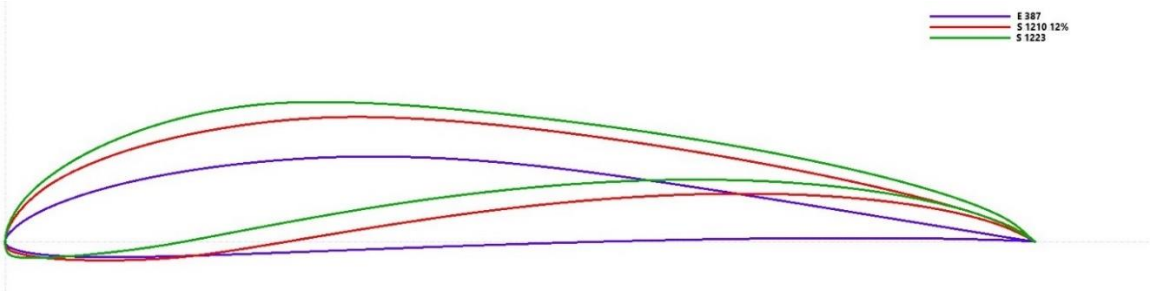

Figure 5- 3: Airfoils E387, S1210 and S1223 [89]

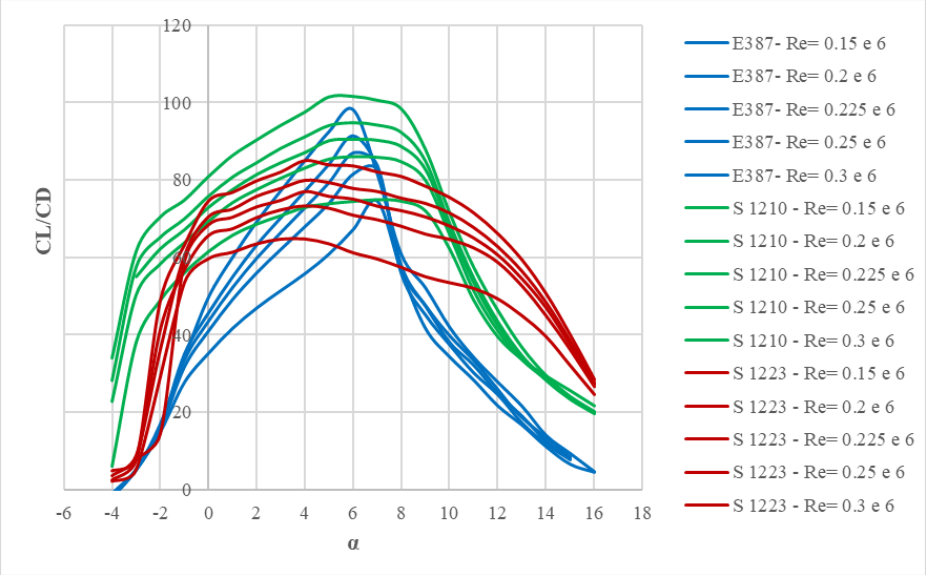

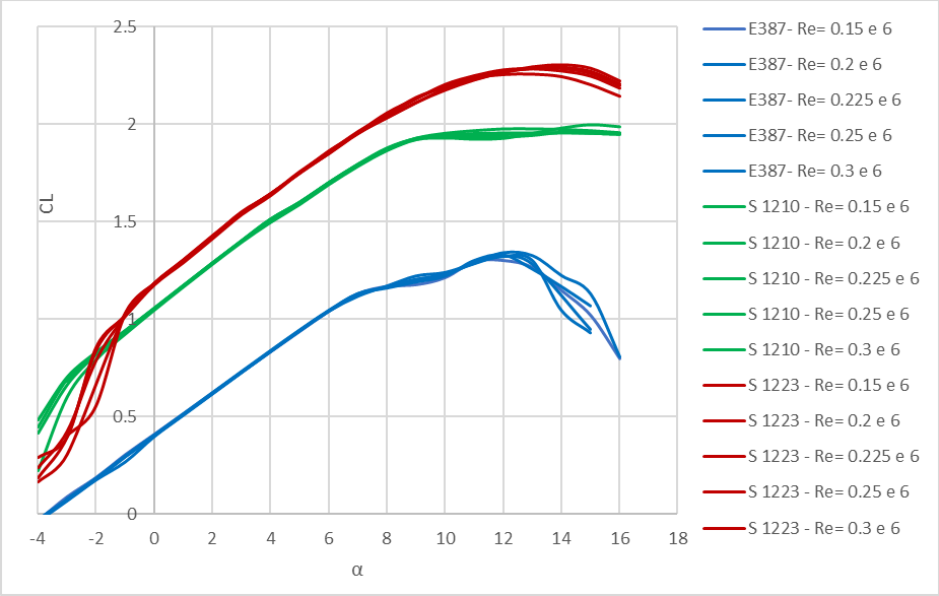

Figure 5- 4: C_l/C_d versus alpha and C_l versus alpha [89]

Table 8 shows all the important parameters of the investigated airfoils. The design lift coefficient of the HALE drones varies from 0.8 to 1.75 but we should also keep in mind that drag coefficients get higher with high lift coefficients as separation bubble occur at the trailing edge. So, we decided to select a value of 1 for cruise lift coefficient (C_l=1). As design Reynolds numbers lies in between 200000 and 250000 at cruise altitude (20 km), airfoil properties for those Reynolds numbers are given in table 8.

Table 8. Airfoils properties at cruise altitude

Re=200000								
Airfoil	Max thickness	C_{lmax}	$(C_l/C_d)_{max}$	Stall angle (α)	C_{di} @ C_{lmax}	α @ $(C_l/C_d)_{max}$	C_d @ C_l=1	α @ C_l=1
e387	9.10%	1.33	82.7	12	0.055	7	0.0127	5.579
s1210	12%	1.96	86	15	0.068	6	0.0148	-0.4
s1223	12.10%	2.28	73	12	0.04	4	0.018	-1.14
Re=250000								
Airfoil	Max thickness	C_{lmax}	$(C_l/C_d)_{max}$	Stall angle (α)	C_{di} @ C_{lmax}	α @ $(C_l/C_d)_{max}$	Cd @ C_l=1	α @ C_l=1
e387	9.10%	1.32	91	12	0.052	6	0.011	5.577
s1210	12%	1.958	95	14	0.068	6	0.0134	-0.41
s1223	12.10%	2.29	80	14	0.04	4	0.017	-1.08

5.1.1 Selection of airfoil by studying the wing characteristics

A detailed analysis of wings with various aspect ratios, taper ratios, and airfoils was performed before selecting a specific airfoil. At the design phase of the wing, governing variables such as wing area, taper ratio, and aspect ratio are used to establish the basic dimensions of the wing (span and chords at root and tip). The required wingspan (b), root chord (C_r), tip chord (C_t), and mean aerodynamic chord of a simple tapered planform wing were calculated using the following formulas (eq. 14-18). Airfoil e387 was used for the first eight wings, s1210 for wings 9–16, and s1223 for the final eight wings (17–24). Each wing aspect ratio (AR = 22, 24 and 26) had a taper ratio of 0.6, 0.8 and 1. The total wing span ranges from 33.01 to 33.04 meters. Table 9 shows the properties of all 24 wings that were examined for 3D analysis in XFLR5 at operating altitudes. The vortex lattice approach was used by program XFLR5 to predict the wing's lift and drag values [89].

$$\text{Aspect ratio, } AR = \frac{b^2}{S} \Rightarrow b = \sqrt{AR.S} \tag{14}$$

$$\text{Taper ratio, } \lambda = \textit{tip chord/ root chord;} \ [\lambda = 1, \text{ for rectangular wing}] \tag{15}$$

$$\text{Root chord, } C_r = \frac{2b}{(1+\lambda)AR} \tag{16}$$

$$\text{Tip chord, } C_t = \lambda C_r \tag{17}$$

$$\text{Mean aerodynamic chord, } MAC = (2/3)C_r \left(\frac{1+\lambda+\lambda^2}{1+\lambda}\right) \tag{18}$$

Table 9. Basic dimensions of the wings and their properties at operating altitude [89]

Wing	***AR***	**Taper ratio**	**Wingspan [m]**	**Root Chord [m]**	**Tip Chord [m]**	**MAC [m]**	**Airfoil**
Wing 1	22	0.6	33.01	1.88	1.13	1.53	e387
Wing 2	22	0.8	33.01	1.67	1.33	1.51	e387
Wing 3	22	1	33.01	1.50	1.50	1.50	e387
Wing 4	24	0.6	33.03	1.72	1.03	1.40	e387
Wing 5	24	0.8	33.03	1.53	1.22	1.38	e387
Wing 6	24	1	33.03	1.38	1.38	1.37	e387
Wing 7	26	0.8	33.04	1.41	1.13	1.28	e387
Wing 8	26	1	33.04	1.27	1.27	1.27	e387

Wing 9	22	0.6	33.01	1.88	1.13	1.53	s1210
Wing 10	22	0.8	33.01	1.67	1.33	1.51	s1210
Wing 11	22	1	33.01	1.50	1.50	1.50	s1210
Wing 12	24	0.6	33.03	1.72	1.03	1.40	s1210
Wing 13	24	0.8	33.03	1.53	1.22	1.38	s1210
Wing 14	24	1	33.03	1.38	1.38	1.37	s1210
Wing 15	26	0.8	33.04	1.41	1.13	1.28	s1210
Wing 16	26	1	33.04	1.27	1.27	1.27	s1210
Wing 17	22	0.6	33.01	1.88	1.13	1.53	s1223
Wing 18	22	0.8	33.01	1.67	1.33	1.51	s1223
Wing 19	22	1	33.01	1.50	1.50	1.50	s1223
Wing 20	24	0.6	33.03	1.72	1.03	1.40	s1223
Wing 21	24	0.8	33.03	1.53	1.22	1.38	s1223
Wing 22	24	1	33.03	1.38	1.38	1.37	s1223
Wing 23	26	0.8	33.04	1.41	1.13	1.28	s1223
Wing 24	26	1	33.04	1.27	1.27	1.27	s1223

The 3D characteristics of wings at operating altitudes are shown in Table 10. Again, all the wings in XFLR5 were analysed using the vortex lattice method to predict lift and drag values.

Table 10**.** 3D properties of wings at operating altitude [89]

	Wing 1	**Wing 2**	**Wing 3**	**Wing 4**	**Wing 5**	**Wing 6**	**Wing 7**	**Wing 8**
C_{Lmax}	1.2	1.19	1.18	1.21	1.2	1.19	1.22	1.2
$\alpha@C_L=1$	6.8	6.99	7	6.78	6.82	6.93	6.75	6.8
C_d $@C_L=1$	0.0266	0.0275	0.0279	0.0261	0.0265	0.0272	0.0262	0.0268
L/D @ $\alpha=C_{Lmax}$	37.6	36.3	35.8	38.8	37.6	36.7	38.2	37.37
$(L/D)_{max}$	38.9	37.9	37.6	39	38.4	37.78	38.35	37.63

	Wing 9	**Wing 10**	**Wing 11**	**Wing 12**	**Wing 13**	**Wing 14**	**Wing 15**	**Wing 16**
C_{Lmax}	1.9	1.88	1.86	1.91	1.89	1.88	1.91	1.89
$\alpha@C_L=1$	-0.4	-0.3	-0.25	-0.48	-0.4	-0.32	-0.45	-0.4
$C_d\ @C_L=1$	0.0295	0.0303	0.0312	0.0288	0.0296	0.0303	0.0291	0.0298
$L/D\ @\ \alpha= C_{lmax}$	34	33.1	32.1	34.6	33.7	33	34.4	33.6
$(L/D)_{max}$	34.5	33.6	32.7	34.9	34	33.3	34.3	33.7
	Wing 17	**Wing 18**	**Wing 19**	**Wing 20**	**Wing 21**	**Wing 22**	**Wing 23**	**Wing 24**
C_{lmax}	2.205	2.19	2.17	2.23	2.21	2.19	2.23	2.221
$\alpha@C_L=1$	-2.7	-2.6	-2.5	-2.8	-2.7	-2.65	-2.7	-2.7
$C_d\ @C_L=1$	0.035	0.036	0.0361	0.0348	0.0356	0.0365	0.0355	0.0363
$L/D\ @\ \alpha= C_{Lmax}$	28.2	27.7	27.3	28.8	27.6	27.3	28.5	27.8
$(L/D)_{max}$	30	29.2	28.4	31	30.1	29.1	30.8	29.7

A wing with the largest glide ratio $(L/D)_{max}$ has been chosen after conducting both airfoil and wing evaluations in XFLR5. It has already been proven that a wing with a taper ratio equivalent to that of an elliptical wing (taper ratio = 0.57) provides the optimum glide ratio as well as the lowest induced drag ratio. They, on the other hand, have poor stall qualities and are more difficult to manufacture. As a result, for the conceptual design phase of Wing 11, a rectangular wing with an aspect ratio of 22 and an airfoil s1210 was chosen. The Selig 1210 airfoil was chosen because it possesses all of the features needed in solar-powered, high-altitude, long-duration aircraft. The first is that it is an airfoil for a low Reynolds number. Because this UAV will be flying at low speeds, a low Reynolds number will be present throughout the mission, hence an airfoil with excellent low-speed characteristics was chosen. Despite the fact that the wing with the e387 airfoil has a higher glide ratio than the s1210, its design angle of attack (AoA) corresponding to the design lift coefficient is dangerously close to its critical AoA. Airfoil s1223, on the other hand, has a very high lift coefficient but a low glide ratio (Figure 5-4). Because a high aspect ratio wing creates less tip vortex than a low-aspect-ratio wing, and the strength of the tip vortex is lessened, a wing with an aspect ratio of 22 is chosen for further investigation. As a result, when compared to a low-aspect-ratio wing of equal area, the high-aspect-ratio wing loses less lift and induces less drag owing to tip effects[2].

Specification of **wing 11:**

Aspect ratio 22; Taper ratio 1; Wingspan 33 [m]; mean aerodynamic chord 1.5 [m].

Design lift coefficient C_L = 1.08; at operating altitude (20 km) for cruising speed (25 m/s) and surface area (S = 49.50 m^2) was derived from the horizontal flight equation [89].

5.2 Airfoil selection through airfoil optimization

Optimization is one of the most important stages in the aircraft design process since it increases the efficiency of the process without increasing the cost. In [93], the authors give an overview of the civil HALE UAV design effort, saying that enhancing aerodynamic efficiency and optimizing aircraft structures could lower operational costs. A substantial amount of study has been undertaken in the topic of airfoil shape optimization in recent years, as this technique helps to increase airfoil performance as well as overall aircraft performance, which is more than helpful given that power consumption can be significant. Because endurance (flight duration) and range (path length) are critical performance aspects of HAPS UAVs, optimizing them can result in longer endurance and range as well as lower power consumption. Many studies have been conducted to optimize the geometric parameters of airfoils in order to get a higher glide ratio and hence greater endurance, although this involves additional effort. Many examples of their parameterization and optimization can be found in the literature [42]–[45], [94]–[98]. Reference [42] used multi-objective optimization technologies in conjunction with computational fluid dynamics (CFD) to improve the design of a high aspect ratio airfoil for a long-range UAV. The authors of [94] examined 400 cases and concluded that ProfoilGA and BezierGA are both trustworthy in generating an airfoil with a 14% reduction in drag. Reference [95] utilised a differential evolution algorithm to optimize a constrained (area-preserving) airfoil, with XFOIL [99] estimating the aerodynamic performances of each considered airfoil. In contrast, starting with the NACA 2411 airfoil, [43] formulates and solves an aerodynamic shape optimization process, and the optimized airfoil is validated through an experimental process, with the results of the genetic algorithm (GA) for the optimized airfoil being found to be reasonably close to the results obtained from wind tunnel measurements. Using a *transition SST* turbulence model [100], the authors of [44] used an evolutionary optimization algorithm to help them define an optimal 4-digit NACA airfoil. All of these examples resulted in new streamlined shapes, with the primary purpose of improving the aerodynamic efficiency of the 3D body [86].

5.2.1 **Airfoil optimization**

Future HALE/HAPS UAV development largely depends on the design of its major lifting surface, such as a wing. Aerodynamic shape optimization, alternatively referred to as aerodynamic design optimization, is a technique for optimizing the shape of a body (such as an airfoil or wing) in order to increase its performance. The goal, in this case, is to design an ideal airfoil that is both efficient and aerodynamically sound by utilizing CST parameterization and a genetic algorithm.

5.2.2 **CST parameterization**

In the design of aircraft wings and propeller blades, evolutionary algorithms for airfoil optimization have become popular. In order to accomplish satisfactory optimization, airfoil forms are often generated as compound curves or splines that must be parameterized in a straightforward and smooth manner. Although other parameterization approaches are also employed, the class-shape transformation (CST) proposed by Boeing employee Brenda Kulfan [101] is extensively used due to its simplicity, robustness, and ability to generalize various conceivable shapes of aerodynamic bodies.

In short, this method has two parts: a class function that generalizes different two-dimensional airfoils and three-dimensional body shapes, and an analytic shape function that allows easy control of the critical design parameters (leading-edge radius, trailing edge boat tail angle etc.) of the airfoil.

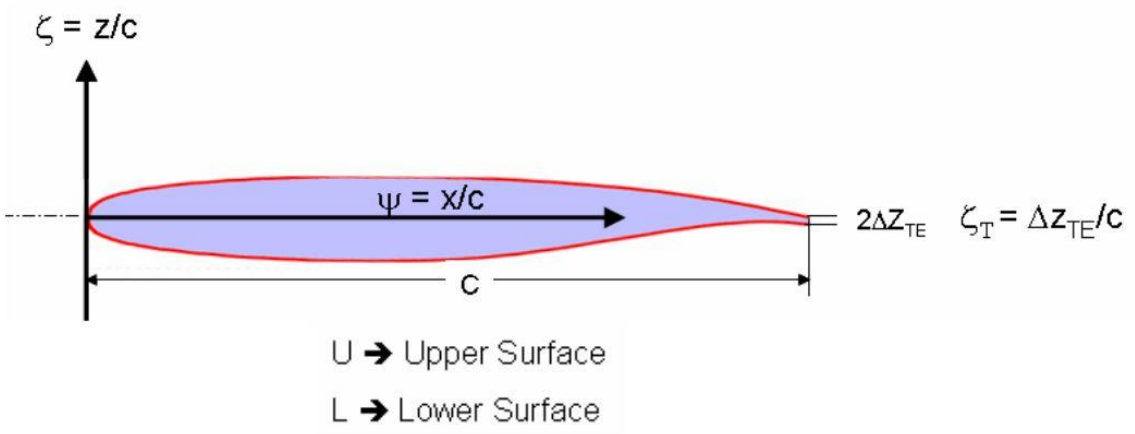

Figure 5- 5: A typical wing airfoil section [101]

The general equation that represents the typical airfoil geometry shown in figure 5-5 can be written as:

$$\zeta(\psi) = \sqrt{\psi}(1-\psi)\sum_{i=0}^{N} A_i \psi^i + \psi\zeta_T, \tag{19}$$

where $\psi = x/c$, $\zeta = z/c$ and $\zeta_T = \Delta\zeta_{TE}/c$.

The terms $\psi^{1/2}$ and $(1-\psi)$ insure round nose and a sharp trailing edge respectively,

$\psi\zeta_T$ allows to control the thickness of the trailing edge and

$\sum_{i=0}^{N} A_i\psi^i$ represents a general feature that defines the distinct geometry between the round nose and the sharp aft end.

The term $\psi^{1/2}(1-\psi)$ is the class-function and it can be defined as:

$$C_{N_2}^{N_1}(\psi) = \psi^{N_1}(1-\psi)^{N_2}. \tag{20}$$

The values N_1 and N_2 define whether the airfoil nose and tail are round or pinpointed. If N_1 is 0.5, airfoil nose shape is round, whereas its end is pinpointed if the value of N_2 is 1.

The shape function is obtained by a Bernstein polynomial, Eq. 21, and a set of curvature coefficients for a given airfoil that scale the corresponding binomial coefficients:

$$S(\psi, i) = K_i^N \psi^i (1-\psi)^{N-i}. \tag{21}$$

The following are some of the especially convenient and efficient properties of using Bernstein polynomials to describe an airfoil:

- This airfoil representation technique captures the entire design space of geometrically smooth airfoils,
- The unit form factor airfoil can be used to build any airfoil in the design space,
- As a consequence, every airfoil in the design space can be derived from any other airfoil.

The degree of polynomials in this example was $N = 2$, implying that each pressure and suction side of the airfoil was defined by three coefficients of negative and positive values for a total of six input parameters. The ranges of potential absolute values for the three input coefficients are constrained, implicitly limiting the airfoil's minimal and maximal relative thicknesses to 6% and 35%, respectively. This factor is taken into account in order to create geometrically viable designs that are also structurally sound. The defined shape of the airfoil may then be described by a large number of pairs of points (e.g., 100) where x-coordinates were generated by cosine distribution to better represent the leading and trailing edges and z-coordinates were computed as mentioned before [86].

5.2.3 **Genetic algorithm**

There are many different algorithms available to discover the optimal solution, which can be divided into two categories: gradient-based algorithms and non-gradient algorithms. Genetic algorithms

(GA), which are non-gradient based algorithms, have been used successfully to address single and multi-objective optimization problems [102]. Although gradient-based methods outperform non-gradient-based methods in a local search, the optimum discovered using these methods is not always the global optimum, especially for aerodynamic designs. Genetic Algorithms (GAs), on the other hand, are more likely to find a global optimum, making them suited for optimizing aerodynamic design [103]. The fundamental principles of GAs were first laid out in detail by Holland in 1960 and have subsequently been clearly defined by a number of experts. GAs are adaptive optimization approaches derived from biological organisms' genetic processes. The "survival of the fittest" principle is used in this technique. They primarily simulate processes that are required for evolution to occur. These algorithms favour those who have a higher chance of survival (i. e., individuals capable of providing solutions to a given problem). The most productive individuals attract other mates and have a large number of offspring. A fitness function scores each individual based on its effectiveness in solving the problem. Various selection approaches are employed to avoid the optimization procedure from converging to a local minimum or a sub-optimal solution. Among the most popular are uniforms, roulette, and tournaments [104]. Many optimization algorithms are now available in programming systems such as MATLAB.

With respect to the number of input parameters, the population numbered 400 entities. More than 1000 generations were formed, resulting in nearly 400000 individual computations.

As previously mentioned, each considered entity was defined by 6 coefficients that served to define the shape of the airfoil whose aerodynamic characteristics at 0.20 *MRe* were computed by XFOIL [99].

In order to perform multi-objective optimization, two distinct objective functions whose maximal values are sought were defined, best glide ratio and best maximal lift coefficient:

$$\max\left(C_L/C_D\right) \wedge \max\left(C_{L,\max}\right). \tag{22}$$

A more comprehensive overview of GA is given in [104], [105].

5.2.4 **Computational model validation**

To determine the validity of the adopted computational approach as well as the usefulness of the optimized airfoils, the numerical results obtained by XFOIL [99] (a relatively simple but very useful and powerful solver, particularly applicable to low *Re* airfoils, based on panel methods and enhanced by various semi-empirical corrections capable of sufficiently accurately describing viscous flow in

the vicinity of walls, laminar separation bubble, etc.) were first examined (that is designed for small speeds and Reynolds numbers and is illustrated in Figure 5-6). A thorough description of the experimental investigation that was carried out may be found in [106].

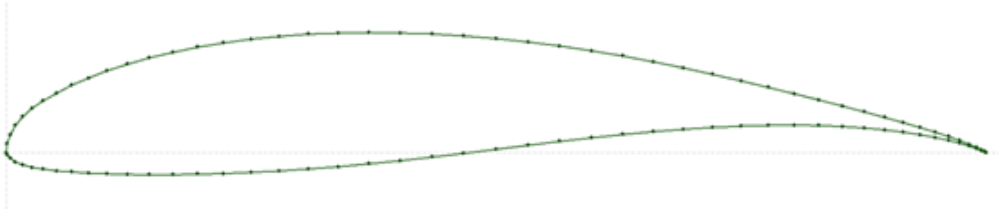

Figure 5- 6: Airfoil FX 63-137 [86]

FX 63-137 airfoil lift and drag coefficient curves are shown in figure 5-7, which includes both numerical and experimental data. As expected, the numerical data are a little overestimated because of the high curvature of the airfoil. While the measured numerical drag coefficient is lower for smaller angles of attack, the numerical lift gradient is higher. However, the tendency of both curves is well represented, and the overall agreement is good, showing that XFOIL can be utilized in preliminary optimization studies, as long as the researcher understands that not all geometric aspects or viscosity effects can be accurately simulated. Furthermore, the maximal lift coefficient and critical angle-of-attack are slightly underestimated at high angles of attack, whilst the total drag coefficient is significantly overestimated. Both of these statements suggest that for high angles of attack, the computed glide ratio remains on the safe side [86].

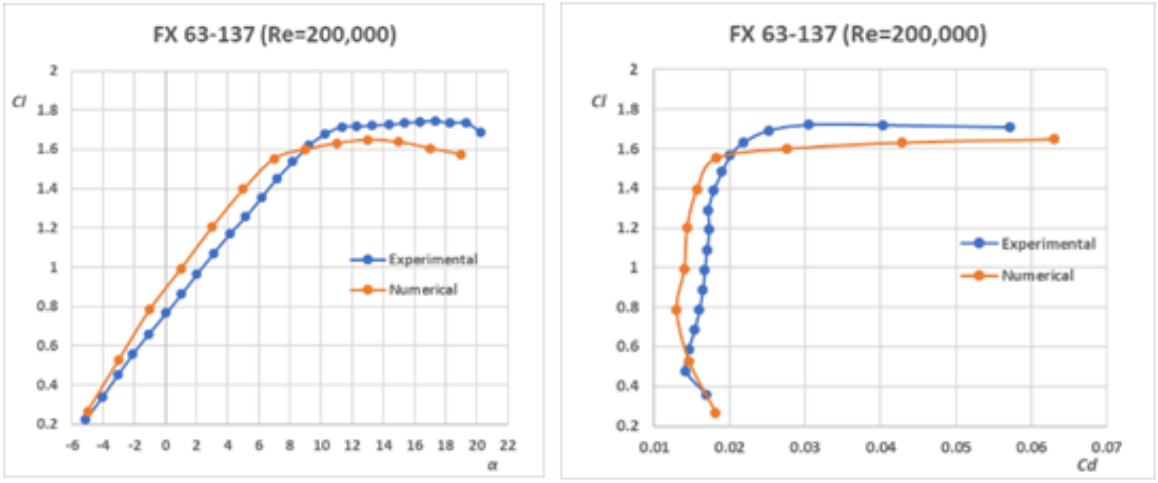

Figure 5- 7: Lift and drag coefficient curves of airfoil FX 63-137 [86]

5.2.5 **Optimized 2D airfoils**

Figure 5-8 depicts the calculated Pareto front, as well as the values of the last generation's target functions. It can be observed that excellent airfoil aerodynamic performance appears to be feasible

with two-criteria optimization. The maximum lift-to-drag (or glide) ratio C_l/C_d is approximately 88, whereas the maximum lift coefficient $C_{l,\max}$ is 1.67. Of course, both goals cannot be met at the same time, thus a compromise or a choice between the two must be made. Greater lift-to-drag means longer endurance and lower height loss throughout the night in the case of HAPS, and can thus be chosen as the major norm for picking an optimal airfoil from the resulting Pareto set [86].

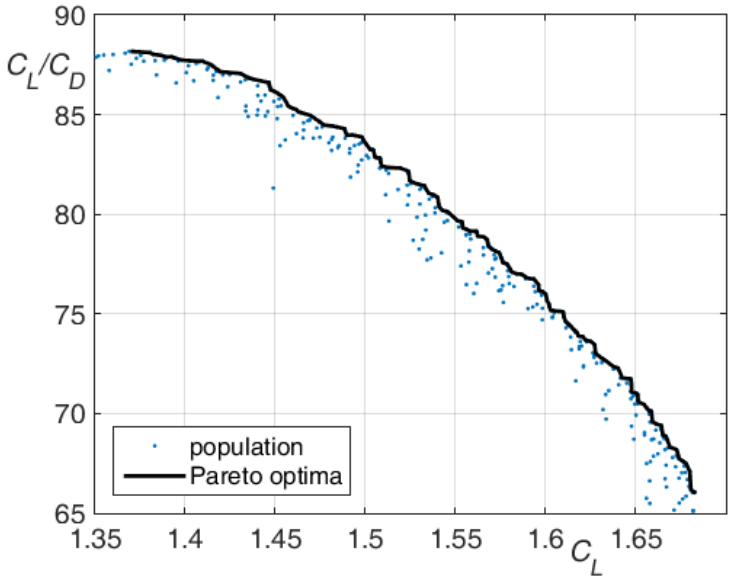

Figure 5- 8: Obtained Pareto front [86]

Three airfoils were chosen for comparative analysis in order to better understand the properties of the Pareto set. Airfoil-1 has the best glide ratio, Airfoil-3 has the highest maximal lift coefficient, and Airfoil-2 is in the middle. Table 11 lists their geometric characteristics (maximal relative thickness $(t/l)_{\max}$ and its relative position, maximal relative curvature $(c/l)_{\max}$ and its relative position), whereas figures 5-9 and 5-10 show their shape and aerodynamic performance.

Table 11**.** Geometric properties of chosen airfoils [86]

	$(t/l)_{\max}$ [%]	at x/l [%]	$(c/l)_{\max}$ [%]	at x/l [%]
Airfoil-1	12.36	34.53	4.87	46.95
Airfoil-2	14.00	31.53	5.55	43.74
Airfoil-3	15.97	28.73	6.59	37.54
FX 63-137	13.71	30.83	5.97	53.35

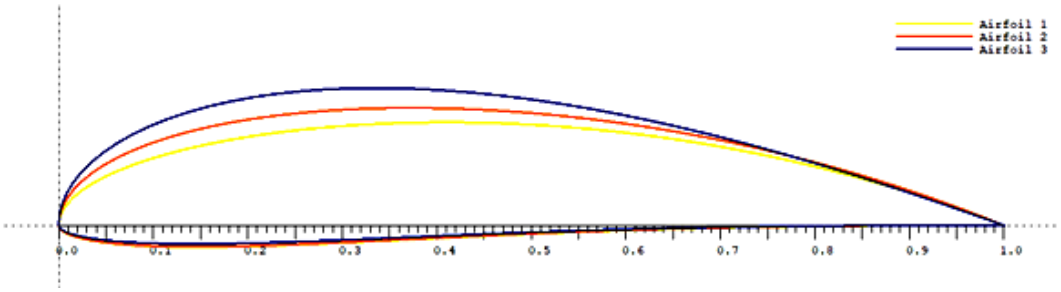

Figure 5- 9: Contours of chosen airfoils [86]

Surprisingly, the airfoils differ mostly in their suction shape (causing thickness and curvature variances), while their lower surfaces are nearly identical. As previously stated, Airfoil-3 has the highest maximum lift coefficient ($C_{L,max}$ = 1.65), whereas Airfoil-2 and Airfoil-1 have values of 1.55 and 1.45, respectively. On the other hand, all three airfoils behave well near stall because there are no sudden shifts or large lift losses at high angles of attack.

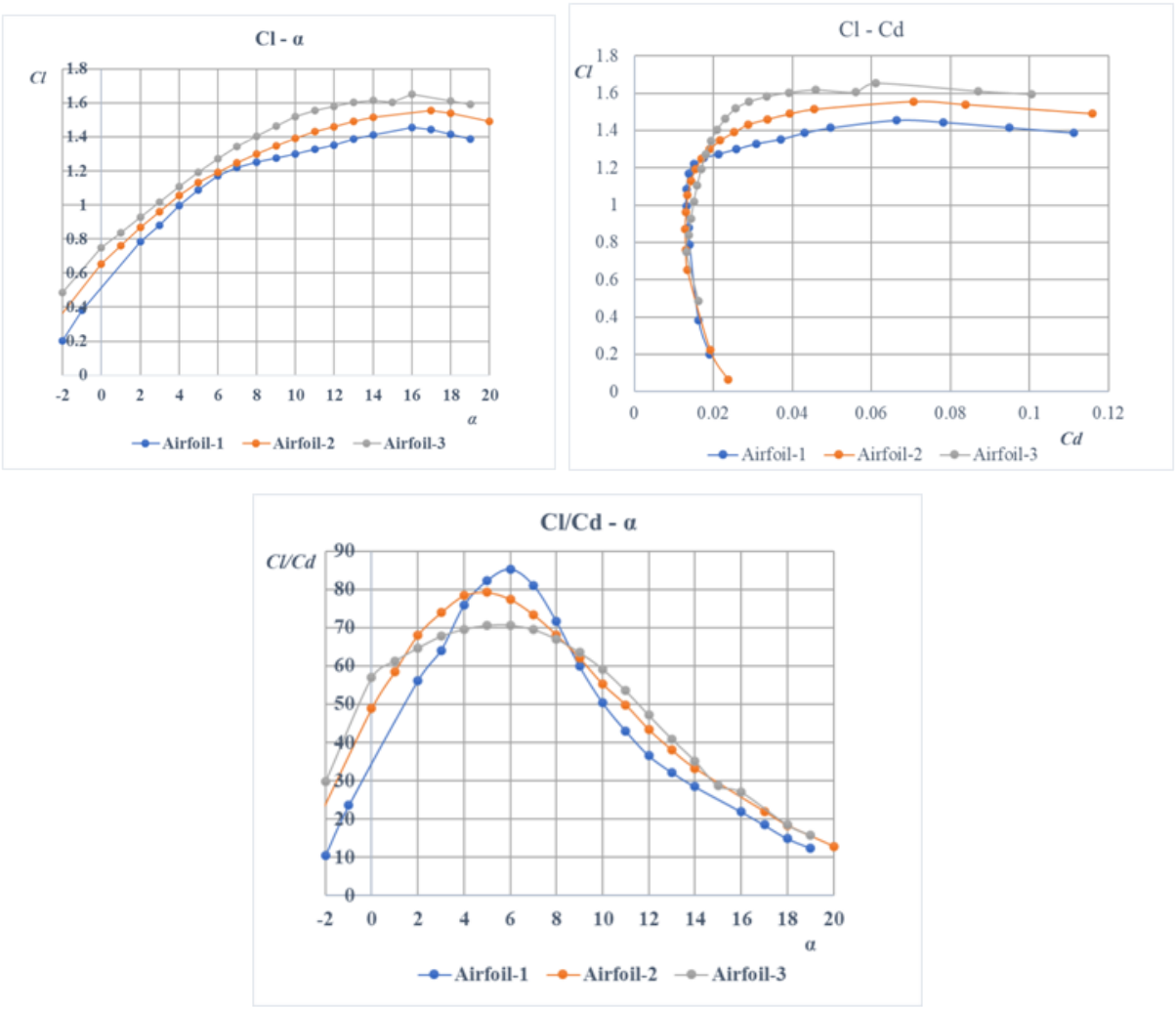

Figure 5- 10: Aerodynamic performances of chosen airfoils [86]

Drag coefficients of all three airfoils are in the range [0.013, 0.020] for medium angles of attack ($3° \leq \alpha \leq 8°$), which is acceptable, whereas rapid drag rise occurs at $\alpha > 10°$. For $3° \leq \alpha \leq 8°$, the estimated glide ratios of airfoils 1, 2, and 3 are roughly 85 (which is extremely desirable), 79, and 70, respectively. Although the presented results are based on simplified 2D analyses and will undoubtedly be reduced when applied to a 3D wing, they are intriguing and indicate in the direction of optimal wing geometry specifically built for HAPS. Therefore, for the two-segmented wing design and more extensive investigation, Airfoil-1 with the highest glide ratio is chosen [86].

So, after both XLRF and Optimization Airfoil S1210 and Airfoil 1 were selected for further analysis. Although the characteristics of airfoil S 1210 seem much better in comparison to the optimized airfoil, the true quality of both airfoils will become apparent after considering the fluid flow around 3D wing.

Table 12. Maximum lift coefficient and glide ratio of two selected airfoils [86,89]

Airfoil	C_{lmax}	$(C_l/C_d)_{max}$ at $(3° \leq \alpha \leq 8°)$
S 1210	1.95	95
Optimized airfoil (1)	1.45	85

6 Wing design and aerodynamic analysis

The wing configuration of unmanned aerial vehicles is critical throughout the design stage. It has already been said that the HAPS take-off weight is 150 kg, and its main lifting surface must be able to generate enough lift force to keep the plane in the air or allow it to glide at a height of 20 km. Aside from being the most efficient and least expensive to construct, the wing should have the maximum usable surface available (allowing for as much as possible solar panels to be installed). All of these considerations led to the selection of a wing with a high aspect ratio. The use of this type of wing can help to reduce the negative effects of induced drag on the aircraft (i.e., the vortices separating from the wing tips).

Two types of high aspect-ratio wings were studied in this study, and the wing with the best aerodynamic properties was chosen. Both forms of wings are commonly used in the development of long-endurance aircraft. It is intended that both wings be untwisted since its stalling characteristics can directly be related to the airfoil stalling characteristics, which seem to be satisfactory, as previously illustrated in Figures 5-4 and 5-10. Simultaneously, the production of an untwisted composite wing is much easier than that of a twisted composite wing and can be done in segments from the same mould.

6.1 One segmented or constant chord wing

The simplest basic wing planform is a constant-chord wing. Constant-chord wings are fairly common on light planes. Despite having a lower aerodynamic performance, they have a significant advantage: all of the ribs are the same length and the spars are the same height. As a result, they cost less to develop and construct. Catia v5 is used to model a one-segmented wing with wingspan, b = 33.01 [m], taper ratio = 1, chord, c = 1.50 [m], and airfoil = S 1210.

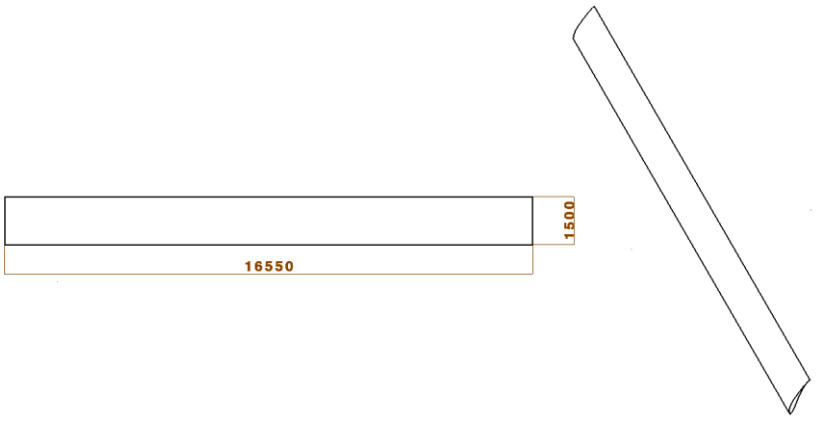

Figure 6- 1: One-segmented wing

6.2 Two-segmented wing

Because of their high aspect ratios and structural elasticity, polyhedral wings are used on the majority of solar-powered HAPS UAVs because they are prone to deform (i.e. bend) extensively in flight under aerodynamic loads. A multi-sectioned wing is highly stable in roll and yawing, and it quickly achieves static equilibrium in level flight. A two-section wing with an inner rectangular and an outer trapezoid section with a dihedral tip is built and modelled in this section, and its performance is investigated. The outer wing segment is also tapered to improve span-wise load distribution. The taper ratio is close to 0.6, which is suggested for untwisted wings.

The half-span of the designed two-segmented wing is *b/2* = 16.55 m, where the first rectangular segment is 11.05 m long and its chord length is 1.50 m (as demonstrated in Figure. 6-2). The wing reference area is approximately 46.5 m^2. In order to cruise at 25 m/s velocity and 20 km altitude, the wing should achieve a lift coefficient close to 1. The taper ratio of the outer trapezoid segment is 0.6 while its dihedral angle is set to 10.44°.

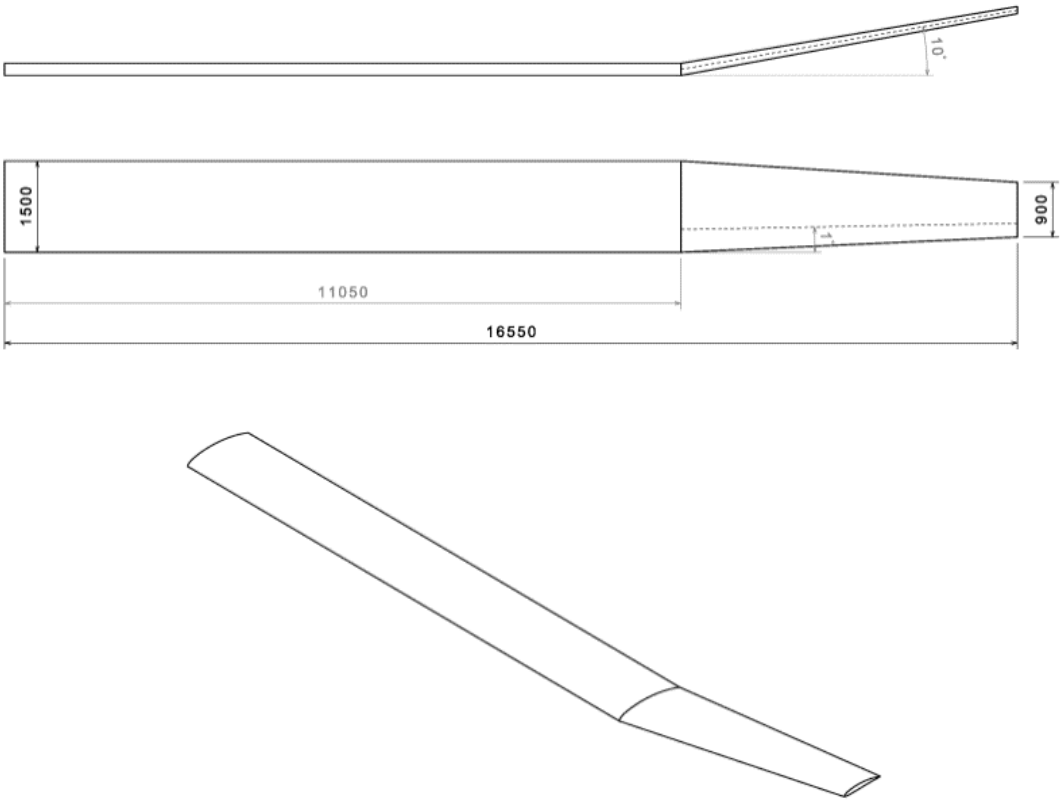

Figure 6- 2: Geometric features of the designed wing [86]

6.3 Aerodynamic performance analysis

6.3.1 Reynolds models of turbulence

One of the ways to solve turbulent - chaotic, very non-stationary and irregular flow, which is perhaps the optimum between the complexity of the problem and the possibility of solving it as well as the time needed to solve, is the introduction of Reynolds statistics of averaging over time. The flow equations are now solved by the mean values of the flow parameters. Substituting expressions of this form for the flow variables into the instantaneous continuity and momentum equations and taking a time average yield the ensemble-averaged momentum equation. They can be written in Cartesian tensor form as:

$$\frac{\partial \rho}{\partial t} + \frac{\partial}{\partial x_i}(\rho \overline{v_i}) = 0 \tag{23}$$

$$\begin{aligned} &\frac{\partial}{\partial t}(\rho \overline{v_i}) + \frac{\partial}{\partial x_j}\left(\rho \overline{v_i}\,\overline{v_j}\right) \\ &\qquad = \rho \overline{F_i} - \frac{\partial \bar{p}}{\partial x_i} + \frac{\partial}{\partial x_j}\left[\mu\left(\frac{\partial \overline{v_i}}{\partial x_j} + \frac{\partial \overline{v_j}}{\partial x_i} - \frac{2}{3}\delta_{ij}\frac{\partial \overline{v_K}}{\partial x_k}\right)\right] \\ &\qquad + \frac{\partial}{\partial x_j}\left(-\rho \overline{v_i' v_j'}\right) \end{aligned} \tag{24}$$

Equation 23 and Equation 24 are called Reynolds-averaged Navier-Stokes (RANS) equations. They have the same general form as the instantaneous Navier-Stokes equations, with the velocities and other solution variables now representing ensemble-averaged (or time-averaged) values. Additional terms now appear that represent the effects of turbulence. These Reynolds stresses, $-\rho \overline{v_i' v_j'}$, must be modeled in order to close Equation 24. The Reynolds-averaged approach to turbulence modeling requires that the Reynolds stresses in Equation 24 are appropriately modeled. A common method employs the Boussinesq hypothesis to relate the Reynolds stresses to the mean velocity gradients:

$$-\rho \overline{v_i' v_j'} = \mu_t\left(\frac{\partial \overline{v_i}}{\partial x_j} + \frac{\partial \overline{v_j}}{\partial x_i}\right) - \frac{2}{3}\left(\rho k + \mu_t \frac{\partial \overline{v_K}}{\partial x_k}\right)\delta_{ij} \tag{25}$$

$$k = \frac{\overline{v'^2}}{2} = \frac{\overline{{v'_x}^2 + {v'_y}^2 + {v'_z}^2}}{2} \tag{26}$$

The dependence of turbulent stresses on mean velocity gradients is expressed by turbulent viscosity μ_t, which is now a characteristic of flow, not fluid. The advantage of this hypothesis is that it is relatively easy to calculate. However, turbulent viscosity is considered an isotropic quantity, which is not the case in all technical problems.

In order for the total flow energy to be taken into account, magnitude *k* appears in the equation 25, which is the turbulence kinetic energy. In general, most Reynolds turbulent models analyze and solve the equation of kinetic energy of turbulence, and they differ in another quantity that is defined, such as turbulence dissipation rate, ε, or specific dissipation rate, ω.

It was mentioned earlier that the problem of turbulent flow is still not completely solved. There is no universal turbulence model, especially when considering averages, because calculating the entire flow field is still generally unprofitable and demands a lot of computational power. For these reasons, there are a large number of models that are more or less appropriate, depending on the specific problem. The two models used in this dissertation are *k-ω SST* and transition *SST*.

6.3.2 **Shear-Stress Transport (SST) *k-ω* model**

This model is a combination of the standard *k-ω* model near the wall and the *k-ε* model in the rest of the computational domain. It is generally more reliable and accurate than the standard *k-ω* model for a number of flow classes. Transport equations are of the following form:

$$\frac{\partial}{\partial t}(\rho k) + \frac{\partial}{\partial x_j}(\rho k v_j) = \frac{\partial}{\partial x_j}\left(\left(\mu + \frac{\mu_t}{\sigma_k}\right)\frac{\partial k}{\partial x_j}\right) + \mu_t S^2 - \rho\beta^* k\omega \tag{27}$$

$$\frac{\partial}{\partial t}(\rho\omega) + \frac{\partial}{\partial x_j}(\rho\omega v_j) = \frac{\partial}{\partial x_j}\left(\left(\mu + \frac{\mu_t}{\sigma_k}\right)\frac{\partial k}{\partial x_j}\right) + \frac{\alpha}{\nu_t}\mu_t S^2 - \rho\beta\omega^2 + D_w\left(\omega, \frac{\partial k}{\partial x_j}, \frac{\partial \omega}{\partial x_j}\right) \tag{28}$$

- $\mu_t S^2$; the generation of turbulent kinetic energy and *S* is the modulus of the mean rate-of-strain tensor

- $\rho\beta^* k\omega$; dissipation of turbulence kinetic energy

- $\rho\beta\omega^2$; dissipation of ω,

- $D_w\left(\omega, \frac{\partial k}{\partial x_j}, \frac{\partial \omega}{\partial x_j}\right)$; represents a function that regulates the transition from the *k-ω* model near the wall to the *k-ε* model in the rest of the computational domain.

For additional information of SST *k-ω* model can be found in ANSYS FLUENT Theory Guide [107].

6.3.3 **Transition SST model**

This is a four-equation model specially developed to cover standard bypass transition as well as flows in low freestream turbulence environments. It derives from the *k-ω* SST model with two additional equations for intermittency γ, the ratio of laminarity and turbulence of the flow, and for the transition onset criteria, in terms of momentum-thickness Reynolds number $Re_{\theta t}$. The transport equations are of the following form:

$$\frac{\partial}{\partial t}(\rho\gamma) + \frac{\partial}{\partial x_j}(\rho\gamma v_j) = \frac{\partial}{\partial x_j}\left(\left(\mu + \frac{\mu_t}{\sigma_k}\right)\frac{\partial\gamma}{\partial x_j}\right) + P_\gamma - E_\gamma \tag{29}$$

$$\frac{\partial}{\partial t}(\rho R\tilde{e}_{\theta t}) + \frac{\partial}{\partial x_j}(\rho R\tilde{e}_{\theta t} v_j) = \frac{\partial}{\partial x_j}\left(\sigma_{\theta t}(\mu + \mu_t)\frac{\partial R\tilde{e}_{\theta t}}{\partial x_j}\right) + P_{\theta t} \tag{30}$$

The first additional equation governs the start of the change of flow regime, while the second equation governs the impacts of the external flow in the boundary layer. The original term $P\gamma$ is equal to zero in the laminar boundary layer, and changes when the criterion of the beginning of the regime change is satisfied. The term E_γ ensures that the value of γ is close to zero in the laminar boundary layer and establishes a laminarization of the flow when the selected criterion is no longer met, and finally disappears in a completely turbulent boundary layer. The term $P_{\theta t}$ ensures that the empirical criterion matches outside and within the boundary layer. The final coupling of the two pairs of equations is achieved by a small modification of the original term of the kinetic energy of turbulence which is now a function of intermittency [107].

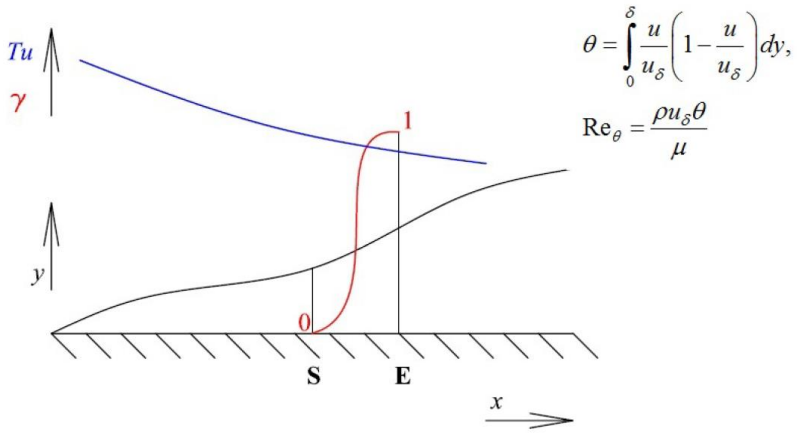

Figure 6- 3: Change in turbulent quantities in the transition region [107]

6.4 One segmented wing analysis

A three-stage approach was used to conduct the numerical analysis: pre-processing, processing, and post-processing. The pre-processing step included geometry and meshing generation and setup. Using the commercial ANSYS software, a computational model based on the S-1210 airfoil was developed. Initially, the grid was created using Ansys Meshing. A rounded semi-cylinder domain was constructed around the wing, with an arc radius of 2*b* from the leading edge and the wing's outlet is 100 meters aft the leading edge. It is advised to extend the outlet limit as much as possible. Inflation of 20 layers with a growth rate of 1.2 was used to refine the mesh around the wing surface locally. Feature inflation layers on the wing surface generate high aspect ratio cells, which are ideal for capturing areas where the airflow is subjected to rapid changes in critical variables, such as within the boundary layer. Different edge sizes were employed for the wing's root and tip airfoils and the leading and trailing edges. Eventually, a mesh of 944000 cells was generated. Even though this is a medium-fine mesh, it is appropriate for the conceptual design stage. Figure 6-4 depicts the domain grid model as well as the mesh details around the wing.

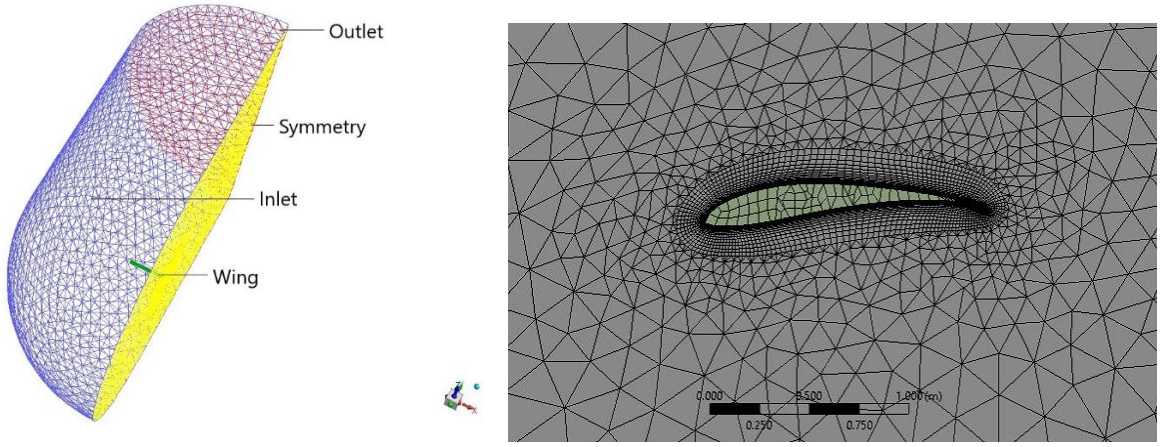

(a) (b)

Figure 6- 4: (a) 3D domain grid model, (b) meshing around wing [89]

6.4.1 Simulation and analysis of the wing flow field

After checking the grid, a pressure-based steady-state solver is chosen since it is better suited to incompressible flow. The *k-ω* SST and the transition SST turbulence models were used to check which model gives more realistic results. Both of these models have been thoroughly validated and developed for aerodynamic applications, with the transition SST model solving two more equations compared to the *k-ω* SST model and assuming partly laminar flow that transitions to transitional and eventually turbulent flow. As a result, it is ideal for low-speed flows around laminar airfoils. For *k-ω* SST, the SIMPLE pressure velocity coupling approach was used. The SIMPLEC approach, on the

other hand, was used for the transition SST model, and both simulations were performed with 2nd order accuracy of numerical schemes.

At operational altitude (h = 20 km), the fluid's physical properties and boundary conditions are studied. In order to obtain the design lift coefficient (C_L =1.08) for a given angle of attack (AoA), simulations were carried out. The design lift coefficient (C_L =1.08) corresponds to the required UAV mass of 150 kg. The inlet velocity was held constant at 25 m/s. Both computations lasted/were performed for 2000 iterations.

The pressure contours were generated from the post-processing stage following the simulations. The pressure contours on the wing surface for the *k-ω* SST and transition SST models are shown in Figure 6-5. Table 13 displays the C_L values for several AoA and the two turbulent models [89].

Table 13**.** Aerodynamic coefficients of wing 11 at operating conditions from Ansys fluent and XFLR5 for different AOA [89]

Program	Model	AOA [º]	C_L	C_D	C_L/C_D	Force [N]	Mass [kg]
ANSYS	Transition SST	2.8	1.08	0.043	25.11	1480	150.86
	Transition SST	3.3	1.13	0.045	24.74	1538	156.75
	k-ω SST	3.2	1.08	0.050	21.60	1482	151.07
	k-ω SST	2.3	0.999	0.045	22.20	1360	138.60
XFLR5	Ring Vortex (VLM2)	2.8	1.288	0.043	29.95	1471	150.00

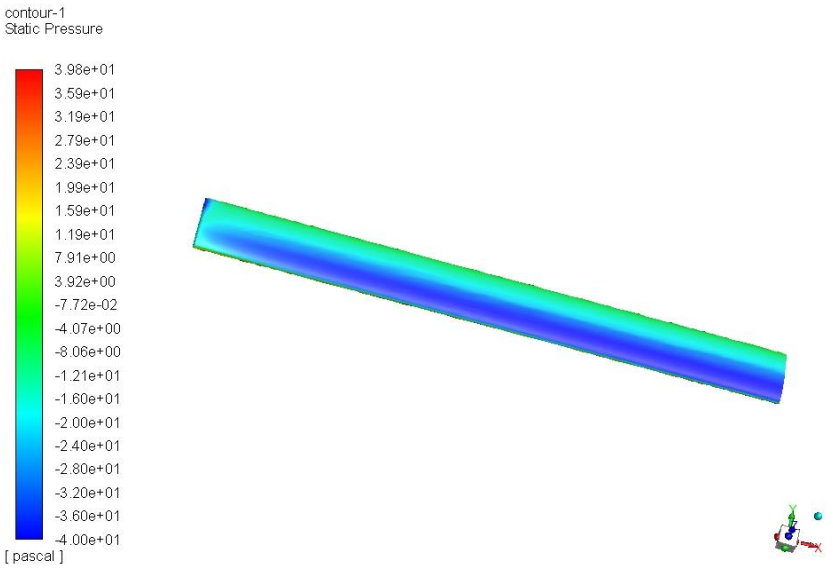

(a)

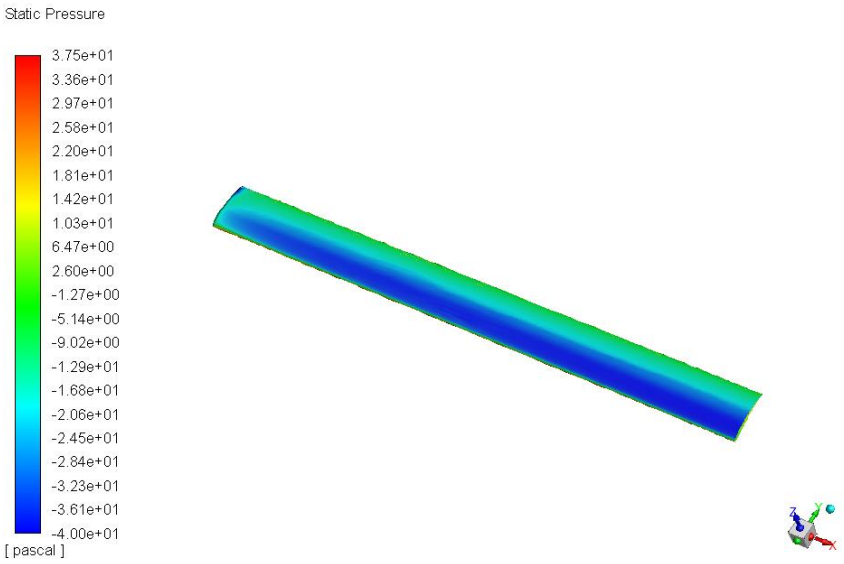

(b)

Figure 6- 5: Pressure contours of (a) SST *k-w* and (b) Transition SST model [89]

The pressure distributions along the upper wing surface generated by the two turbulence models are similar, as shown in figure 6-5. Blue zones of negative gauge pressure cover most of the leading part of the wing, with modest losses appearing at the wing tips. Because of the wing's high aspect ratio, induced drag is low, and pressure distribution is nearly uniform across the span.

However, despite the fact that deviations in pressure distributions are almost imperceptible, the values of the lift-to-drag ratio shown in table 13 show that the assumption of partially laminar flow improves computed aerodynamic characteristics by about 15%. The high value of $C_L/C_D > 25$ attained via transition SST is most satisfactory since it reduces the necessary thrust (and thus power) that the electrically-driven propellers must generate (and spend). It is also quite similar to the value found by XFLR5, which utilizes the simplest numerical model, makes the most flow simplifications, and does not account for all of the viscous drag that occurs in reality.

6.5 Two segmented wing analyses

The same simulation software (Ansys) simulates the two-segmented wing. A quarter-sphere with a radius of 2*b* and a half-cylinder that spans 100 m aft of the wing's leading edge are used to make the computational domain around the half-wing. The generated mesh is a hybrid unstructured mesh. To locally improve the mesh surrounding the wing surface, 20 layers of inflation with a growth rate of 1.2 were used. In addition, different edge sizing functions were assigned to the root and tip airfoils, as well as the leading and trailing edges of the wing. Eventually, a fine mesh of 4651546 components was generated to increase the reliability of flow simulations. Figure 6-6 depicts the domain model as well as the mesh details around the wing.

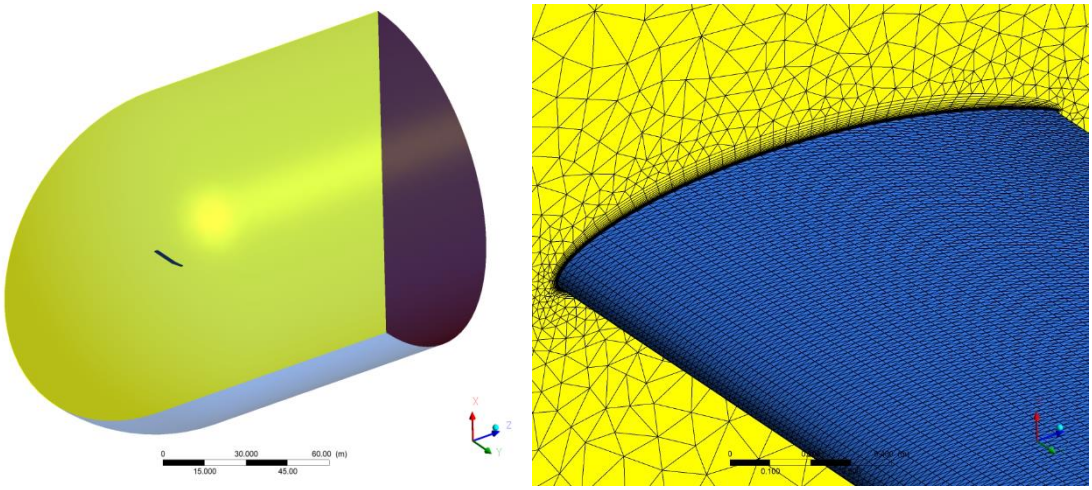

Figure 6- 6. Computational domain and detail of the generated mesh [86]

6.5.1 Simulation and analysis

The finite volume approach solves mass, momentum, and energy conservation equations in ANSYS FLUENT [107], which is used to analyze wing aerodynamic performance. The fluid flow is considered 3D and steady, and the pressure-based solver is chosen because it is better suited to incompressible flow.

At an operational altitude of h = 20 km, the physical properties of the air, as well as the boundary conditions, are taken into account. Simulations were carried out for five different angles of attack (AoA), with the input velocity maintained at 25 m/s and the outlet pressure assumed to be zero gauge pressure. A well-proven *transition SST* turbulence model is used to close flow equations [100], same as in the previous section.

The computed aerodynamic performances of the designed wing is depicted in Figure 6-7. Despite the fact that the maximum glide ratio C_L/C_D is significantly lower than the previously determined airfoil

value, its value of almost 32 is still suitable for three-dimensional geometry. This is mostly due to the significantly higher viscous drag, although the wing lift coefficient curve closely approaches its 2D counterpart. In addition, moderate lift loss and steady behaviour at higher angles of attack are kept, which is essential for aircraft safety. The lift-to-drag ratio will be reduced even further when propellers and vertical tail surfaces are added. It is also worth noting that the lift coefficient of 0.5 to 1 required for cruise at altitudes of 15 km and 20 km, respectively, can be accomplished with angles-of-attack in the [1°, 6°] range.

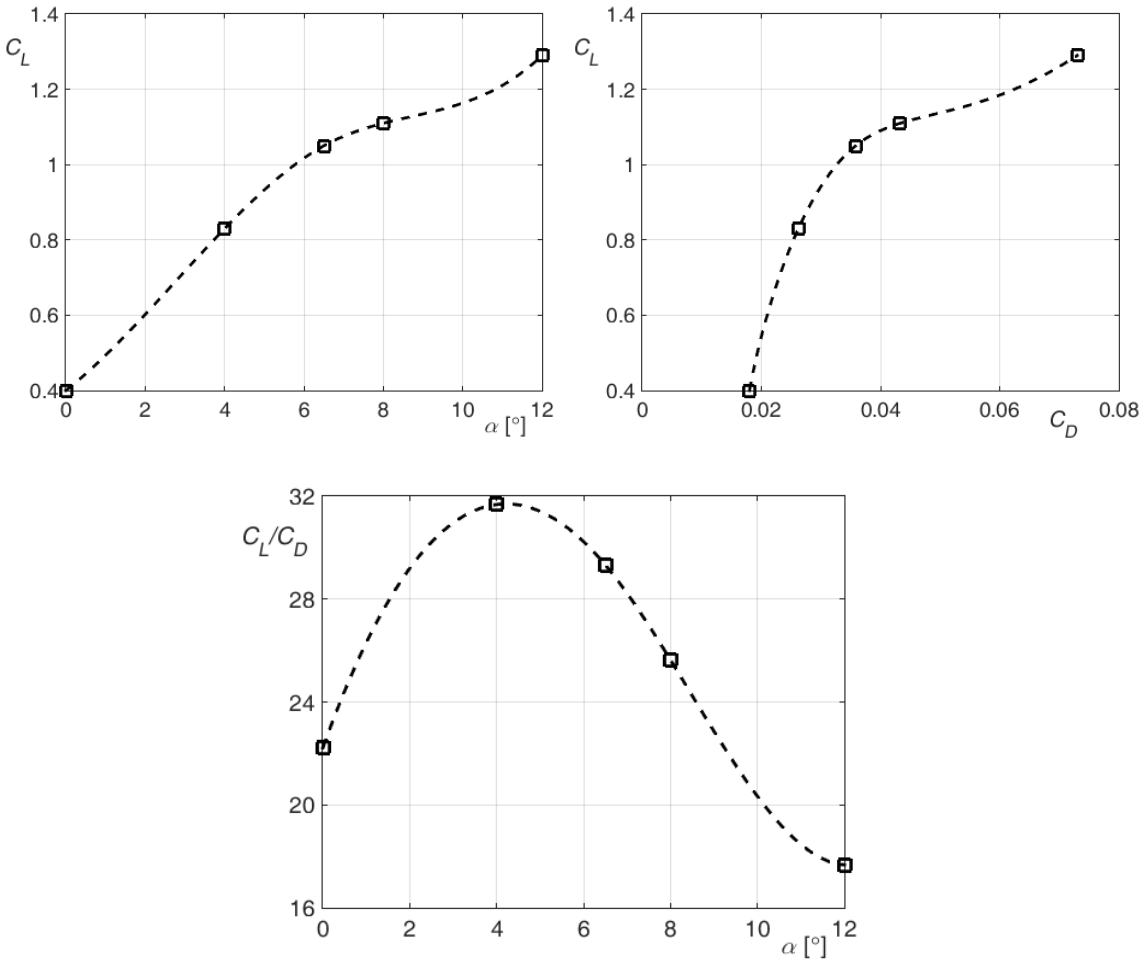

Figure 6- 7. Computed wing aerodynamic performances [86]

More flow analysis and visualization can be performed. Pressure coefficient distributions in four cross-sections (y = 0 m, y = 5 m, y = 10 m, and y = 15 m) show that aerodynamic distributions are favorable in both chord- and span-wise directions. The pressure coefficient distribution is practically consistent along the largest region of the wing (rectangular and for more than half of the trapezoid component), as shown in Figure 6-8. Only the cross-section with a lateral coordinate of y = 15 m (closest to the wing tip) shows a decrease in aerodynamic loads (and associated losses) (closest to the wing tip). Similar results can be drawn by inspecting velocity curves in four cross-sections, as shown

in Figure 6-9. Flow is smooth and attached along the greatest part of the wing, and even laminar at the fore half of the suction surface.

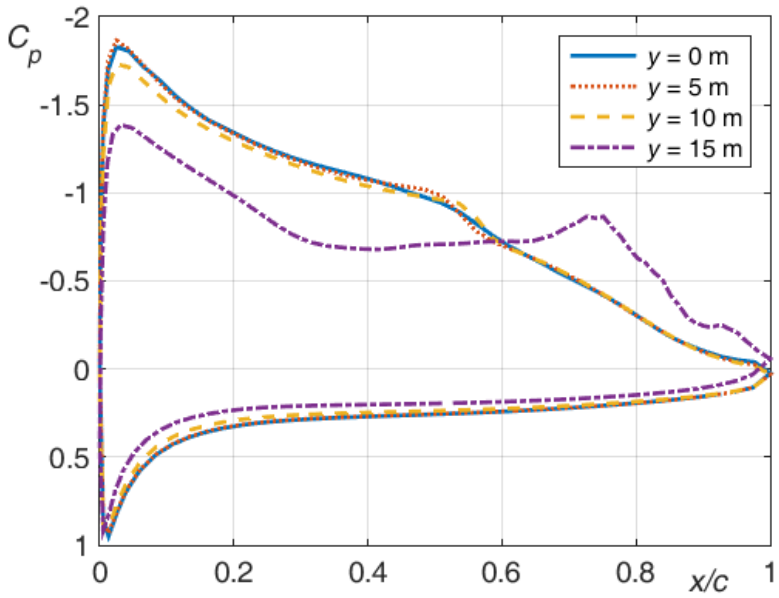

Figure 6- 8. Computed pressure coefficient distributions [86]

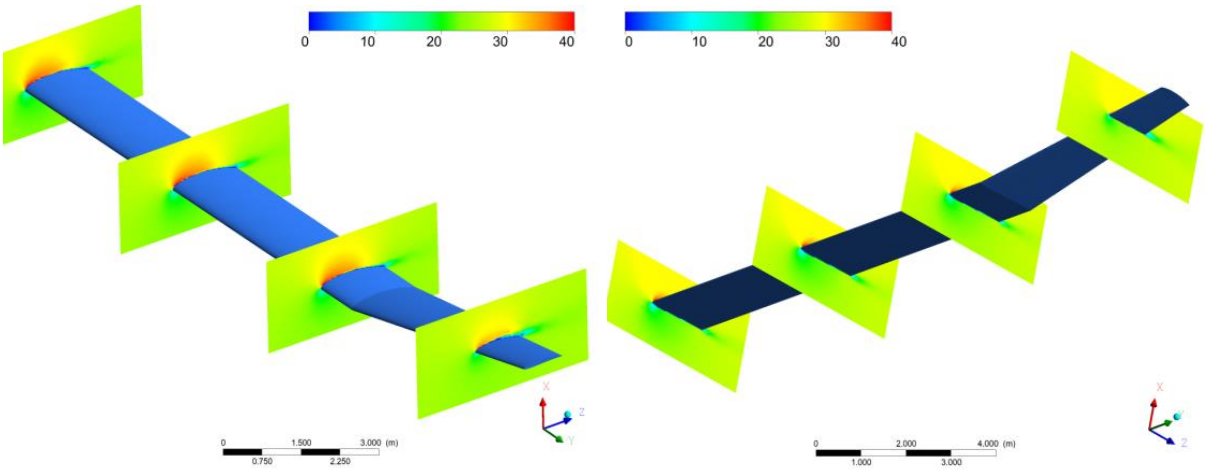

Figure 6- 9. Computed velocity contours [86]

In the cruising regime, as shown in Figure 6-10, streamlines follow the wing surface almost to the trailing edge, while vortical structures and uneven flow exist only near the wing tips, significantly decreasing the induced drag.

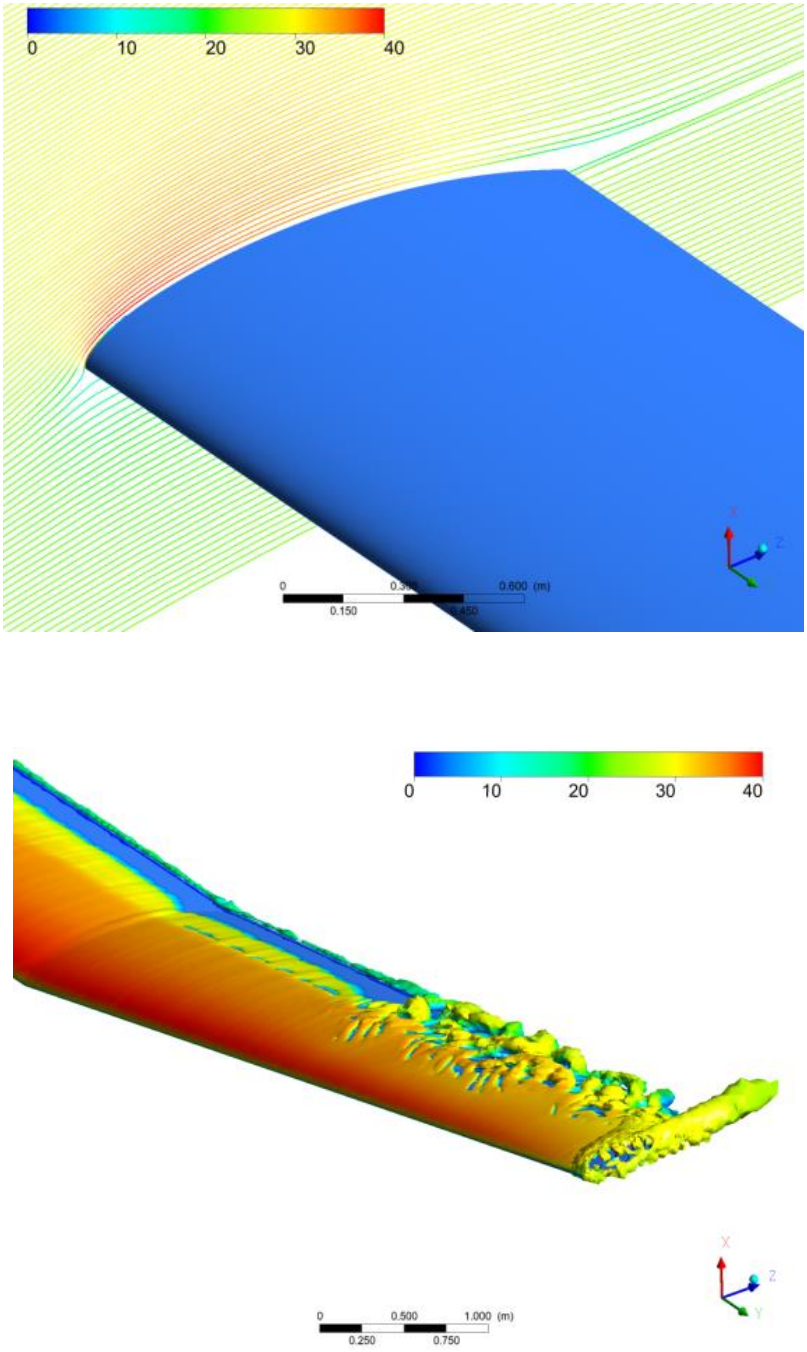

Figure 6- 10. Computed streamlines and vortical structures colored by velocity [86]

7. Wing structural design

Besides having a high aspect ratio wing, low structural weight is also essential to increase the flight endurance. Before designing the wing, it is advised to have a solid grasp of the materials because this can have a significant impact on the aircraft's serviceability. By selecting appropriate materials for different elements of the wing, it is vital to build a light-weight airframe without compromising structural integrity. The most significant advancement in the aircraft industry has been the use of composite materials in airframe construction. Although the HAPS airframe is largely made of composite materials, the use of 3D printed plastic materials in complex structures is also becoming more common.

7.1. Materials

Aircraft materials have come a long way since the early days. Modern aircraft designers have a wide range of high-performance materials from which to choose. The goal is to create a structure with enough strength and stiffness while keeping the weight, cost, and manufacturing effort to a minimum. Wood, steel, aluminum alloys with, more recently, titanium alloys, and fiber-reinforced composites have been the principal materials used in aircraft construction, moreover, the usage of 3D printed plastic materials in some airframe structures is gaining popularity [46]–[48]. To provide outstanding mechanical qualities, complex composite materials that are exceptionally lightweight have been used extensively in solar-powered airplanes (e.g., strength, torsion, flexion, and vibration) [11], [38], [49]–[51].

7.1.1. Composite materials

Composite materials are made up of strong fibres like glass or carbon that are encased in a mechanically and chemically protective matrix of plastic or epoxy resin. The fibres might be continuous or discontinuous, but they have a far higher strength than the bulk materials. The reinforcement is in responsibility of resisting the loads that are applied to the material, while the matrix is responsible of transmitting the loads between reinforcements through shear stresses. In aeronautic applications, the matrix is usually a polymer and the reinforcement is usually non-metallic, more specifically, glass, carbon or aramid (Kevlar).

Depending on the geometry of the reinforcement, composite materials can be classified as: fiber reinforced composite materials, where fibers can be continuous or discontinuous and, regarding their orientations, they can be: random, unidirectional, bidirectional or multidirectional or particle reinforced composite materials. The fiber reinforced composites are usually created by stacking two

or more layers of reinforcement that have been previously impregnated with the matrix (prepreg) or are impregnated during the stacking procedure (hand-lay-up). The stacking procedure is called lamination and each layer is also called a ply. Depending on the matrix material and the mechanical qualities desired, the matrix is cured (hardened) either by leaving it exposed to ambient conditions or by curing it under controlled temperature, humidity, and pressure conditions. In the fiber direction, unidirectional fiber reinforced laminate composites have higher mechanical strength and elastic modulus (*E*) (high stiffness), however these values are substantially lower in the orthogonal direction[108], [109].

Figure 7-1 depicts four popular fiber orientation tailoring configurations. All fibers in part a) are aligned with the principal axis, giving the composite maximum strength in that direction and minimal strength in the others. Arrangement b) is strong in both vertical and horizontal directions.

The fibers in c) are at a 45-degree angle to the primary axis. This gives strength in both of those directions, as well as good shear strength in the principal axis. As a result, this configuration is typical in composite-wing-box shear webs. The 45-degree orientation is also commonly utilized in structures that must withstand torque.

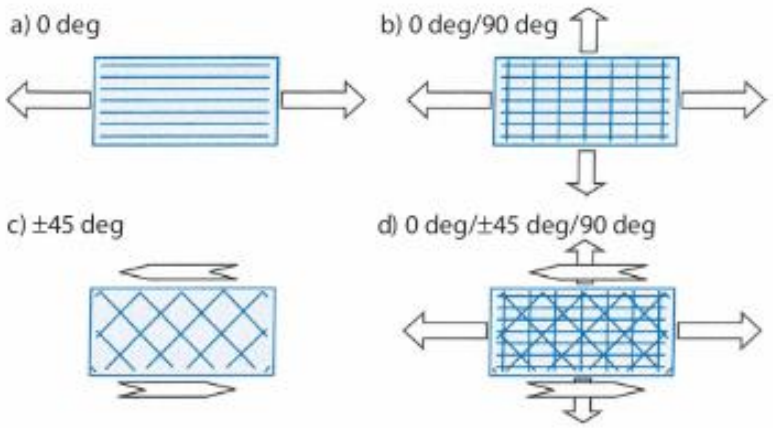

Figure 7- 1: Composite ply orientation [2]

Arrangement d) combines b) and c), resulting in alternate layers (plies) of fibers at 0 degrees, 45 degrees, and 90 degrees. The designer can achieve practically any combination of tensile, compression, and shear strength in any desired direction by altering the number of plies at various orientations. Piles that are 60 degrees apart are used in another ply-orientation system. To achieve unique properties, composites are occasionally made with fully random ply directions [2].

7.1.2 3D printed plastic materials

Fused deposition modeling (FDM) is a popular additive manufacturing (AM) and rapid prototyping (RP) process that has revolutionized the way we construct products. In 1986, Charles Hull first introduced additive manufacturing as a method known as Stereolithography (SLA). Many industries, including aerospace, construction, prototype, and biomechanics, use rapid prototyping. One of the most dominant AM markets for the past decade has been the aerospace industry. This technology is also appealing for the construction of UAVs because of its widespread availability and rapidly growing market for additive manufacturing. By simplifying design and simplifying the production process, additive manufacturing (AM) has transformed not only the realm of UAVs, but also the entire manufacturing arena. In this method, development time and costs can be considerably reduced. AM has acted as a link between digital and physical disruption more than any other technology [110], [111]. Researchers have demonstrated that additive manufacturing can be used to quickly and cost-effectively produce scale aircraft prototypes to determine flight performance through flight tests [112]. Today, 18.2% of the revenue in the AM industry is received from the aerospace industry [52].

Internal components of UAVs are difficult to manufacture using typical manufacturing methods. AM has an advantage over traditional manufacturing in that it can print complex interior structures directly without the need for a mould, thus saving time, cost and effort. G. Goh [110] investigated how additive manufacturing affects UAV aerodynamics, structures, and materials. By using AM techniques, elliptical- shaped wing (elliptical wing offers the lowest induced drag) can be manufactured which is hard to achieve by conventional techniques. He also talked about how additive manufacturing might help UAVs perform better by using smart material actuators and multi-functional constructions. In [113], the extraordinary potentials of FDM printing were revealed. Researchers have shown that high-performance optimized components for the aerospace sector can be built with the right scientific methodology and the help of cutting-edge design tools. S. Junk [114] demonstrated that FDM technology can be used to create robust devices, and that the device can be manufactured rapidly and at a reasonable cost. He also proved that AM method could be used to make wind tunnel models. Rutkay [115] demonstrated the use of additive manufacturing technology to produce propellers by conducting material testing, manufacturing trials, and testing the propellers in a wind tunnel under simulated flying circumstances. His research had clearly proved that, when combined with the customized analysis program, existing 3DP technology can be used to build a flight-ready propeller for a small UAV. Ramirez [48] analyze the aerodynamic improvements obtained in a wing section with a NACA 0018 airfoil manufactured using the fused deposition

modeling (FDM) technique. An improvement in the aerodynamic efficiency of 10% compared with profiles with a smooth surface was gained by using this technology.

A small nozzle is used to extrude a heated thermoplastic filament, such as PLA or ABS, to create 3D objects using the fused deposition modeling (FDM) technique. By generating and following a readable G-code that instructs the numerically controlled printer to enable the printing operation, this additive manufacturing technique forms a part with a certain degree of accuracy from a suitable digital format (e.g., stereolithographic (STL)) that is fused into many layers to obtain a desired thickness [116].

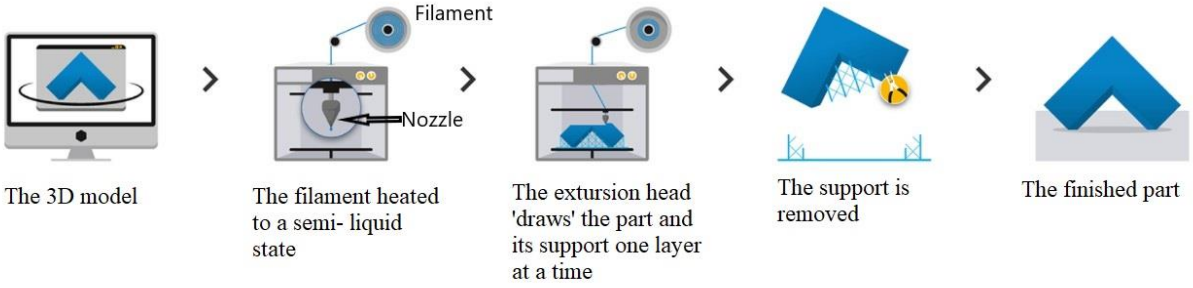

Figure 7- 2: The FDM process [117]

Acrylonitrile butadiene styrene (ABS) and polylactic acid (PLA) filaments are the commonly used materials in the FDM printing process. One must take into account that these polymers have tremendous advantages since they are naturally degradable when disposed in the environment. They are cheap, affordable and efficient in producing specimens that will undergo various tests before manufacturing the real part.

7.2 Tensile test of 3D printed plastic materials

Different sets of material qualification tests were undertaken to assure the safe operation of 3D-printed materials in UAVs. First, the basic static strength of 3D printed polymers such as PLA (Polylactic Acid), ABS (Acrylonitrile Butadiene Styrene), PET-G (Poly-ethylene Terephthalate with a glycol modification) and HIPS (High Impact Poly-styrene) were evaluated using the ISO 527-2 standard [118]. Next, the tensile properties of PLA specimens printed with various layer heights and raster angles, as well as the impact of aging and heat treatment on the tensile properties were investigated. All of the specimens were manufactured using a WANHAO Duplicator i3 and WANHAO Duplicator 6 3D printer, and the 3D printed polymers were tested using a standard ASTM (D638) tensile test procedure [116].

7.2.1 Tensile strength of 3D printed polymers such as PLA, ABS, PET-G and HIPS

Four types of filaments were used in the experimental part for the test specimens, which were PLA (Polylactic Acid), ABS (Acrylonitrile Butadiene Styrene), PET-G (Polyethylene Terephthalate with a glycol modification) and HIPS (High Impact Polystyrene). For the study, 20 specimens were printed with 5 samples of each substance. The sorts of materials used in this work are listed in Table 13 along with the names of the firms who produced them.

Table 14. Characteristics of PLA, ABS, PETG and HIPS Materials delivered by different manufacturers [118]

Material type	Manufacturer	Nozzle temp. [°C]	Bed temp. [°C]
PLA	Wanhao	190-225	50-60
ABS	Wanhao	220-235	80-110
PETG	Devil Design	220-250	70-80
HIPS	Devil Design	230-240	90-100

7.2.1.1 Sample preparation

The specimens used for the test were designed based on the International Organization for Standardization ISO 527-2 standards for determining the tensile properties of molding and extrusion plastics. Figure 7-3 shows the dimensions of such a specimen. As a result, a set of bone-shaped specimens with a thickness of 4 [mm] and an initial spacing between grips of 110 [mm] were constructed.

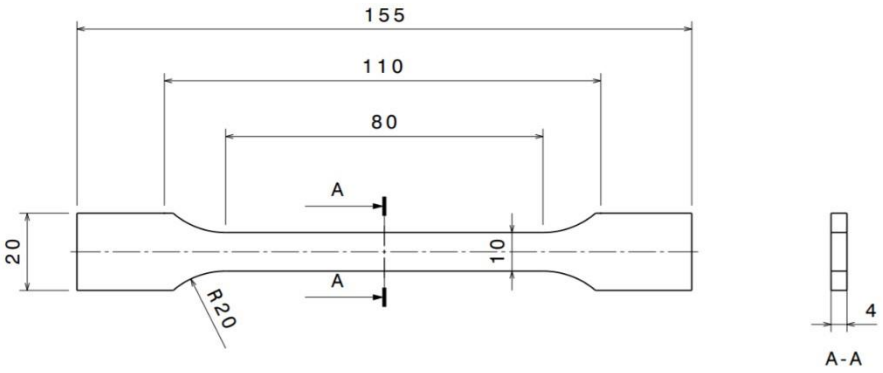

Figure 7- 3: Dimensions of specimen (units are given in [mm]) [118]

All specimens had the same layer height (0.2 [mm], wall thickness (5 [mm], printing speed (60 [mm/s], and infill density (100 %). Only the temperatures of the extrusion and bed differed depending

on the material. The printing parameters needed to create the G-code in Ultimaker Cura are listed in Table 15.

Table 15**.** Printing parameters[118]

Specimen number	Material	Nozzle temperature [°C]	Bed Temperature [C°]	Layer Height [mm]	Density [g/cm^3]
1- 5	PLA	215	60	0.2	1.31
5 -10	ABS	255	80	0.2	1.01
10 -15	PETG	255	80	0.2	1.23
15 -20	HIPS	230	100	0.2	1.05

The Wanhao Duplicator 6 was then used to print the specimens. The printing procedure and the printed samples produced by this printer are depicted in Figure 7-4.

(a)

(b)

Figure 7- 4: 3D printing: (a) printing process; (b) specimens from different materials[118]

7.2.1.2 Experiment

A Shimadzu AGS-X universal testing machine with a capacity of up to 100 kN was used for the tensile test. Using the ISO 527-2 standard, the entire system was calibrated and tested at 1 mm/min speed. Using the recorded data, mechanical characteristics such as Young's Modulus of Elasticity and maximum tensile strength were determined. Figure 7-5 depicts the tensile testing apparatus and its examined specimens.

(a)

(b)

Figure 7- 5: (a) Shimadzu AGS-X series tensile test machine and (b) 3D printed sample after tensile testing [118]

The data were tracked using Trapezium-X software, which was also utilized to create stress- strain graphs. Figure 7-6 depicts the Trapezium software as well as the stress-strain diagram generated by it.

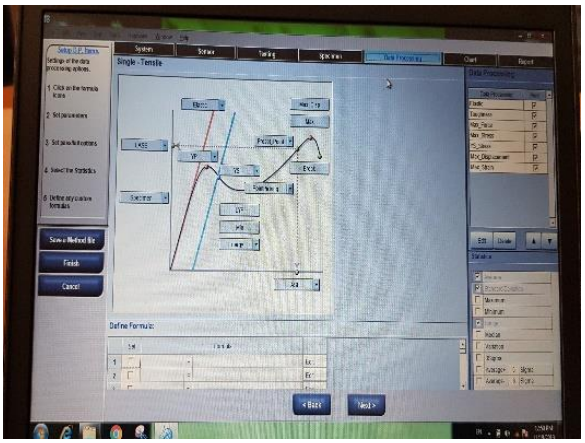

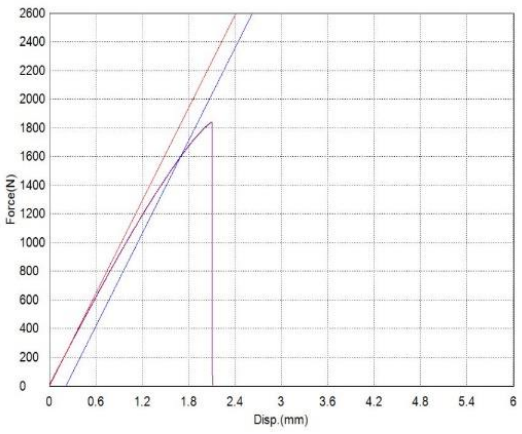

Figure 7- 6: Trapezium-X software and stress-strain diagram obtained from the software [118]

7.2.1.3 Results and discussion

The experiment continued until the specimens were broken. The average tensile strength values derived from measurements are shown in Table 16.

Table 16. Average values of the tensile properties [118]

Specimens	Max Force [N]	Max Stress [MPa]	Max Strain [%]
PLA	1854.75	46.37	2.03
ABS	1329.68	33.24	2.34
PETG	1830.06	45.75	3.30
HIPS	525.98	13.15	1.15

Figure 7-7 shows the tensile test results for four different materials (a). As can be seen from the graph, PLA and PETG have significantly higher tensile strengths than ABS and HIPS. PLA's tensile strength is 1% higher than PETG's at 46.37 [MPa] (45.75 [MPa]). Compared to PLA, the strength of ABS and HIPS is reduced by 22% and 71%, respectively. PLA and ABS also show results that are in line with the reference[119]. Despite its lower maximum stress than other materials, HIPS is frequently utilized in the machining of pre-production prototypes because of its exceptional dimensional stability.

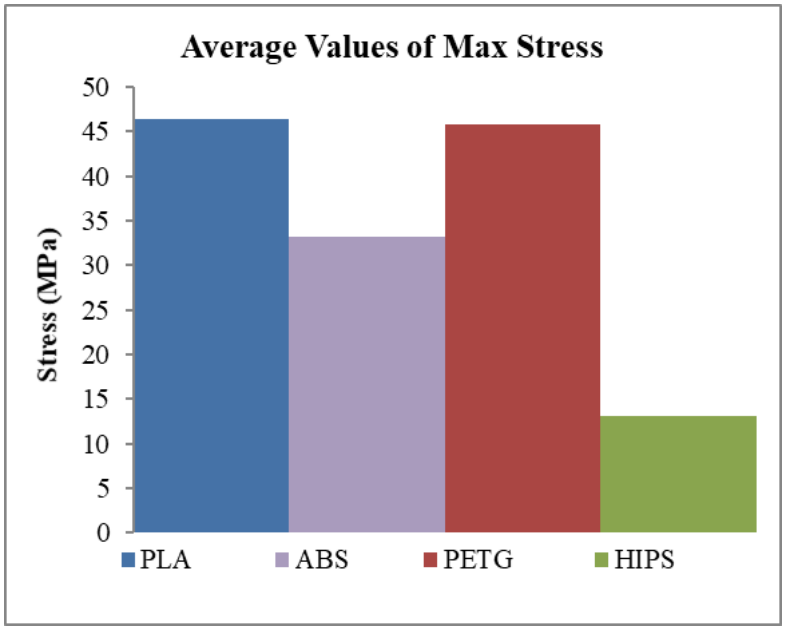

(a)

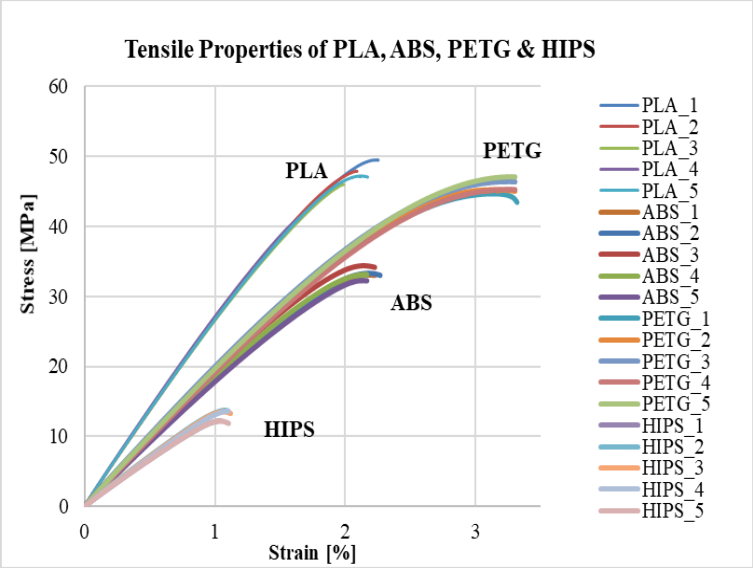

(b)

Figure 7- 7: (a) Average values of the maximum tensile stress for four different materials and (b) averaged stress-strain curves [118]

Figure 7-7 (a) shows the stress-strain curves plotted for several materials using the Trapezium-X software. Figure 7-7 (b) shows that all curves are nearly linear until the maximum stress is reached, at which point the specimens fracture. PETG has the longest elongation at break, while HIPS has the lowest elongation at break.

7.2.2 Impact of Aging Effect and Heat Treatment on the Tensile Properties of PLA

HALE/ HAPS are built to travel around the world for months at a time. As a result, having an understanding of how the materials will react after a particular amount of time is crucial. With this in mind, we investigated how aging and heat treatment affected the tensile characteristics of PLA printed test specimens.

Extrusion temperature, infill density, building orientation, layer height, etc. all affect the tensile properties of 3D printed objects. There was a total of 96 samples, each with a distinct raster angle and a different layer height. The specimens were 175 x 20 x 3 mm in size and the tensile test was performed in accordance with ASTM D638. Six months before the experiment, we printed 36 PLA specimens to examine how they would hold up over time. The first set consisted of 6 specimens with line direction of both shell and infill [0/90]. The second and third sets were made of 6 specimens as well with the line direction of the infill and shell being [-45/45] for the second, and [0/-30/30/-60/60/90] for the third. For the first batch, the layer height was kept at 0.3 mm for all three sets. The second batch included three sets with the same orientations as the first, but with a 0.1mm difference

in layer height. This layer height was taken into account in order to better understand how layer thickness affects mechanical behavior. Similarly, 60 additional specimens were made prior to the experiment, each pair consisting of ten specimens. Half of each set were cured in oven at 57.5 [°C] for 3 hours[116].

7.2.2.1 Sample preparation

The American Society for Testing and Materials (ASTM) D638 standard for tensile testing of polymers was used to print a set of bone-shaped specimens, each with a thickness of 3 [mm] and an initial distance between grips of 106 [mm] [120]. The dimensions of the intended specimen are shown in Figure 7-8

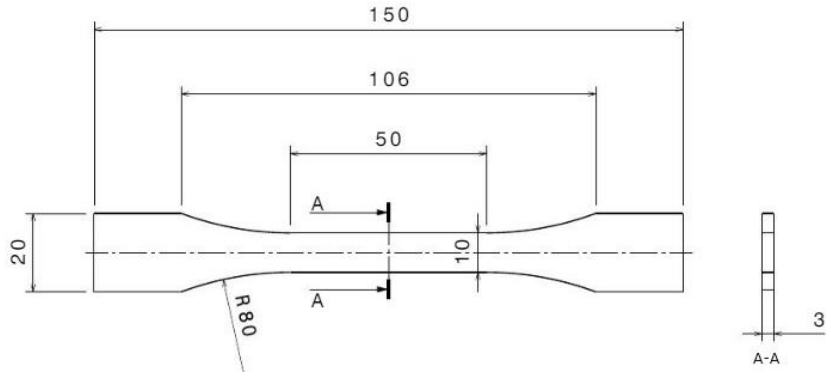

Figure 7- 8: Dimensions of specimens (units are given in [mm]) [116]

For each specimen, the printing parameters were specified to be the same. The first batch's layer thickness was kept at 0.3 [mm], while the second batch's was lowered to 0.1 [mm]. In both batches, the wall thickness was 1.2 [mm], and the top and bottom shell orientations were the same as the infill printing orientation. The key printing parameters evaluated are listed in Table 17. The specimens were printed on a Wanhao duplicator i3 printer, and the average masses were measured using a precise digital scale.

Table 17. Main printing parameters [116]

Specimen number	Layer Height [mm]	Raster angle [°]	Heat treatment [Yes/ No]	Average mass [g]
Aged Samples (36)				
1.1- 1.3	0.1	45/ -45	No	6.67
2.1- 2.3	0.1	0/90		6.67
3.1- 3.3	0.1	0/-30/30/-60/60/90		6.33
4.1- 4.3	0.3	45/ -45		5.66

5.1- 5.3	0.3	0/90		6.33
6.1- 6.3	0.3	0/-30/30/60/-60/90		5.66
7.1- 7.3	0.1	45/ -45	Yes	7.00
8.1- 8.3	0.1	0/90		6.67
9.1- 9.3	0.1	0/-30/30/-60/60/90		7.00
10.1- 10.3	0.3	45/ -45		6.33
11.1- 11.3	0.3	0/90		6.33
12.1- 12.3	0.3	0/-30/30/60/-60/90		6.00
New Samples (60)				
13.1- 13.5	0.1	45/ -45	No	7.40
14.1- 14.5	0.1	0/90		7.00
15.1- 15.5	0.1	0/-30/30/-60/60/90		7.40
16.1- 16.5	0.3	45/ -45		6.60
17.1- 17.5	0.3	0/90		6.80
18.1- 18.5	0.3	0/-30/30/60/-60/90		6.80
19.1- 19.5	0.1	45/ -45	Yes	7.40
20.1- 20.5	0.1	0/90		7.00
21.1- 21.5	0.1	0/-30/30/-60/60/90		7.80
22.1- 22.5	0.3	45/ -45		6.60
23.1- 23.5	0.3	0/90		6.80
24.1- 24.5	0.3	0/-30/30/60/-60/90		7.00

Additional 60 specimens were printed six months after the initial 36 samples were printed to assess the aging effect. For six months, the first 36 samples were stored at room temperature (23.5–27 [˚C])) with a humidity level of 30–50%. After printing, half of the samples from both the old and new sets were immediately placed in an oven and kept at 57.5 [˚C] with a variation of +/- 0.5 [˚C] for around 3 hours. The ambient temperature was 26.50 [˚C], and the atmospheric pressure was 1003 mbar. The oven temperature was measured using a TESTO 735-2 mercury thermometer with a Pt-100 probe as a temperature gauge. The primary purpose of curing some of the samples was to investigate the annealing properties of PLA filament. Following figure shows the oven and thermometer used for the heat treatment.

Figure 7- 9: Oven and thermometer used for the heat treatment [116]

7.2.2.2 Experiment

Tensile tests of aged and new specimens were done using the Shimadzu AGS-X Series universal testing equipment, which has a load capacity of up to 100 kN (7-6 (a)). To achieve accurate results, the entire system was carefully calibrated. To tighten each specimen, non-shift wedge grips were used. During the procedure, the testing speed was adjusted to 5 mm/min in accordance with ASTM D638. During the experiments, the load, displacement, and time were all recorded in real time. Mechanical parameters such as Young's modulus of elasticity and maximum tensile strength were calculated using the recorded data. Figure 7-10 shows the specimens following the tensile test. The Trapezium Lite X software application was used to examine the results, same like in the prior experiment.

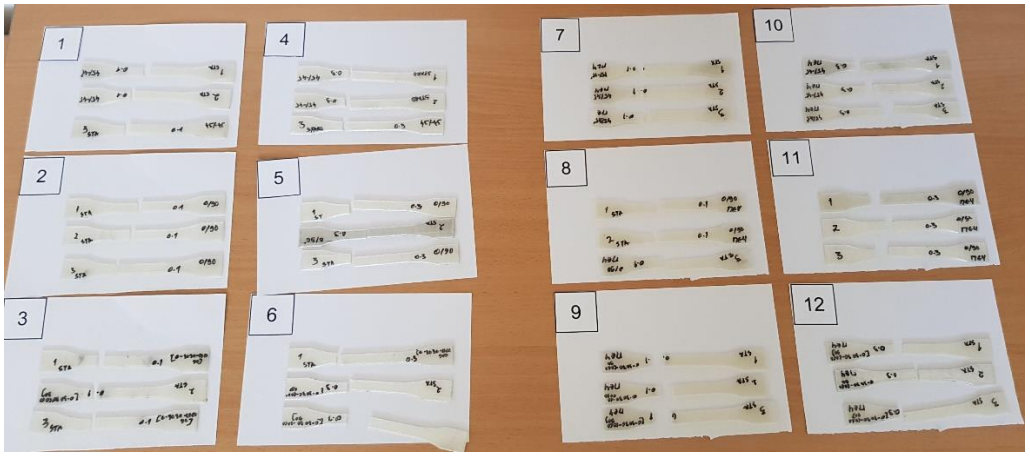

(a) Aged samples (b) Aged samples with heat treatment

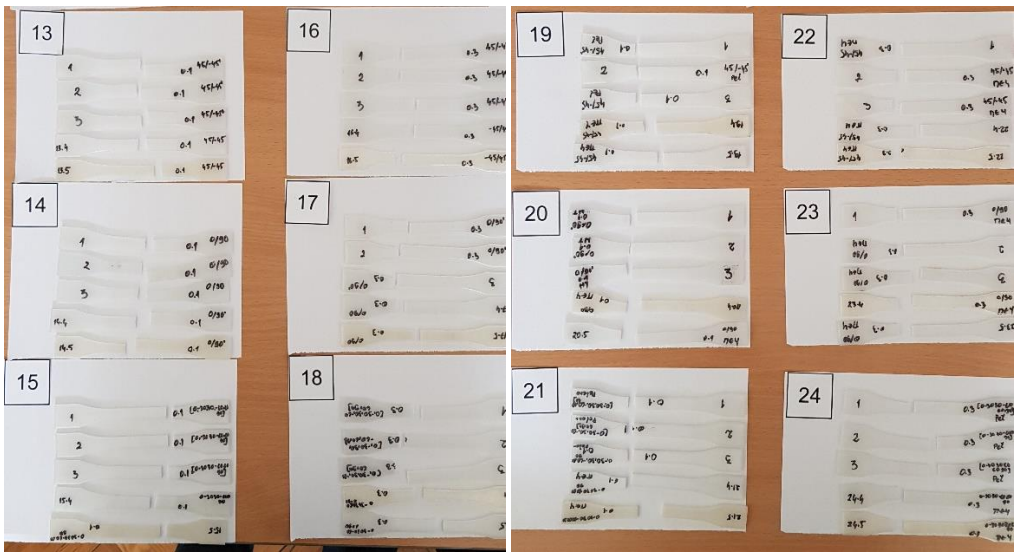

(c) New samples (d) New samples with heat treatment

Figure 7- 10: 3D printed samples after tensile test [116]

7.2.2.3 Results and discussion

Microscopic structure

Any material's microstructure is directly proportional to its strength. As a result, microstructure inspection of the printed surface is essential for understanding irregularities in layer formation quality. On a Motic AE-2000 MET electron microscope, four samples were examined (see figure 7-11). No special preparations were required before testing.

Figure 7- 11: Electron Microscope Motic AE-2000 MET [116]

Inconsistencies in the quality of layer formation were discovered by evaluating the surfaces of the samples. The layer thickness and infill orientation in the first sample were retained at 0.1 [mm] and

+45/-45 [°] respectively. Figure 7-12 depicts the filament movement lines (F) as well as the presence of nozzle furrows (N). A permanent furrow is shown by the red arrows. This shows that the layers in the XY plane did not adhere uniformly, as seen in Figure 7-12. The quick movement of the nozzle has caused damage to the layer line's fabrication. On the other side, the nozzle's high temperature further burns the surface, weakening the polymer's bonds, resulting in a brittle and loose structure. The nozzle was generally in continual contact with the material, and as a result, it was mechanically damaged over time. The existence of some abnormalities in filament cooling following the nozzle passage can be explained as the cause of cracks.

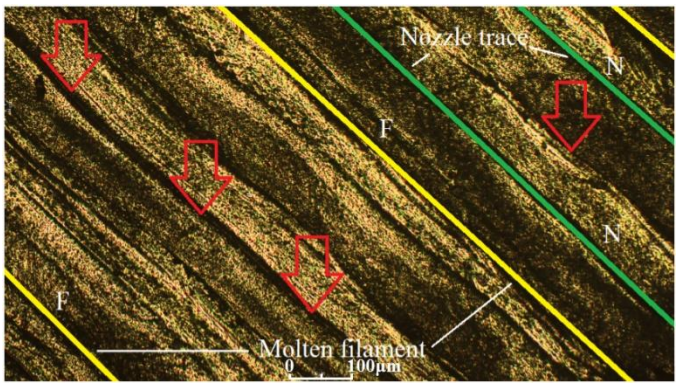

Figure 7- 12 Microscopic view of a specimen (Layer height 0.1 [mm]; Raster angle 45/-45 [°]**)** [116]

The second sample's layer thickness and raster angle were 0.1 [mm] and 0/90 [°] respectively. The abnormality in the printing process is indicated by red arrows in figure 7-13. Due to the high speed printing, the created molten lines were stretched in the upper half of the image. A material accumulation can be seen in the bottom half of the image. The molten thread cooled in an uneven pattern before joining the previous layer. Because the system was not isolated from the environment, uneven material cooling at ambient temperature occurred. Better print quality can be achieved if the PLA is cooled constantly and uniformly.

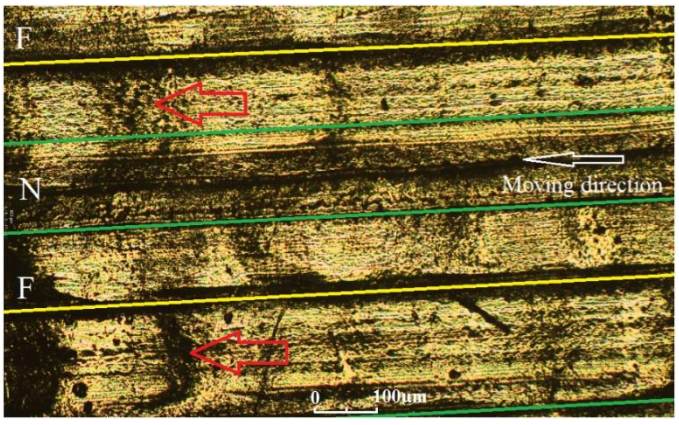

Figure 7- 13: Microscopic view of a specimen (Layer height 0.1 [mm]; Raster angle 0/90 [°]**)** [116]

Tensile properties

As stated previously, 96 samples were generated, 36 of which were six months old and 60 of which were brand new. Half of the samples from the old and new batches were heat treated in an oven. The 96 samples were sorted into six groups or combinations for analysis. To see the effect of heat treatment (HT) on new and aged specimens, different raster angles and layer heights were used to create combinations. The average values and standard deviations (SD) for the maximum force, maximum tensile stress, and maximum displacement of the specimens are shown in the following six tables [116].

Table 18. Average value of the main parameters in Combination 1 (Raster angle 45/-45, Layer Height 0.1 mm) [116]

	Specimens	Max Force [N]	Max Tensile Stress [MPa]	Max Disp. [mm]	Young's Modulus [GPa]
Aged	1.1-1.3	1507.72	50.26	3.685	3.164
Standard Deviation		22.24	0.74	0.435	0.043
Aged with HT	7.1-7.3	1655.01	55.17	3.841	3.318
Standard Deviation		14.37	0.48	0.851	0.055
New	13.1-13.5	1581.71	52.72	3.027	3.416
Standard Deviation		71.98	2.39	0.271	0.033
New with HT	19.1-19.5	1607.85	53.59	3.021	3.300
Standard Deviation		50.07	1.66	0.107	0.046

Table 19 Average value of the main parameters in Combination 2 (Raster angle 0/90, Layer Height 0.1 mm) [116]

	Specimens	Max Force [N]	Max Tensile Stress [MPa]	Max Disp. [mm]	Young's Modulus [GPa]
Aged	2.1-2.3	1439.34	47.97	2.127	3.143
Standard Deviation		8.06	0.26	0.085	0.013
Aged with HT	8.1-8.3	1549.53	51.65	2.258	2.905
Standard Deviation		7.72	0.26	0.052	0.106
New	14.1-14.5	1577.78	52.59	2.308	3.331

Standard Deviation		117.37	3.91	0.116	0.267
New with HT	20.1-20.5	1574.20	52.47	2.370	3.149
Standard Deviation		33.68	1.12	0.129	0.097

Table 20. Average value of the main parameters in Combination 3 (Raster angle 0/30/-30/-60/60/90, Layer Height 0.1) [116]

	Specimens	Max Force [N]	Max Tensile Stress [MPa]	Max Disp. [mm]	Young's Modulus [GPa]
Aged	3.1-3.3	1422.09	47.40	2.874	2.944
Standard Deviation		28.76	0.95	0.282	0.007
Aged with HT	9.1-9.3	1683.84	56.12	2.804	3.337
Standard Deviation		49.35	1.64	0.072	0.077
New	15.1-15.5	1548.91	51.63	2.702	3.327
Standard Deviation		93.24	3.11	0.281	0.269
New with HT	21.1-21.5	1686.34	56.21	2.718	3.430
Standard Deviation		43.20	1.44	0.396	0.156

Table 21. Average value of the main parameters in Combination 4 (Raster angle 45/-45, Layer Height 0.3 mm) [116]

	Specimens	Max Force [N]	Max Tensile Stress [MPa]	Max Disp. [mm]	Young's Modulus [GPa]
Aged	4.1-4.3	1126.08	37.54	2.637	2.586
Standard Deviation		48.07	1.60	0.274	0.037
Aged with HT	10.1-10.3	1157.19	38.57	2.570	2.648
Standard Deviation		113.50	3.78	0.050	0.182
New	16.1-16.4	1428.21	47.61	2.752	3.058
Standard Deviation		23.32	0.78	0.490	0.014
New with HT	22.1-22.4	1478.23	49.27	2.771	2.770
Standard Deviation		44.41	1.48	0.251	0.251

Table 22. Average value of the main parameters in Combination 5 (Raster angle 0/90, Layer Height 0.3 mm) [116]

	Specimens	Max Force [N]	Max Tensile Stress [MPa]	Max Disp. [mm]	Young's Modulus [GPa]
Aged	5.1-5.3	1261.03	42.03	2.138	2.883
Standard Deviation		39.14	1.30	0.02	0.077
Aged with HT	11.1-11.3	1243.23	41.44	2.096	2.842
Standard Deviation		74.65	2.49	0.055	0.160
New	17.1-17.4	1503.26	50.11	2.463	2.46
Standard Deviation		92.25	3.08	0.283	0.147
New with HT	23.1-23.4	1568.94	52.30	2.326	3.252
Standard Deviation		42.97	1.43	0.228	0.065

Table 23. Average value of the main parameters in Combination 6 (Raster angle 0/30/-30/-60/60/90, Layer Height 0.3 mm) [116]

	Specimens	Max Force [N]	Max Tensile Stress [MPa]	Max Disp. [mm]	Young's Modulus [GPa]
Aged	6.1-6.3	1055.97	35.20	2.470	2.456
Standard Deviation		28.04	0.93	0.132	0.064
Aged with HT	12.1-12.3	1053.89	35.13	2.232	2.503
Standard Deviation		16.54	0.55	0.179	0.058
New	18.1-18.4	1528.71	50.95	2.648	3.229
Standard Deviation		87.79	2.92	0.170	0.094
New with HT	24.1-24.4	1619.55	53.98	2.579	3.231
Standard Deviation		14.62	0.49	0.284	0.032

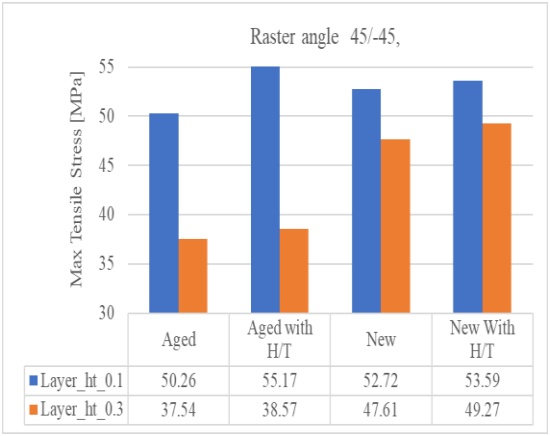

(a) Raster angle 45/-45

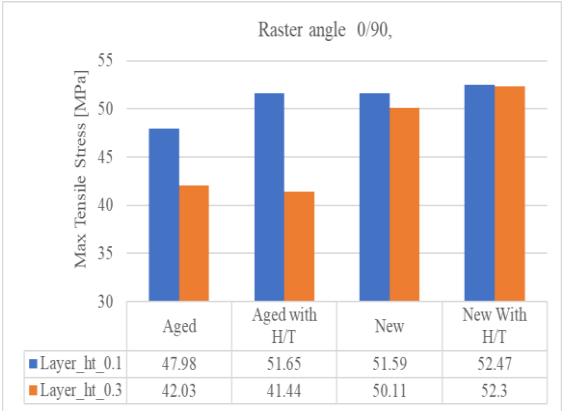

(b) Raster angle 0/90

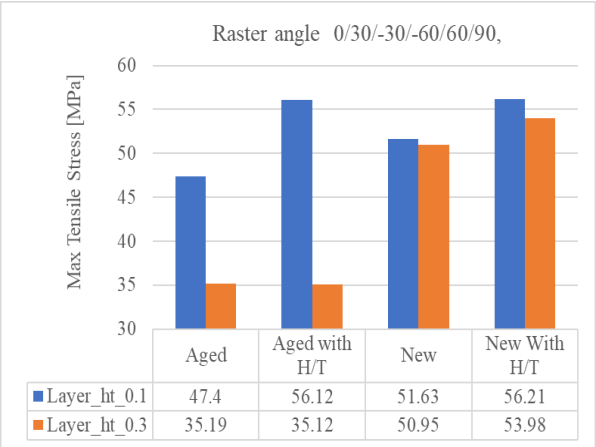

(c) Raster angle 0/30/-30/-60/60/90

Figure 7- 14: Average values of the maximum tensile stress for various raster angle [116]

The mechanical properties of the PLA material often decline with age, as seen in Tables (18-23) and Figure 7-14. The degrading process is clearly more extensive for the specimens printed with a layer thickness of 0.3 [mm]. This is most likely due to the fact that these specimens have a bit larger "air gap," making them more porous and hence more accessible to external influences. The specimens printed with smaller layer heights had higher structural strength, as expected and demonstrated by other researchers [121].

However, it's worth noting that, while heat treatment of the specimens was advantageous in almost every case, it was slightly more successful for the 0.3mm layer specimens. The new specimens' average strength increase was roughly 4% for those printed with 0.1 [mm] and 4.5 percent for those printed with 0.3 [mm]. The heat treatment was also influenced by the printing orientation, with the average increase in strength for the new samples ranging from less than 2% for the 45/-45 combinations (Figure 7-14(a)) to more than 8% for the 0/30/-30/-60/60/90 combinations (Figure 7-14 (c)).

Heat treating the specimens (both old and new) printed with 0.1 [mm] layer height almost completely eliminated aging degradation, with an average strength drop of less than 1% compared to over 7% in the untreated specimens. Surprisingly, heat treatment of the 0.3 [mm] layer specimens accelerated rather than slowed the material degradation. The average reduction in strength for all untreated 0.3mm specimens was roughly 23%, while it was almost 26% for heat treated specimens. It is unclear why is this happening. Perhaps the greater heat exposure made the material more vulnerable to external influences, or the larger "free space" allowed the heat treatment to enhance the observed irregularities. The scientists believe that this phenomenon should be investigated further using PLA filaments from various manufacturers as well as other types of materials (ABS, PET-G etc.). This impact could be

explained by PLA printed components' high variability and inconsistency due to material anisotropy [122], but this is doubtful given that this behavior was found in the majority of specimens.

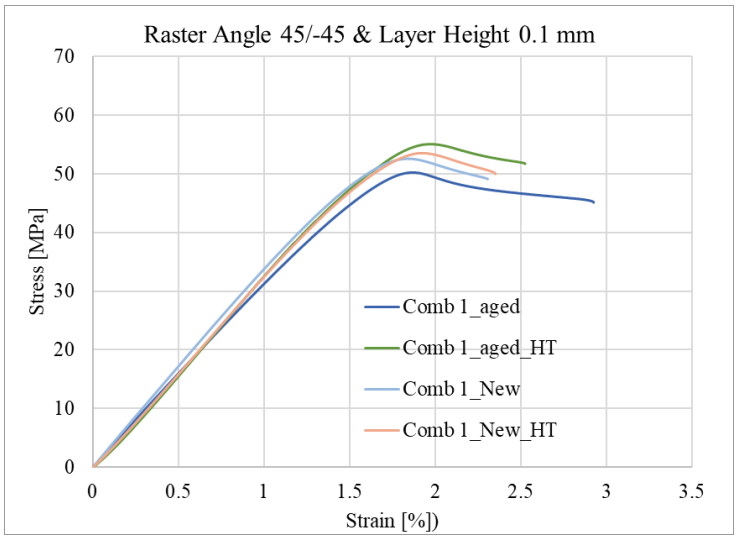

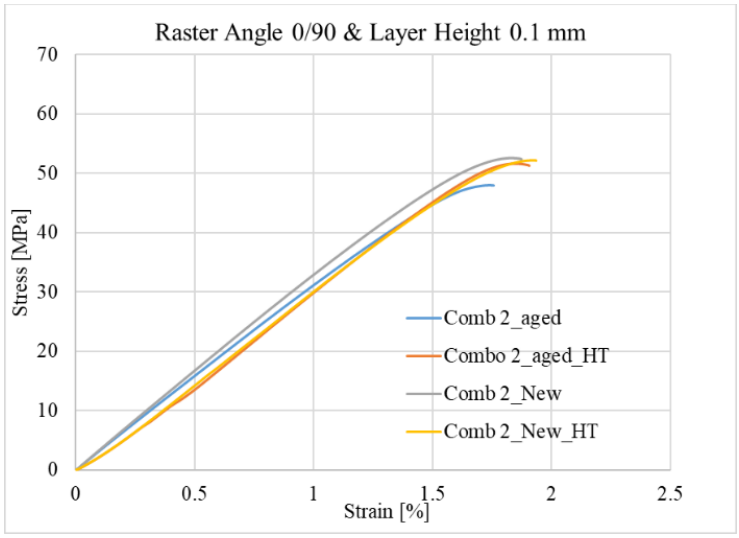

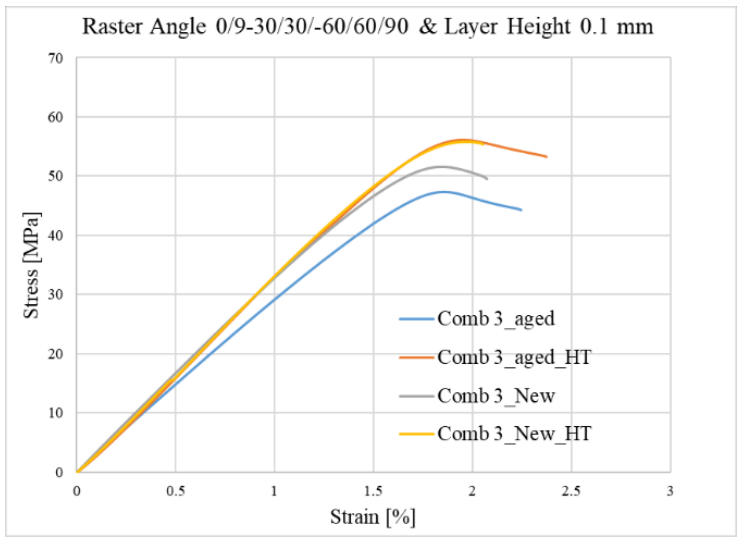

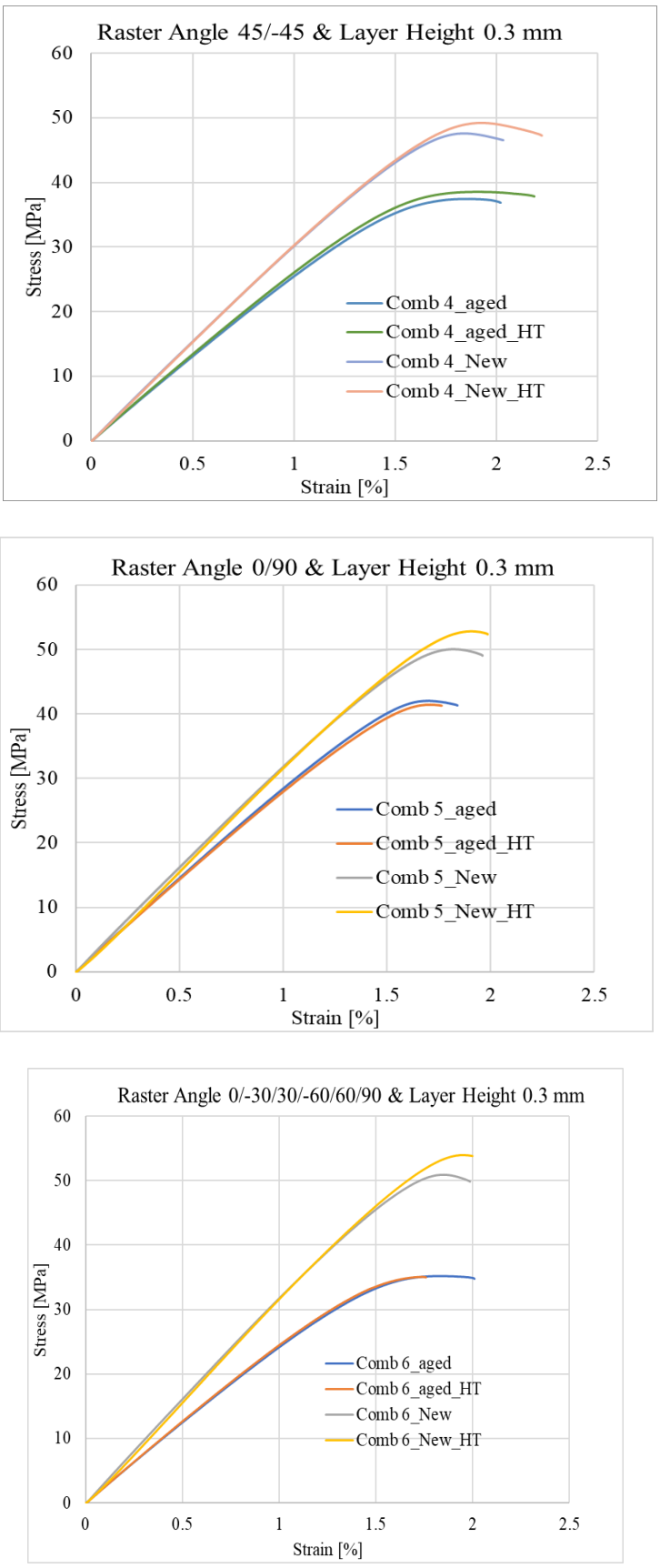

Figure 7- 15: Averaged stress-strain curves [116]

The averaged stress strain curves for all tested combinations are shown in figure 7-15. The influence of printing orientation can be seen from the stress-strain curves as well. It can be noticed that the behavior of the 0/90 [°] printed orientation specimens is almost linear and has the smallest elongation at break hence it is the most brittle of the considered orientations. The 45/-45 [°] orientation has the highest average elongation and the highest plasticity.

7.3 Tensile test of composite materials

Composite materials are advanced materials with excellent mechanical and physical properties, and their use is limited to specialized industries such as aviation and wind energy. However, the use of composite materials in the aviation industry is continuously increasing as these materials are used to construct wing structures and propellers.

The mechanical behaviour of composite plates subjected to tensile force is depicted in this section [123]. Three carbon epoxy composite plates with the exact dimensions but different layer orientations were manufactured and experimentally evaluated according to the D3039 standard process. The tests were carried out with the help of the SHIMADZU AGS-X 100 kN tensile testing machine. The obtained values are then graphically depicted on stress-strain diagrams.

7.3.1 Methodology

The test specimens were subjected to tensile load after being generated, which included selecting a carbon-epoxy composition with various layer orientations and determining their dimensions in accordance with the given standard. The results were then processed and analyzed.

7.3.1.1 Sample making

In this experiment, the tested plates are laminates of carbon-epoxy composition, where 8 layers are differently oriented (stacking of laminates at different angles) for each of the 3 types of plates. The laminate is a unidirectional fabric, carbon marked CU 300-0 /SO, with 300 g/m^2 fabric, fiber content marked HTS40-12k 800tex, 0.3 mm thick per layer and epoxy resin "Hexion Specialty Chemicals Stuttgart" marked L285 with hardener H287. The characteristics of carbon fiber composition provided by carbon fiber and laminate producers are shown in Table 24.

Table 24: The characteristics of carbon fiber composition provided by carbon fiber and laminate producers [123]

Material type	Weave/orientation	Areal weight (dry) [g/m²]	Resin type	Resin mass content [%]
Unidirectional prepregs				
C U200-0/NF-E310/30%	unidirectional	200	epoxy	30
C U255-0/NF-E322/37%	unidirectional	255	epoxy	37
C U300-0/NF-E420/38%	unidirectional	300	snap-cure epoxy	38
C U100-0/SO-E501/40%	unidirectional	100	epoxy	40
C U150-0/SO-P360/43%	unidirectional	150	phenolic	43
C U450-0/SD-E501/36%	unidirectional	450	epoxy	36
C U600-0/SD-E501/33%	unidirectional	600	epoxy	33

Woven fabric prepregs				
C W95-PL1/1-E323/48%	plain	95	epoxy	48
C W160-PL1/1-E323/50%	plain	160	epoxy	50
C W200-TW2/2-E311/48%	twill 2/2	200	epoxy	48
C W200-TW2/2-E501/48%	twill 2/2	200	epoxy	48
C W200-PL1/1-E323/42%	plain	200	epoxy	42
C W200-TW2/2-E420/40%	twill 2/2	200	snap-cure epoxy	40
C W245-TW2/2-E503/44%	twill 2/2	245	epoxy	44
C W245-TW2/2-E323/45%	twill 2/2	245	epoxy	45
C W245-TW2/2/SQ-E450/43%	twill 2/2	245	transparent epoxy	43
C W305-PL1/1-E331/41%	plain	305	epoxy	41
C W410-TW2/2-E501/42%	twill 2/2	410	epoxy	42
C W665-TW2/2-E323/40%	twill 2/2	665	epoxy	40
Multiaxial fabric prepregs				
C B160-45/SO-E501/47%	biaxial	160	epoxy	47
C B450-45/SO-E501/38%	biaxial	450	epoxy	38
C B300-45/ST-E331/42%	biaxial	300	epoxy	42
C B610-45/ST-E320/40%	biaxial	610	epoxy	40
Non-woven prepregs				
C N450-IS/NF-E501/65%	isotropic	450	epoxy	65
C N450-IS/NF-E420/65%	isotropic	450	snap-cure epoxy	65

All tested specimens met the requirements of standard D3039 [124] for testing static properties under tensile load, with dimensions of (250* 25* 2) mm. Table 24 shows orientation of laminates.

Table 25. Different laminates and their directions [123]

Samples	Laminates	Orientation
Plate 1	Anti-symmetric	(+45°/-45°/+45°/-45°/ +45°/-45°/+45°/-45°)
Plate 2	Quasi-Isotropic	(90°/+45°/-45°/0°/ 0°/-45°/+45°/90°)
Plate 3	Balanced	(90°/+45°/-45°/0°/ 90°/+45°/-45°/0°)

7.3.1.2 Tension and behavior of composite materials

Composites' physical and mechanical properties directly depend on the properties, geometry, and concentration of constituent materials. When it comes to the analysis of properties and behaviour under the action of load, the experiment of composites begins with establishing basic connections and relations between stresses and strains, as in the case of homogeneous isotropic materials. It is assumed that isotropic, homogeneous materials are uniform throughout their volume and have the same elastic properties in all directions. Under the action of tensile force, the material is deformed, as in figure 7-16.

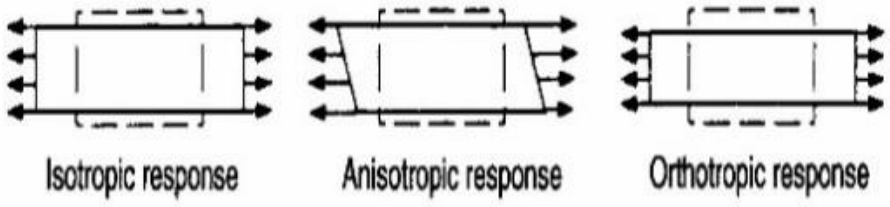

Figure 7- 16: Behavior of isotropic, anisotropic and orthotropic materials under the tensile force

Unlike conventional materials, composites are inhomogeneous and do not behave like isotropic materials. The properties of anisotropic materials are different in different directions. During the action of the tensile load, deformation occurs as a combination of elongation and deformation caused by shear. Due to the different degrees of anisotropic behavior, the actual deformation directly depends on the properties of the material being tested. Deformations in the transverse directions, unlike isotropic materials, are not the same due to the different values of the Poisson's ratio in the observed directions, i.e. the sample will deform more in one of the observed directions under the action of the load. When the matrix and fibers are incorporated and thus form a composite material, they retain their properties and characteristics that directly affect the properties of the composite. The material created in this manner will be made up of layers and laminates with the desired properties in one or more directions.

7.3.1.3 Experimental Setup

The test procedure were discussed in papers [125]–[128], which described the experiment and the determination of the mechanical properties of polymers and some composite structures, as well as the occurrence of delamination due to fracture, and served as a reference in the analysis of the obtained results.

Three test segments were included in the experiment. Nine composite plates (three samples for each segment type) of the same dimensions were prepared for testing (in accordance with the standard, three samples were made in order to repeat the experiment and validate the results).

Figure 7- 17: Test sample prepared for testing in Shimazu tensile testing machine [123]

7.3.2 Results and discussion

After performing all the experiments, the obtained results were processed and analyzed. Figure 7-18 shows the test samples after the experiment, where it can be noticed that all plates look different, i.e. that the behaviour of composite structures depends on the process of making and orientation of layers.

Figure 7- 18: Composite plates after the experiment [123]

Before performing each experiment, it was necessary to calibrate the entire system to obtain valid results. Each specimen was tightened with hydraulic grips/jaws. The machine was equipped with a standard load cell and a device for recording displacement. During the sample mounting phase, the maximum load was controlled. According to ASTM D3039, the samples were exposed to a monotonic tensile load at a rate of 2 mm/min. Figure 7-19 shows the experimental setup of the study.

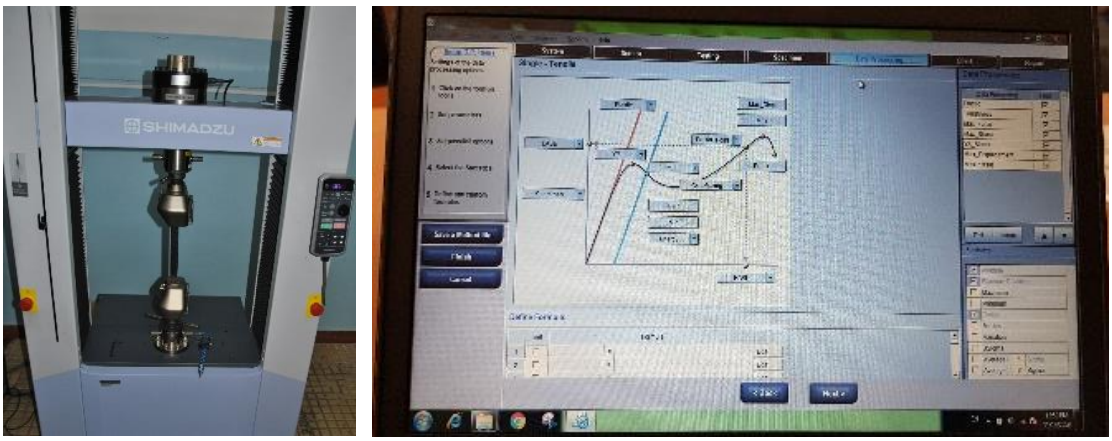

Figure 7- 19: Experimental set-up (tensile testing machine, test sample and data processing and analysis system [123]

The first segment of the test - plate 1 (+45°/−45°/+45°/−45°/+45°/−45/+45°/−45°)

The first block of specimens was made by staking the laminates at 45° angles, and after the tensile test cracking and spreading of the fracture occurred in the layering direction. Two out of three samples behaved similarly, and there was a rupture at approximate load values of about 3.5 kN.

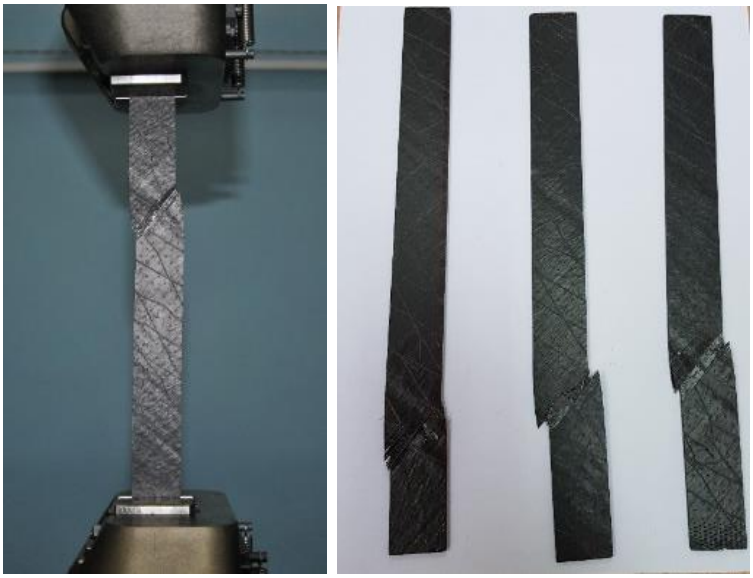

Figure 7- 20: Sample type 1 and their facture positions [123]

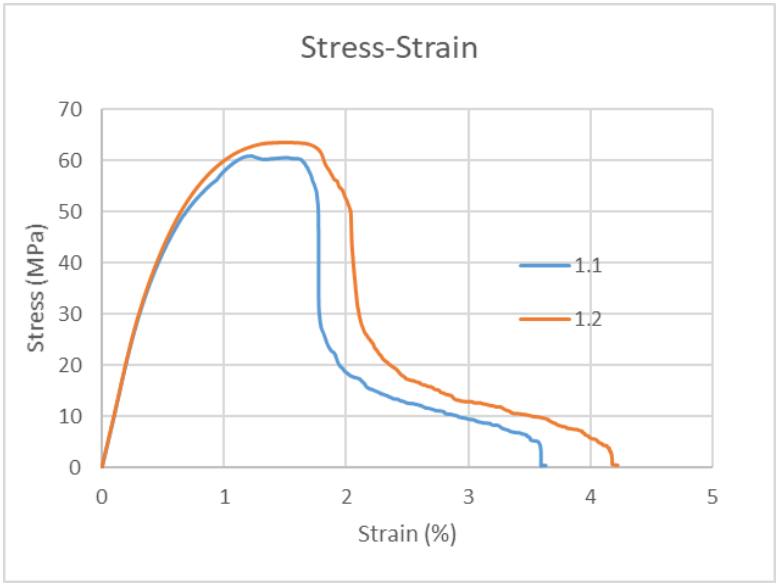

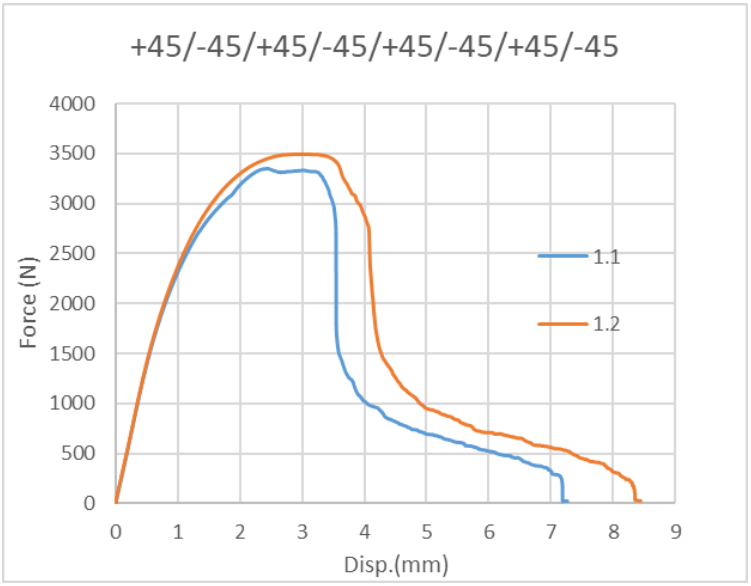

Figure 7- 21 Stress-strain diagram of sample type 1 [123]

Figure 7-21 illustrates the stress-strain curves for the two tested samples. The first sample results are not displayed as the specimen tore shortly after the experiment began and at a very low force, most likely due to material inconsistencies and manufacturing and production problems, which would question the validity of the testing procedure used. The value of tensile strength is around 60 MPa.

The second segment of the test - plate 2 (90°/+45°/−45°/0°/0°/−45°/+45°/90°)

Unlike the previous segment, these three samples were distinct from one another. The first and third were identical, but the second had a difference in both applied force and tearing. The strips and the last layer were removed (peeled) after exposure to the load in the first and third samples and cracking occurred at a lower force (approximately 13 kN). In contrast, the second tube required a substantially greater force (about 24 kN), and the plate corresponds to a horizontal fracture shape (figure 7-22).

Figure 7- 22: All samples from segment 2 after tensile test [123]

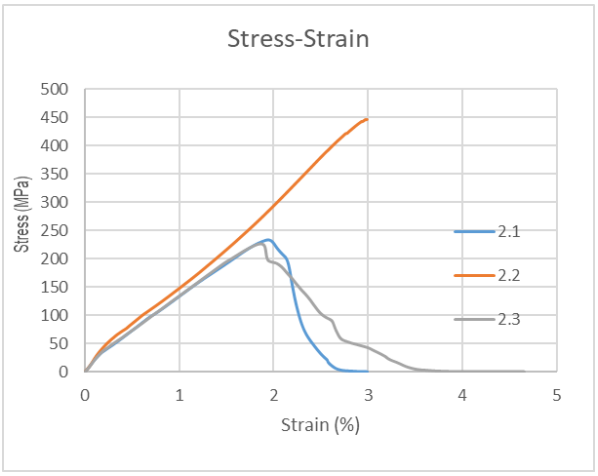

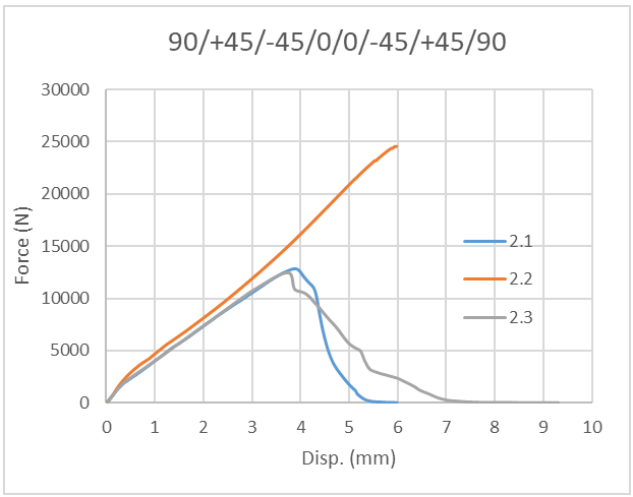

Figure 7- 23: Stress- strain diagram of samples from segment 2 [123]

Figure 7-23 shows the stress-strain curves of three samples of plate type 2, where the similar behavior and the shape of the curves for the first and the third, while the curve of the second differs in shape and significantly higher value of the load at which the fracture occurred.

The third segment of the test - plate 3 (90°/+45°/−45°/0°/90°/+45°/−45°/0)

In the last segment of the test, the rupture occurred at high load values (about 25 kN), and the test period lasted the longest. Figure 7-24 depicts a complete separation of fibers and layers, as well as the development of delamination. Similarly, to the preceding segment, the removal and cracking of the 90-degree layer came first, followed by stratification of the entire structure (Figure 7-24).

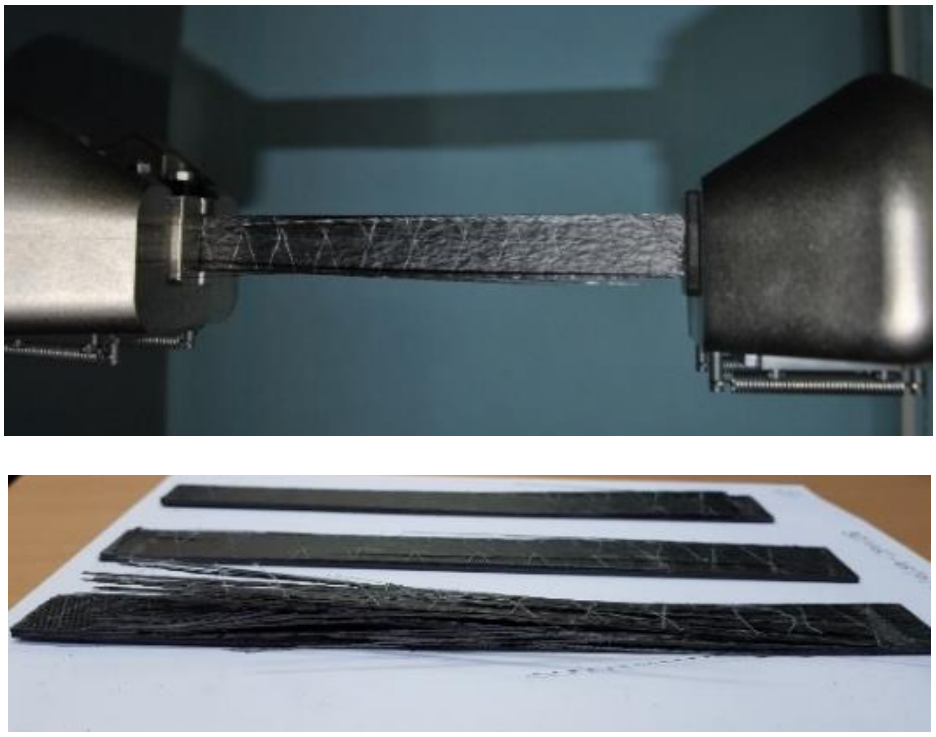

Figure 7- 24: Samples after tensile test [123]

It can be seen from Figure 7-25 that the tensile curves of all three samples were similar and that large values of the forces that led to the rupture were required.

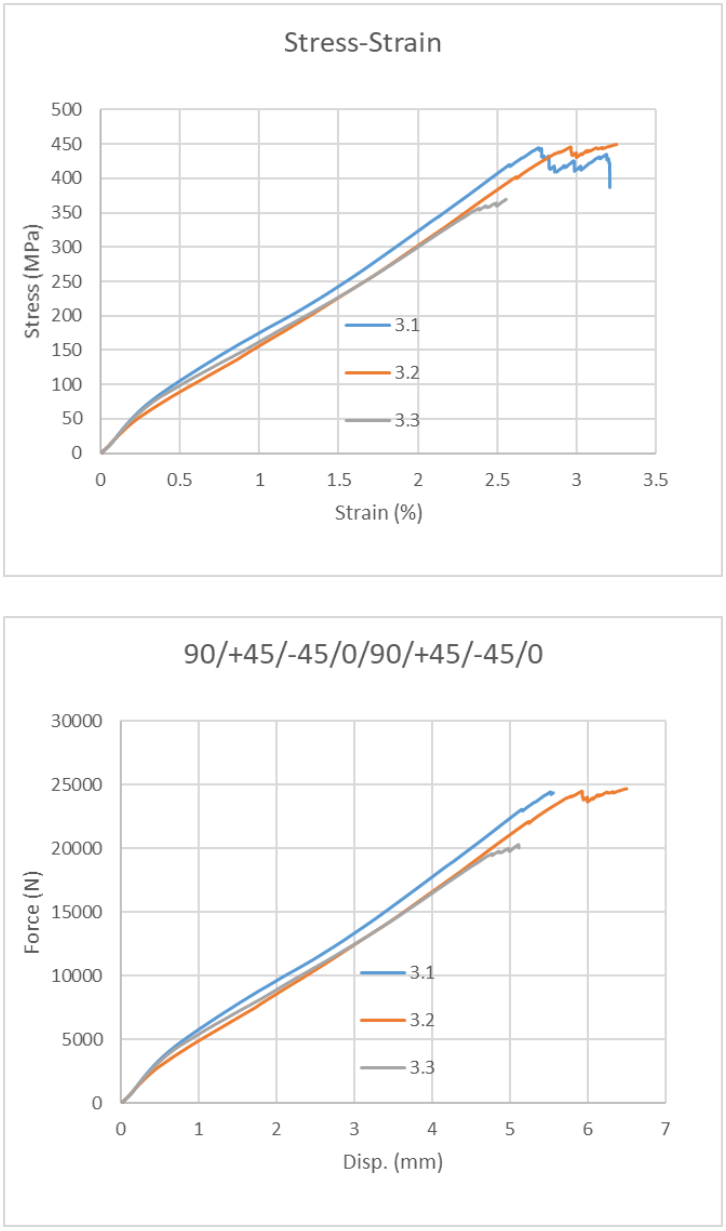

Figure 7- 25: Stress- strain diagram of samples from segment 3 [123]

Despite slight differences induced by material dislocations during production and in the manufacturing process, the study demonstrates that the tested samples' fracture morphologies are consistent with ASTM D3039 [124]and meet the procedure's requirements:

1) the first segment corresponds to the GAT failure mode – G (Failure type- Grip/ tab), A (Failure area- At grip/ tab), B (Failure location- Bottom), i.e the appearance of a fracture at an angle on the upper half of the sample.

2) second segment: the first and third cases correspond to LIT-Lateral Inside grip/ tab Top, i.e. shooting in the part inside the machine grip and the second sample corresponds to the LGM criterion- Lateral Grip Middle, ie the appearance of a fracture in the middle and lower half laterally.

3) the third segment corresponds to the DGM criterion - Delamination Gage Middle, i.e the occurrence of delamination of the entire structure.

After gathering and presenting the data, a conclusion about the behavior of composite plates subjected to tensile load can be reached. Despite the fact that all plates have the same composition and size, there is a significant variance in the mechanical characteristics of all three types of plates, i.e. how different layer stacking and orientation affect sample behavior. The tensile curves in the diagrams of type 2 and 3 plates are similar in shape, but the load necessary for the fracture to occur differs significantly. The variation in the second sample from series 2 was most likely related to possible manufacturing errors (appearance of gaps during lamination, insufficient share of fibers in the fabric, shorter drying period, etc.). Furthermore, in all situations where the outer layers were positioned at a 90-degree angle, cracking and peeling happened quickly across the whole surface of the lamina, implying that such a method of arranging the orientation of surface layers should be avoided during the manufacturing process.

After obtaining and presenting the results, a conclusion can be drawn about the behavior of composite plates exposed to tensile loads. On the behavior of the samples type 2 and 3, diagrams are similar in the shape of the tensile curves, but there is a large difference in the load required for fracture. The deviation in the second sample from type 2 gap during lamination, insufficient proportion of fibers in the fabric, shorter drying period, etc.) Also, in all cases where the outer layers were placed at an angle of 90 °, cracking and peeling quickly occurred over the entire surface of the laminate, from which can be concluded that during the manufacturing process such a way of laying, the orientation of the surface layers, should be avoided. Table 26 and figure 7-26 show the values of the modulus of elasticity and tensile strength of all plates.

Table 26: Modulus of elasticity and tensile strength of all plates

Samples	Modulus of elasticity [Force200-1600 (N)] (GPa)	Tensile strength (MPa)
Plate 1.1	10.0446	60.923
Plate 1.2	10.1572	63.5682
Plate 2.1	20.8157	233.465
Plate 2.2	24.6718	446.6
Plate 2.3	21.1954	226.467
Plate 3.1	26.0574	444.451
Plate 3.2	24.0525	449.226
Plate 3.3	25.6341	369.379

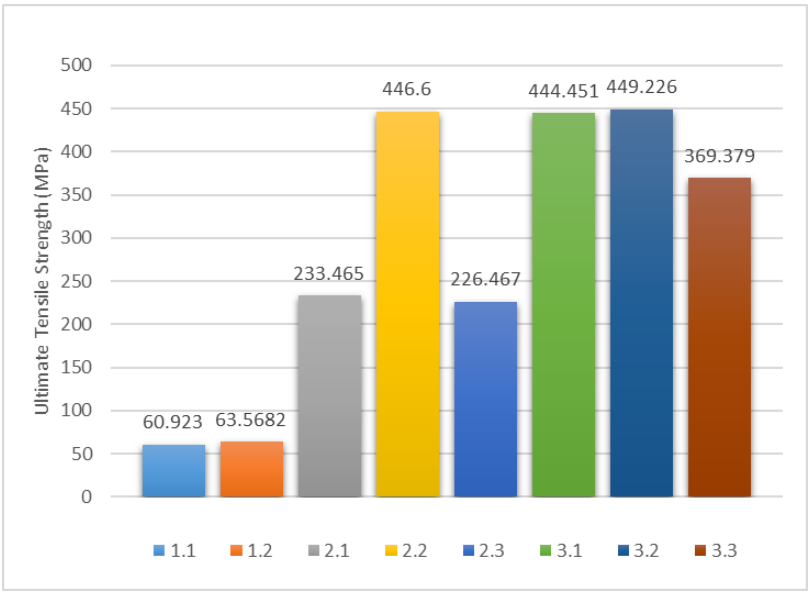

Figure 7- 26: Modulus of elastic and tensile strength of plates from different segments [123]

7.4 Wing structure and its components

Shear forces and moments caused by lift and drag are reacted by the wing structure. They nearly always result in three mutually orthogonal forces (lift, drag, and an inboard force if the wing has dihedral), as well as three mutually orthogonal moments (bending moment, drag moment, and wing torsion). The basic configuration of the main wing of solar-powered airplanes includes the main spar, wing ribs, skin, and solar panels.

7.4.1 Main Spar

The principal load path in the wing is the main spar, which is designed to react to wing bending and shear stresses. The force and moments generated by the spanwise lift distribution are carried by spars, which are strong beams that run spanwise in the wing. The positioning of the main spar (1st spar) in the wing should be, ideally, where torsional moments are minimum [43]. Torsion deforms the cross-section of the spar (beam), decreasing its area moment of inertia (I) and consequently diminishing its effectiveness to resist bending loads [37], [99], [106].

7.4.2 Ribs

The ribs help the wing maintain its airfoil shape, and they form tubes and boxes with the skin and spars to prevent wing twisting and torsion. One of the roles of the ribs is to preserve the shape of the cross-section, which is dictated by aerodynamic principles and must be maintained for all load combinations. They also act with the skin in resisting the distributed aerodynamic pressure loads; they distribute concentrated loads (e.g., undercarriage and additional wing store loads) into the structure and redistribute stress around discontinuities. The spanwise position of the ribs in the wing and the weights they must support determine the dimensions of the ribs. Ribs serve largely as formers for the airfoil shape at the wing's outer sections, where the cross-section may be minimal if the wing is tapered and the loads are light. For this purpose, a light structure is acceptable; but, closer to the wing root, where the ribs must absorb and transmit significant concentrated applied loads, such as those from the undercarriage, engine thrust, and fuselage attachment point reactions, a much more robust structure is required.

7.4.3 Skin

The primary purpose of the wing skin is to provide an impermeable surface for sustaining the aerodynamic pressure distribution that determines the wing's lifting capability. The lower and upper surfaces of the HAPS main wing are usually skinned with Mylar, which resembles a high-tech cling film. This high-tech film is thin like an A4 paper which help to reduce the weight of the wing [129].

7.4.4 Solar cells

The solar cells are then attached to the upper wing surface, covering the Mylar. Flexible solar cells with a low mass density are preferred to increase a plane's efficiency and meet energy demands. Figure 7-28 depicts a typical structure of solar-powered wing.

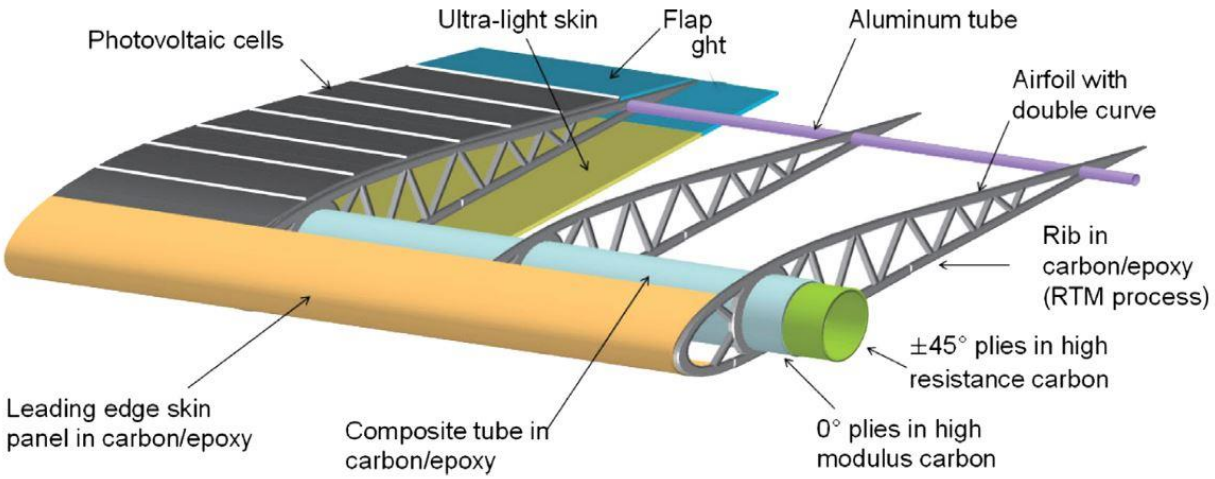

Figure 7- 27: A typical wing structure configuration [130]

8 Wing structural analysis

The design and manufacture of aircraft wings generally require the consideration of several distinct structural requirements. The two primary functional needs to consider when selecting materials for constructing an aircraft wing are high strength and lightweight. The structural behaviour is determined by the used material and its distribution along the wing. Two wing models with ribs, spars, and skins (upper and lower) were initially designed using the CAD program Catia. Then, the structural analysis by 1-way fluid-structure interaction (FSI) approach was used to examine these wing models in Ansys.

8.1 Fluid- Structure Interaction

The shape of a high aspect ratio wing may experience significant deformation due to the wing's coupled aerodynamic, gravitational and inertial loads as well as other sudden effects such as manoeuvres, gusts, atmospheric turbulence, etc. The Fluid-Structure Interaction (FSI) is when fluid and structural analyses are combined. It considers the resulting pressure or temperature fields of a CFD analysis and the direct consequences of this load on the structural analysis. When fluid flow exerts forces on a solid structure, the structure deforms, potentially disrupting the initial fluid flow. For example, during flight, this type of interaction generates the deformation of an airplane wing [89][53][54].

FSI simulation can be divided into two types depending on the complexity of the fluid and solid models and their physical interaction. When the physical coupling between the fluid and solid models is steady and largely from one model to the other, a one-way coupling approach (for example, data transfer) is appropriate and was employed here in the preliminary design phase. When the physical coupling between the fluid and solid models requires significant feedback from one model to the other, a two-way coupling approach is necessary. For example, a two-way FSI analysis approach is necessary to simulate the potentially transient deformation of an airplane wing as air flows around it. For the rapid and correct solution of large and physically complex FSI problems involving highly deformable bodies, thin membranes, unsteady loads, tight integration of sophisticated fluid and structural analytic methods is necessary [131].

The FSI analysis has been widely employed in the aerospace industry. For example, L. Zhang [55] discussed the impact of temperature and pressure in the flow field on the natural properties of various aircraft wing materials. The flow field of the wing structure was simulated at various Mach numbers, and the one-way FSI method in ANSYS-Workbench was used to quantify the stress generated by pressure and temperature. S. Son [56] used the loose coupling or one-way FSI analysis and Kriging

method to find the optimized shape of a high-aspect ratio wing. Z. Qu [57] analyzed the aeroelastic response of a high-altitude propeller by using the loose coupled or 1-way FSI method.

8.2 Detailed wing design

There are many different types of wings, including the conventional wing, delta wing, swept wings, dihedral wings, tapered wings, and flexible geometry wings. Each wing produces different aerodynamic characteristics, stability, and maneuverability. The first wing or wing 1 (one segmented/ conventional) was created using the S1210 airfoil geometry, while the second wing or wing 2 (two-segmented) was designed utilizing an optimization technique. Both of these airfoils' selection procedures are covered in Chapter 5.

8.2.1 Design of wing 1

To begin, the point coordinates of airfoil S 1210 were exported to Catia from the airfoil tools and UIUC airfoil Coordinates Database. Spars are located at 0.25*c* and 0.65*c* from the leading edge of the wing (Chord length = *c*). Spars position was chosen to accommodate the maximum torsional stiffness according to the design practice in the wing structural design. The distance between the ribs is around 720 [mm]. Wingspan, b = 33.01 [m]; Taper ratio = 1; Chord, c = 1.50 [m] are the basic dimensions of the wing. Figure 8-1 depicts the detailed wing model designed in Catia.

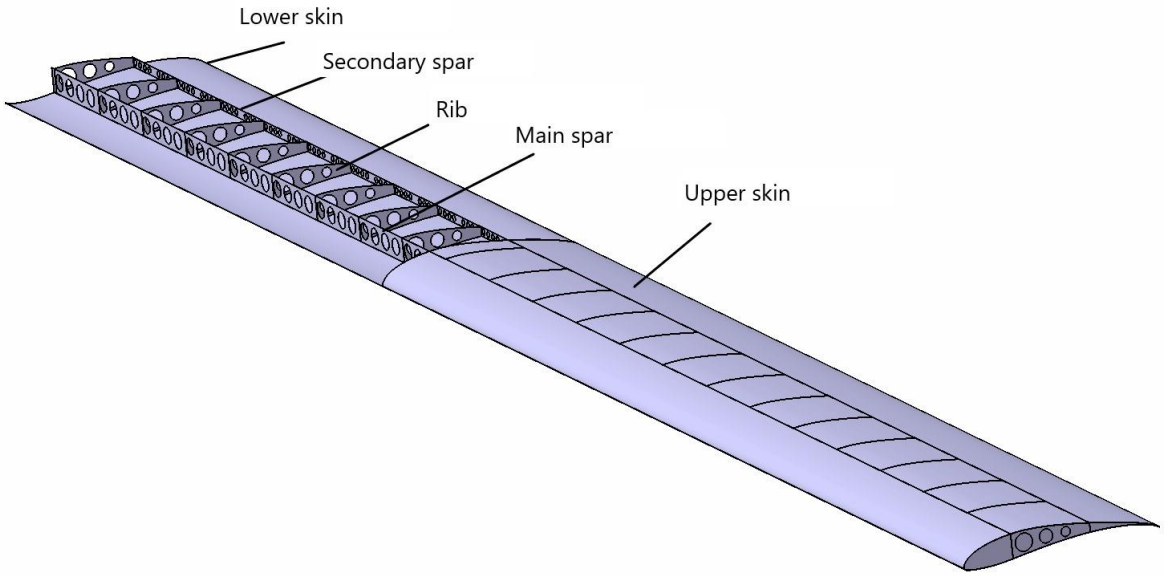

Figure 8- 1: One- segmented rectangular wing structure

8.2.2 Design of wing 2

The structure of a two-segmented wing differs from that of a single-segmented wing. Instead of using flat rectangular spars, two cylindrical tubes are used in wing structure two, but the spacing between spars from the leading edge is identical to wing 1. Because it possesses excellent bending and torsional stiffness, cylindrical tubes are commonly used to construct solar-powered HALE aircraft wings and modern UAVs. The main spar has a diameter of 120 mm in the first section and 70 mm in the second, while the secondary spar has a diameter of 60 mm in the first section and 35 mm in the second. All 24 ribs are designed with an airfoil from the optimization process, and the spacing between them is around 700 [mm]. An extra rib is added here to increase the stiffness between the connection of two wing sections. Figure 8-2 shows a detailed structure of wing 2.

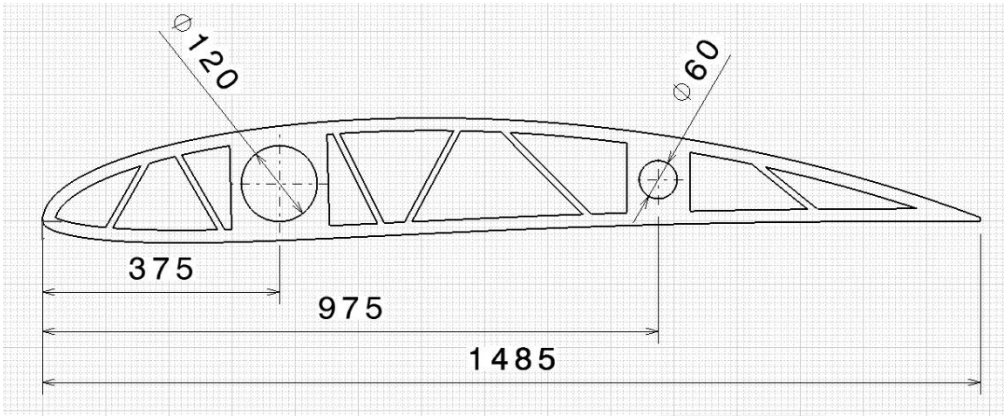

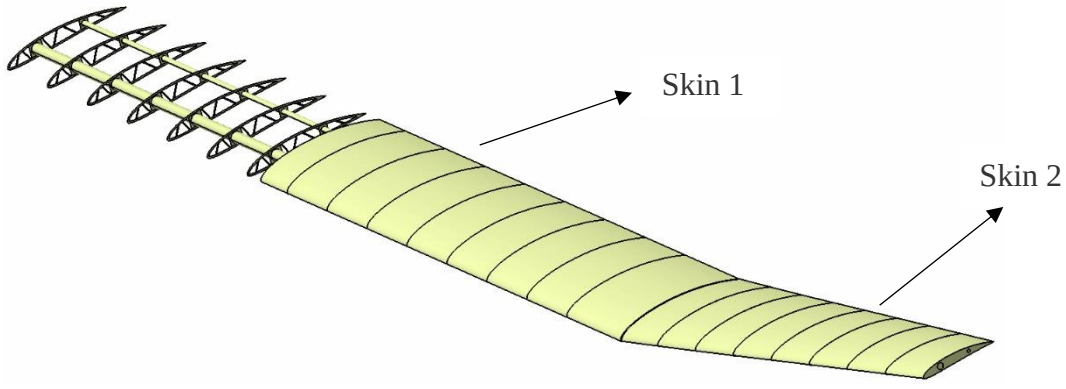

Figure 8- 2: Detailed structure of wing 2

8.3 1- way Fluid-Structure Interaction analysis

This section involves the solid mechanic's aspects of both wings. The pressure loads calculated using Fluent in Chapter 6 are imported in Mechanical and the stresses and deformations on the wings are subsequently determined. The static 1-way FSI analysis of the wing structure is performed by finite element method in ANSYS Structural. Uni-directional Epoxy Carbon, PLA and Mylar (PET) are chosen for the coupled simulation in this study as the wing materials to analyze the stress. The default values of material properties of uni-directional epoxy carbon available in ANSYS Workbench are used, while the materials characteristics of PLA are obtained experimentally, as demonstrated in Chapter 7. This is an initial, simplified structural analysis. Uni-directional carbon is considered isotropic material instead of orthotropic (the assumption is suitable because the wing is primarily loaded along the main direction). Table 27 lists all three materials and their properties.

Table 27**.** Properties of the materials used in wing structure

Material	Young's modulus [Pa]	Poisson's ratio	Density [kg/m^3]
Epoxy Carbon UD	2.09E+11	0.33	1540
PLA	2.2E+09	0.33	1300
Mylar (PET)	2.8E+09	0.33	1370

The choice of element type and the level of refinement of the element mesh are the most important factors to consider when establishing an accurate finite element model. The accuracy of the analysis depends mainly on the number of elements and the quality of the mesh. A large number of elements and fine mesh will give more accurate results. However, at the same time, hardware computation takes more time and more computing resources are needed. An analysis of the mesh convergence of the finite element model is required to satisfy the accuracy of the simulation results. The default mesh setting was first employed, which produced roughly 50000 elements but was regarded to be of moderate mesh quality. The mesh was refined by setting the size function to proximity and curvature, the relevance centre to medium, and the maximum face size to around 1 m and the minimum face size is 16 mm. Other settings such as smoothness and transition were set to medium and fast, respectively. Figure 8-3 shows how the assumed geometries of wing skins, spars, and ribs are discretised into roughly 180000 plate-type elements in Ansys.

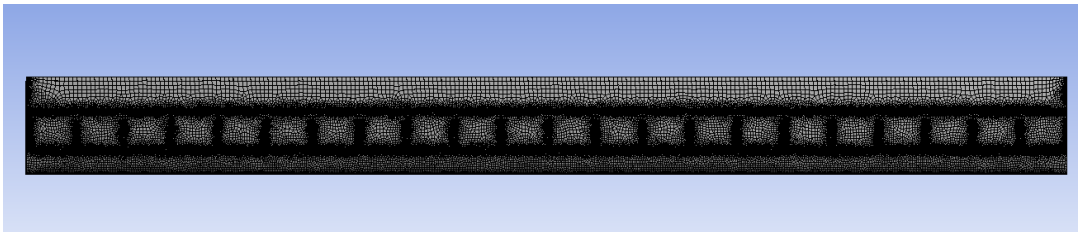

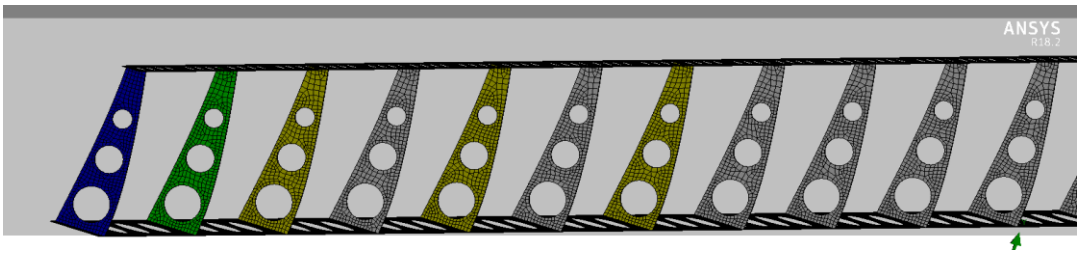

(a)

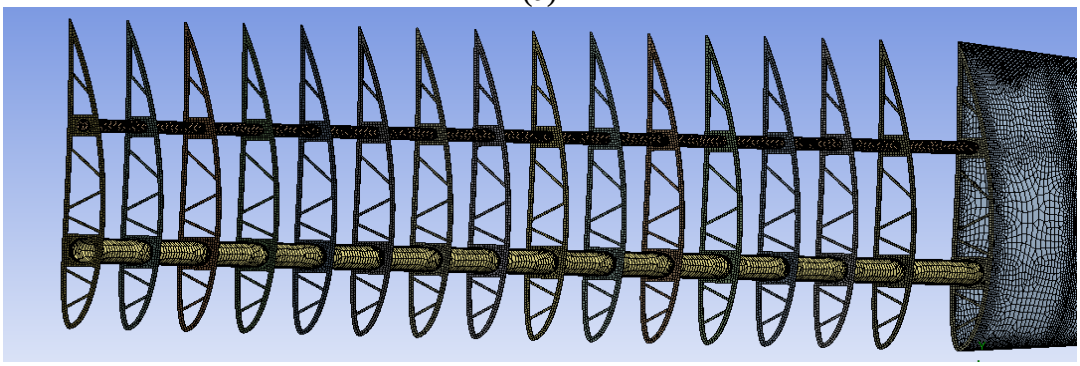

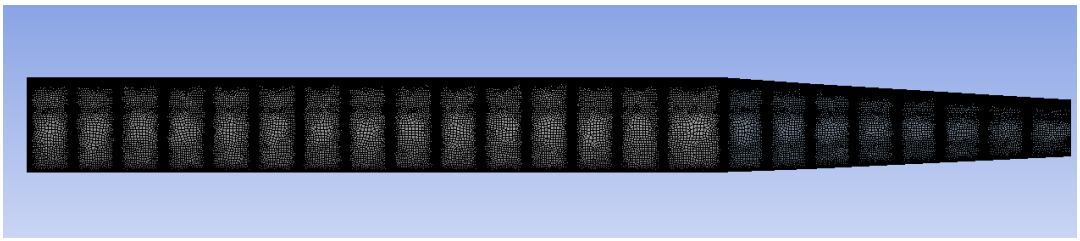

(b)

Figure 8- 3: Mesh of (a) wing structure 1 and (b) wing structure 2

The thicknesses, materials, and masses of individual wing component groups are listed in Tables 27 and 28. The structural weight of the aircraft is an important consideration when designing a solar-powered UAV. The weight of the structures is recommended to be around 40% of the total weight of the aircraft [132][36]. The structural mass of the wing, which is around 60 kg in our case, accounts for about 40% of the total mass of the aircraft.

Table 28. Characteristics of different elements of wing structure 1

Element	No	Material	Thickness [mm]	Mass [kg]
Spar	2	Epoxy Carbon UD	3	13.2
Skin	2	Mylar	0.16	11.22
Ribs	23	PLA	3	5.46
Total				29.85

Table 29. Characteristics of different elements of wing structure 2

Element	No	Material	Thickness [mm]	Mass[kg]
Spar	2	Epoxy Carbon UD	1.0	12.549
Skin 1	1	Mylar	0.15	6.82
Skin 2	1	Mylar	0.2	3.72
Ribs	23	PLA	3	7.107
Total				30.20

Although structural analysis of a highly flexible HALE wing should include unsteady loads and aeroelastic considerations in subsequent design phases, we begin our analysis by considering the steady cruising condition in which the aircraft should spend most of its operational life. The wing structure is clamped on one end (lying in symmetry plane). Non-uniform pressure distribution, obtained from the fluid flow computation, is applied along the upper and lower surfaces of the wing, while gravitational (mass) loads are applied to the complete wing structure. In future studies, critical loads appearing in manoeuvres or unsteady gusts, as well as aeroelastic occurrences, should also be investigated.

Table 30. Value of deformation and stress for wing 1 and Wing 2 after the simulation.

	Deformation [m]	Stress [MPa]
Wing 1	5.23	471
Wing 2	2.68	1310

Figures 8-4 and 8-5 show computed displacement and stress fields along the wing surface. The values of deformation and stress on the wing are shown in Table 30. As expected, the greatest displacement appears at wing tips which are 5.23 m for wing 1 and 2.68 m for wing 2. Given that the half-span of the wing is nearly 16 m, total deformation would be around 32% for wing 1 and 16% for wing 2. A 50% less deformation can be achieved by introducing a dihedral wing. Formation of undulation emerged at the trailing edge of the first portion and the leading edge of the second section of wing 2.

The undulation could be reduced by using skin with a thicker layer of Mylar (in reality, the wing's upper surface will be covered by solar panels, which will also contribute to stiffness).

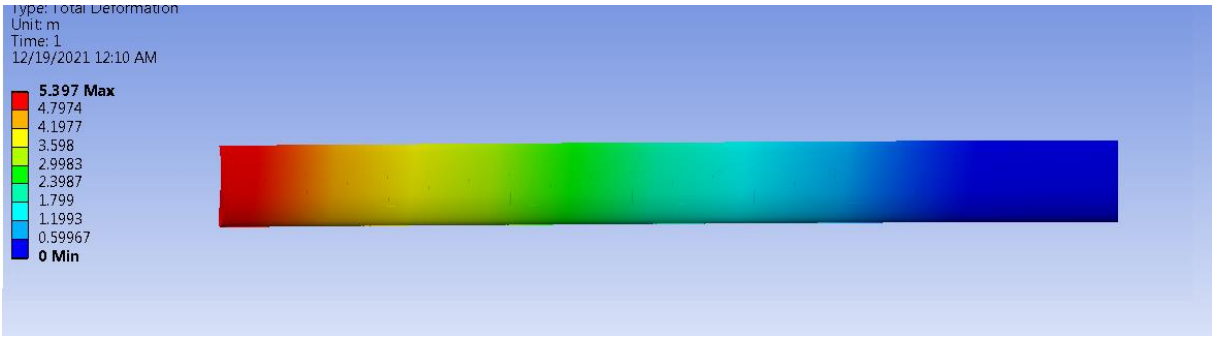

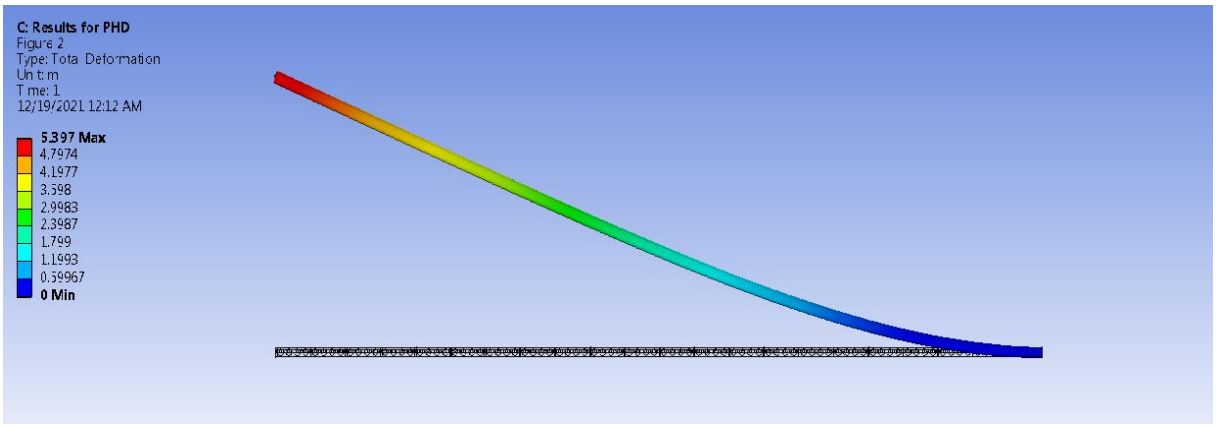

(a)

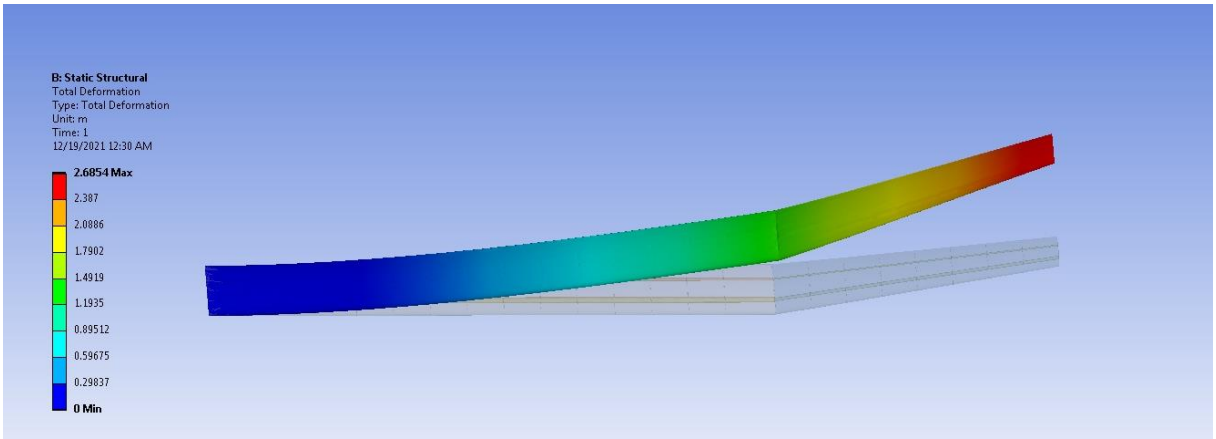

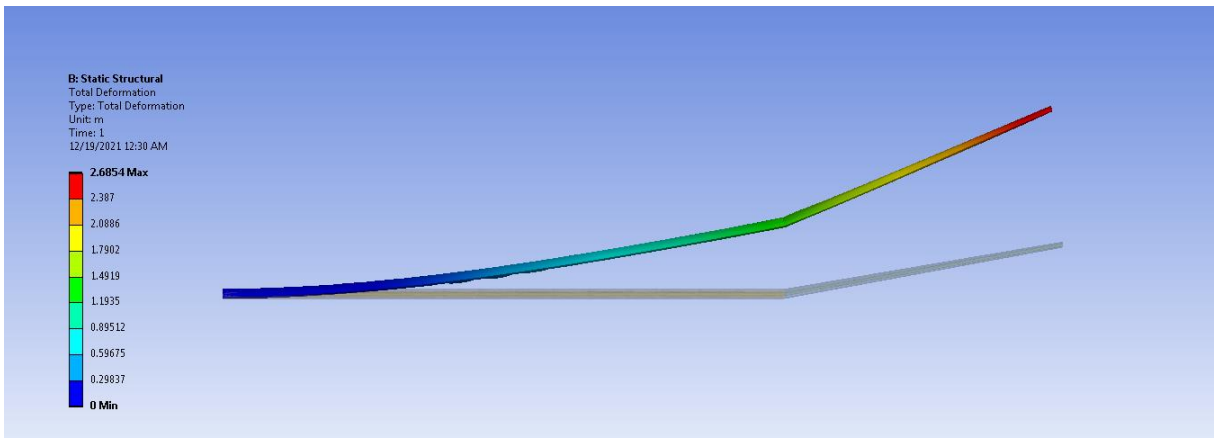

(b)

Figure 8- 4: Deformation of wing 1 (a) and wing 2 (b)

The greatest stress values of wing one and wing 2 are 471 MPa and 1310 MPa, respectively, which appear near the root of both wings' spars. Although these values may seem high at first glance, it can be seen from Fig. 8-5 that colour patterns in the root section of the spars correspond to the values around 200 MPa for wing 1 and 400 MPa for wing 2. The fact that the obtained stress levels are lower than the stress limits of carbon plies validate the assumed wing structure (that weighs approximately 60 kg in total) and proves that the structure will remain operational even if exposed to greater and/or unsteady load factors (that might appear while performing different flight manoeuvres).

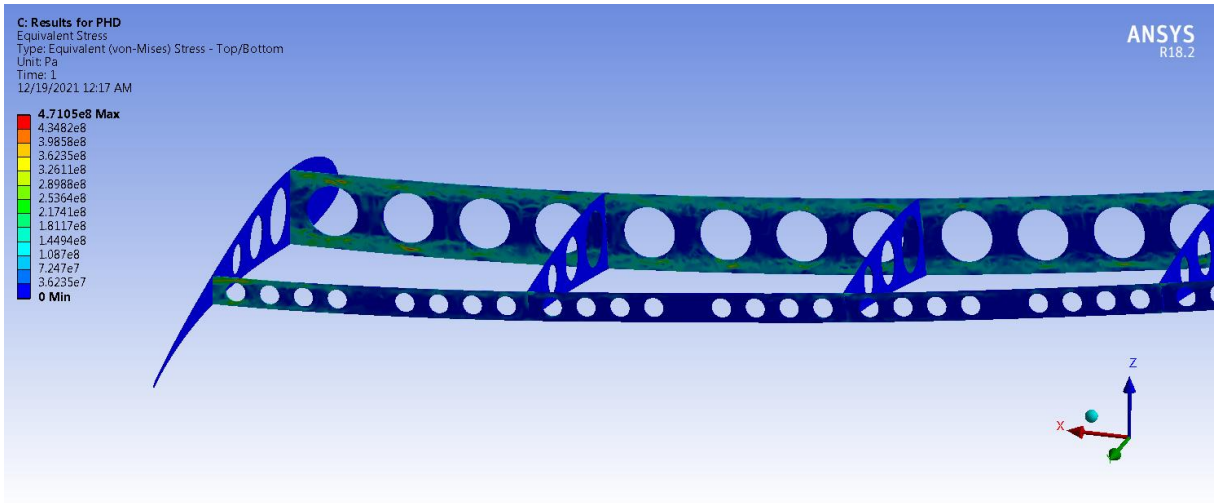

(a)

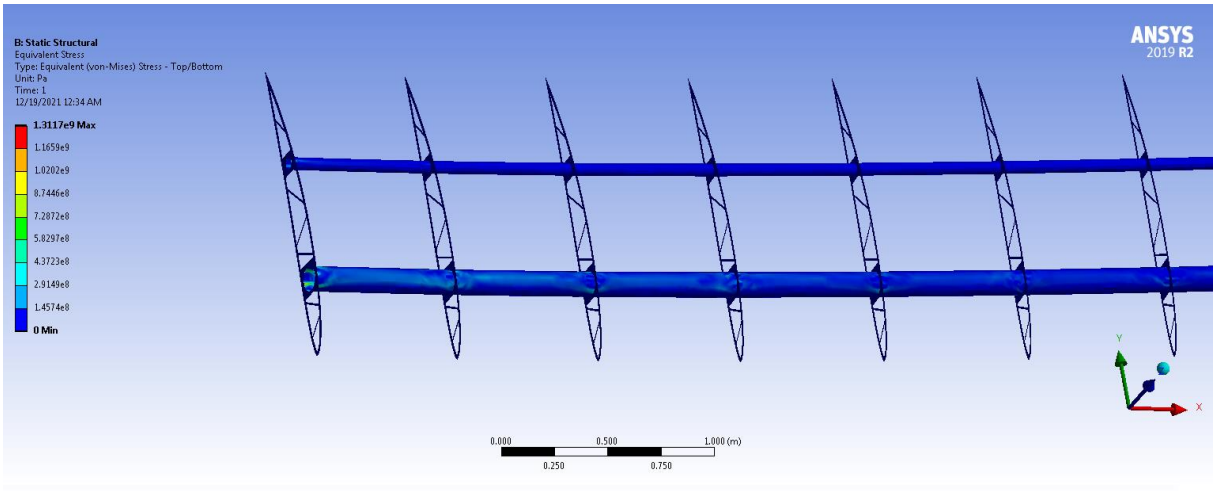

(b)

Figure 8- 5: Visualization of equivalent stress along the wing 1 (a) and wing 2 (b)

8.4 Modal analysis

Modal analysis is used to determine the dynamic features of a system, such as natural frequency, mode shapes, and so on, by studying the dynamic behaviour of mechanical structures under dynamic excitation. It helps in reducing the amount of noise that the system emits into the environment and identifying the causes of vibrations that affect the integrity of system components. Furthermore, modal analysis of a given structure is very important for determining the structure's functionality and behaviour under different expected and unpredictable static and dynamic load cases.

Modal analyses were performed using commercial software ANSYS. It enables the user to perform modal analysis by FEM. The same meshes from the structural analysis are used here. Both wings were clamped at one end and free-modal analyses were performed. After the analysis, both wings show similar mode shapes, two flap-wise modes and one edge-wise mode. Table 31 shows the first three natural frequencies of wing one and wing 2. It can be seen that the frequencies of mode one and mode 2 of wing 2 are around 29 % and 26 % more than wing one, respectively, but the frequency of mode 3 for wing 1 is 9 % more than wing 2.

Table 31: The first three natural frequencies of wing 1 and wing 2 from modal analysis

	Wing 1 Frequency [Hz]	Wing 2 Frequency [Hz]
Mode 1	0.301	0.39
Mode 2	1.266	1.596
Mode 3	1.899	1.743

Patterns of the first three modal shapes are depicted in figures 8-6 and 8-7, respectively. Wing 1 shows flap-wise vibration in modes one and 3, whereas wing 2 shows the same vibration at wings 1 and 2.

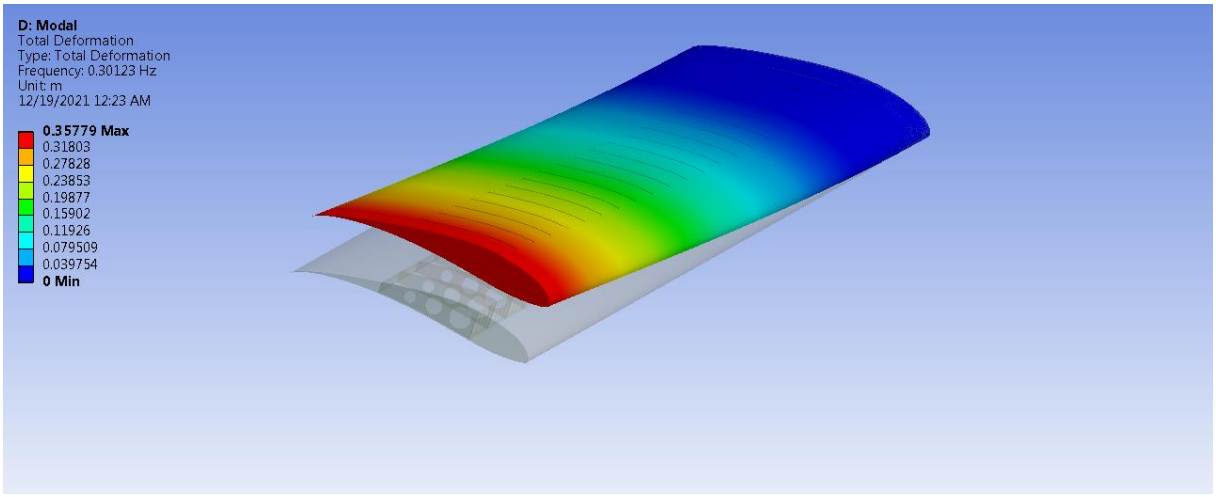

(a)

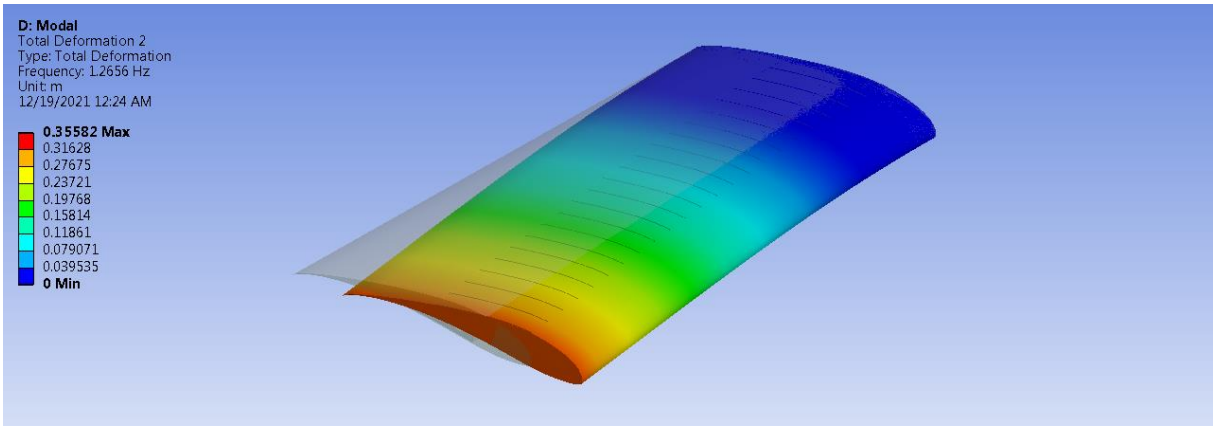

(b)

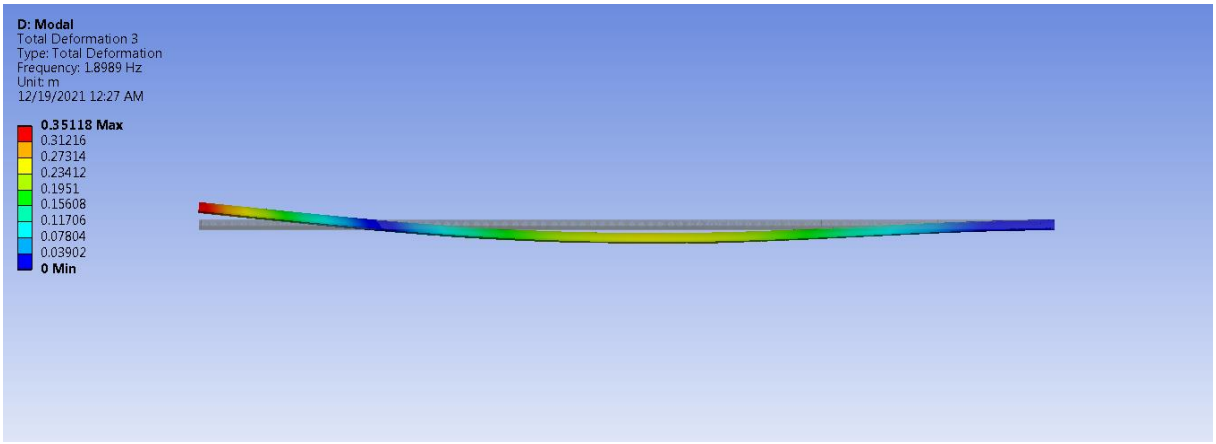

(c)

Figure 8- 6: Patterns of modal vibration. (a) Mode 1; (b) Mode 2; (c) Mode 3 of wing 1

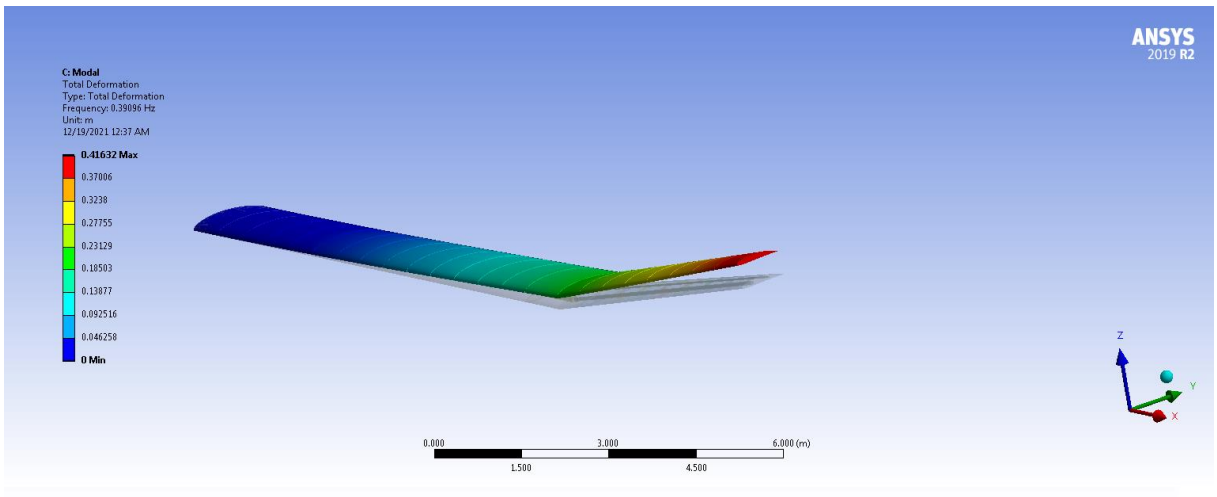

(a)

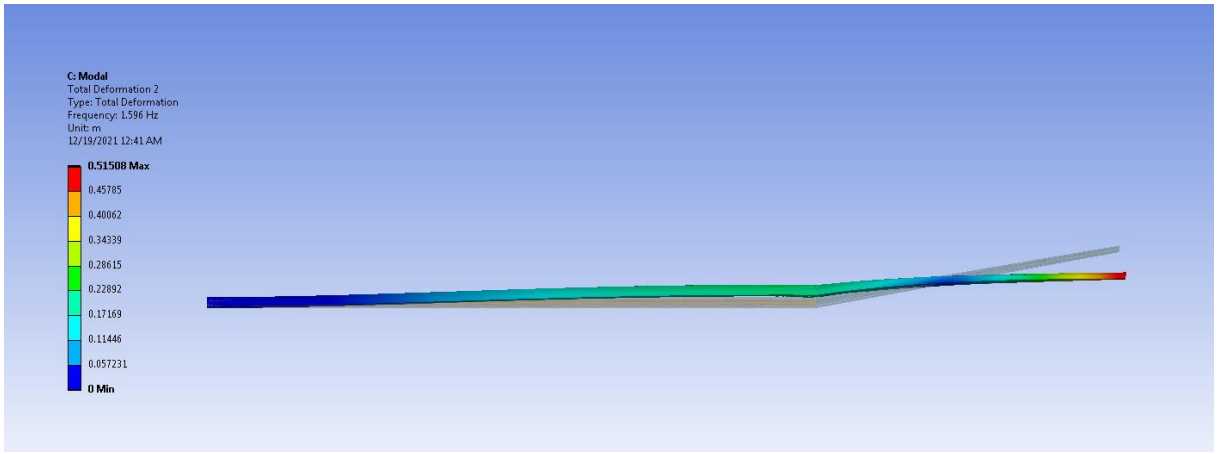

(b)

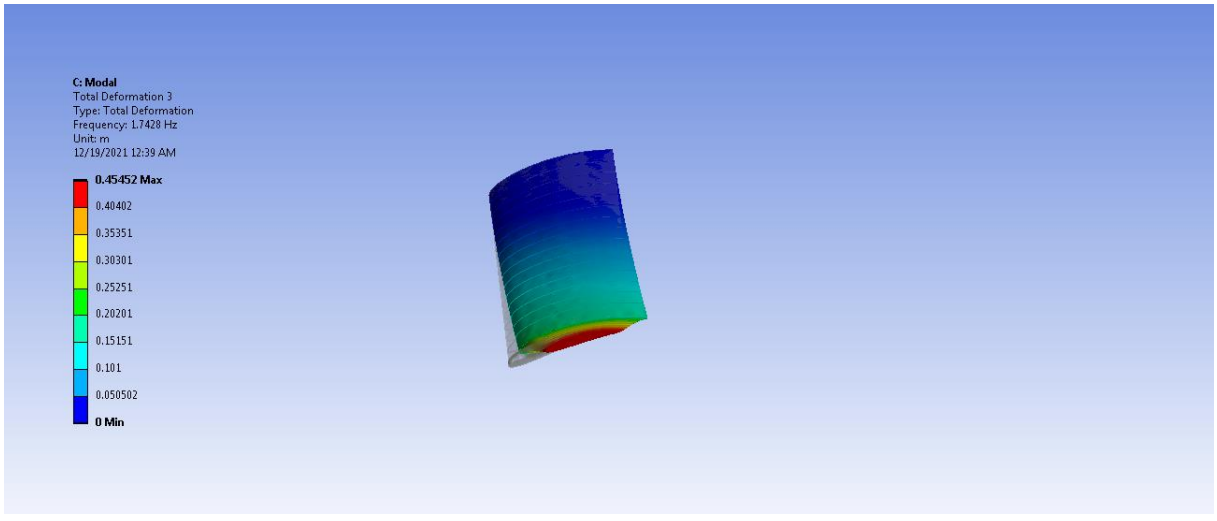

(c)

Figure 8- 7: Pattern of modal vibration. (a) mode 1; (b) mode 2; (c) mode 3 of wing 2

9. Propeller Design

A high-efficiency propulsion system is required for the extended duration, low energy consumption, and high-security features [133]–[136]. HALE usually fly between 17 and 25 kilometers above sea level, where the environment differs dramatically from that on the ground. As a result, the propeller runs in significantly less dense air, resulting in a low Reynolds number. Furthermore, the progress velocity (about 10–30m/s) is exceedingly slow. These aircrafts must meet such rigorous design standards in terms of weight, aerodynamics, structural design, propulsion, energy storage, control, and onboard technology. They must also use cutting-edge technology and innovative methods and solutions. An alternative power system is one such component, which incorporates solar panels with an efficient electric system to drive (usually several) aerodynamically optimized light-weight propellers capable of operating in a wide range of working environments, from sea level to a few dozens of kilometers where density is reduced by more than ten times. Propeller performance is correctly predicted and analyzed to establish a robust and efficient mission profile. As a result, propeller design and performance prediction are two of the most important technologies required for the development of the aircraft [38], [43], [44], [81], [137]–[142].

This chapter presents a conceptual design of such a propeller realized through multi-objective and multidisciplinary optimization procedure. A genetic algorithm is used to conduct a tightly coupled aero-structural two-criteria optimization to define a laminated blade with the best aerodynamic performance (expressed here through maximal efficiency, though other aerodynamic quantifiers might also be used) and minimal mass that is also statically and dynamically reliable when subjected to aerodynamic, inertial, and gravitational loads in cruising conditions. For this project, two equal propellers (with a diameter of D = 2 m) are envisaged. From these two criteria, cruising height of 20000 m and cruising speed of 25 m/s, the necessary amount of thrust as well as the working environment of each propeller can be determined. Previous chapters determined the mentioned details of the planned airplane wing. The listed details on the designed aircraft wing were determined in previous chapters. The applied methodology enables reviewing a large number of viable designs (differing in geometric features, used materials, lay-up sequences, etc) in a relatively short amount of time and choosing the most appropriate answer from several important design aspects out of a large group of generated solutions [74].

9.1 Blade geometry

In the beginning, blade geometry should be studied and simplified to allow for the definition of a parameterized model that can be successfully employed in multiple aerodynamic and structural computations. In general, the radial distributions of the airfoil (i.e. relative thickness and curvature), pitch, and chord totally determine the operational (streamlined) component of any considered blade. Here, the rotor diameter is fixed to D = 2 m, the propeller is assumed as two-bladed (N_b = 2) and the blade tip-speed is set to V_{tip} = 170 m/s (in order to avoid the compressibility effects). For simplicity, only the streamlined blade portion ranging in $y/R \in$ [0.35, 0.50, 0.65, 0.80, 0.90, 0.95] is modeled by the six listed cross-sections, while root and tip sections are neglected. An example of a generated geometric model is illustrated in Figure 9-1. Three coordinate axes are clearly visible.

Each characteristic cross-section is determined by the local airfoil shape, pitch and chord. In order to define the new blade root and tip airfoils (specifically designed for this type of aircraft and its high cruising altitudes), class-shape transformation (CST) technique is employed while the four intermediate blade cross-sections are obtained by interpolation. The other two important distributions, i.e. pitch and chord distributions, are assumed as 2nd order polynomial curves. In total, 17 continuous input parameters are used to unambiguously define different blade geometries enabling practically infinite number of design possibilities.

9.1.1 Airfoil parameterization

Class- Shape Transformation (CST) method discussed in section 5.3.2, is adopted for the parameterization of the root and tip (i.e. the first and last) airfoil.

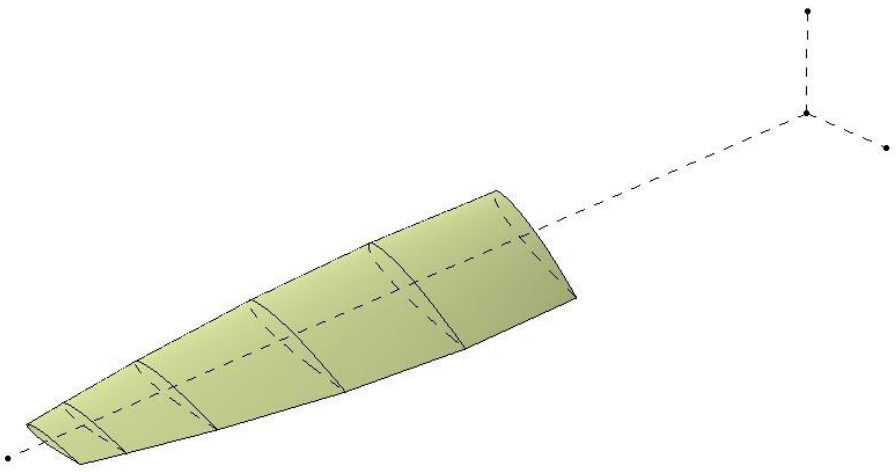

Figure 9- 1: An example of the simplified blade geometry [142]

Bernstein polynomials of second order (as employed in this study) are illustrated in Figure 9-2, along with the addends that define the half-contour of the airfoil. Thus, three coefficients are utilized to characterize the pressure and suction sides of the root and tip airfoils, yielding a total of 12 input parameters describing the radial thickness and curvature distributions.

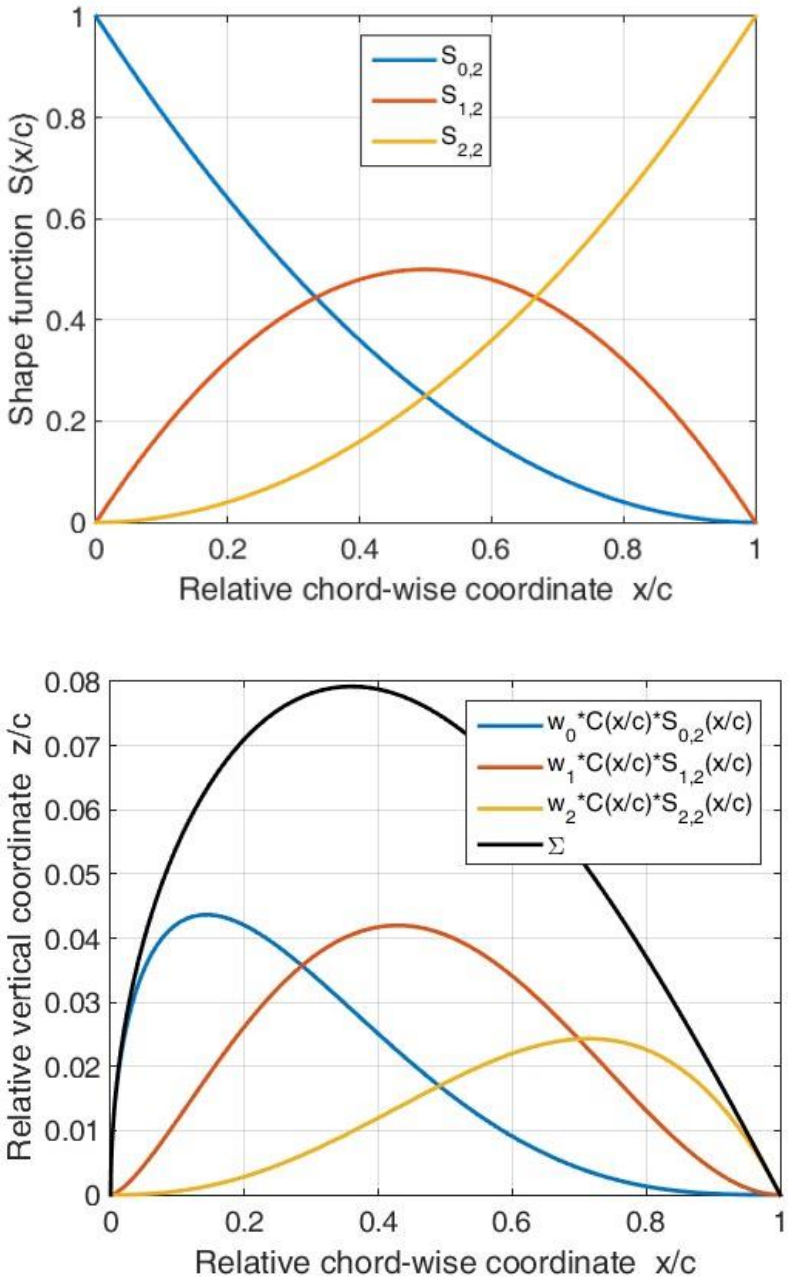

Figure 9- 2: a) 2nd order Bernstein polynomials, b) Representation of airfoil half-contour [142]

Although the first 12 input parameters all represent weighing coefficients, their assigned limits of design space vary because they are used to characterize different geometric aspects. In other words, the airfoil's lower surfaces are determined by negative values, while its upper surfaces are determined by positive values. The w_i values are also more restricted at the tip portion due to the thinner airfoils

than in the root section. Table 32 lists the boundaries of a part of the design space (referring to the airfoil distribution).

9.1.2 Pitch and chord distribution

Both span-wise pitch and chord distributions are considered to be quadratic functions with three parameters in general. However, because one further assumption is made here, namely that local pitch at $0.7R$ must equal 0, the pitch distribution is already limited, and two coefficients are sufficient to define it. Local airfoil rotation occurs around a point around 40% of the chord length along the whole blade. Furthermore, the collective angle $\theta_0 = 20°$ is the same for all blade models in order to ensure an impartial and fair comparison of the aerodynamic characteristics of variable pitch propellers.

Table 32. Limits of the coefficients used to describe the airfoils [142].

	$w0$	$w1$	$w2$
Lower root	$[-0.500, -0.100]$	$[-0.400, -0.050]$	$[-0.300, -0.050]$
Upper root	$[0.100, 0.500]$	$[0.050, 0.400]$	$[0.050, 0.300]$
Lower tip	$[-0.250, -0.050]$	$[-0.200, -0.025]$	$[-0.150, -0.025]$
Upper tip	$[0.050, 0.250]$	$[0.025, 0.200]$	$[0.025, 0.150]$

As a result, there will be 17 geometric parameters in all (where 5 referring to pitch and chord sequence are added to the previously mentioned 12). Figure 9-3 shows some examples of well-defined distributions of pitches and chords.

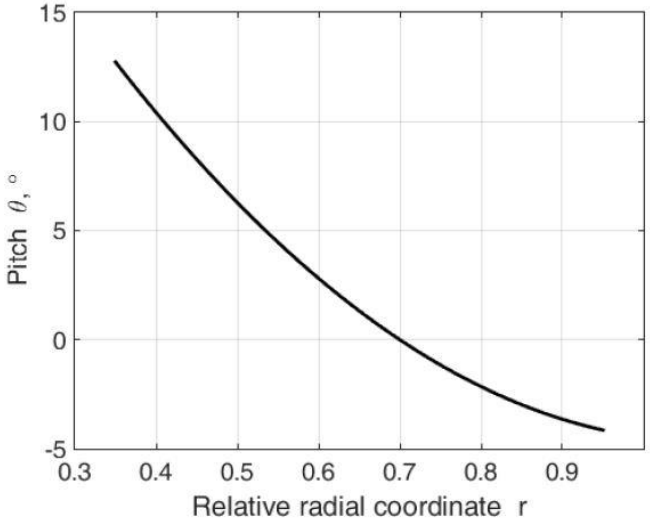

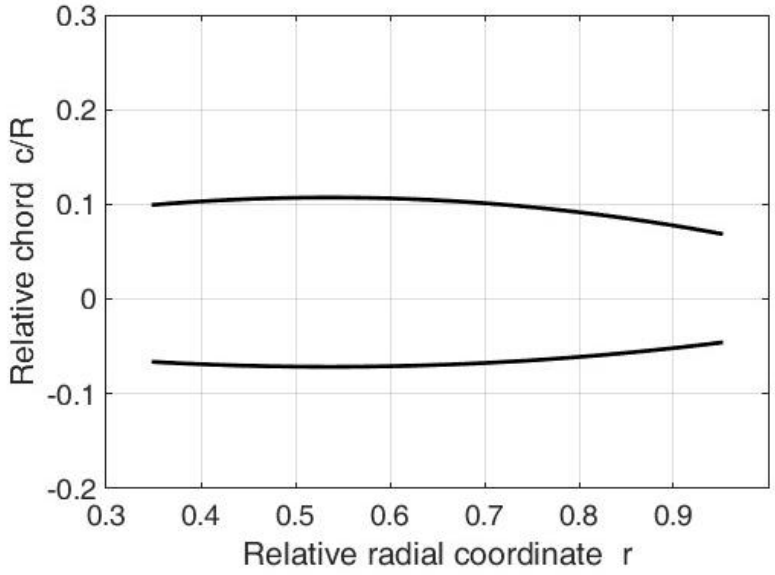

Figure 9- 3: a) An example of pitch distribution, b) An example of chord distribution [142]

In the end, the assumed pitch distribution can be written by Eq. (31):

$$\theta(r) = a_1(r^2 - 0.7^2) + b_1(r - 0.7) \tag{31}$$

where $0 \leq a_1 \leq 1$ and $-2 \leq b_1 \leq -1$.

Similarly, the assumed chord distribution can be written by Eq. (32):

$$c(r) = R(a_2 r^2 + b_2 r + c_2) \tag{32}$$

where $-1.0 \leq a_2 \leq 0.2, -0.5 \leq b_2 \leq 1.5, and -0.3 \leq c_2 \leq 0.2$

Aside from this, higher-degree polynomials can be used to describe the previously mentioned radial distributions, to increase the number of characteristic cross-sections, to model the entire blade (although the root and tip sections do not contribute significantly to aerodynamic performances), or to also vary blade radius, angular velocity, blade number, collective, etc.

9.2 Estimation of blade aerodynamic performances

It is possible to estimate the aerodynamic performance of a blade once the geometry has been established. However, it may be beneficial to replicate the design's extremely particular working conditions.

9.2.1 Nominal operating conditions

The designed propeller of fixed radius is intended to produce sufficient thrust force T at the cruising height H_{cr} = 20 km where the expected:

- temperature is $t = -56.5°C$,
- speed of sound is a = 295 m/s (resulting in tip Mach number of 0.58),
- air density is ρ = 0.088 kg/m3 (nearly 14 times smaller than at the sea-level),
- dynamic viscosity is $\mu = 1.4323 \cdot 10^{-5}$ Pa s.

The adopted combination of the cruising velocity, rotor angular speed and radius, as well as possible chord distributions result in a relatively low advance ratio $J = {\pi V_{cr}}/{V_{tip}} = 0.462$ and blade Reynolds number of approximately 100000.

9.2.2 Blade element momentum theory (BEMT)

For the estimation of propeller aerodynamic performances, various numerical algorithms (varying in complexity and starting physical assumptions) can (and have) been utilized [43], [142], [144]. During the conceptual design phase, the blade element momentum theory (BEMT) that takes into account tip losses is used because it is simple, fast, and accurate. In the end, it is a combination of two simpler models: BET and momentum theory (MT). BET considers the flow around discrete (and independent) blade segments (airfoils) and allows for the estimation of aerodynamic forces when local angles of attack are known, whereas MT is used to solve the system of equations and resolve changes in velocity in the axial and tangential directions, thereby elucidating velocity triangles on blade elements [141], as illustrated in Figure 9-4.

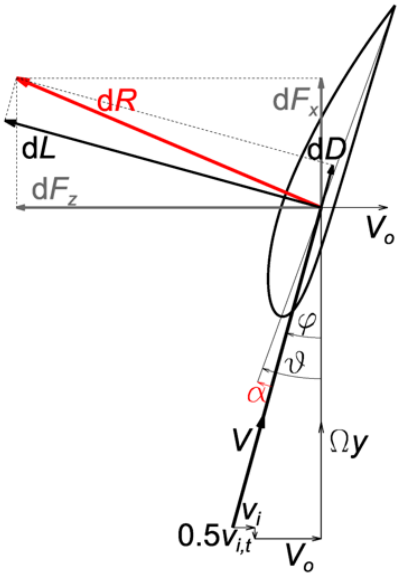

Figure 9- 4: Characteristic speeds and angles at a blade segment [142]

Induced velocities are usually quantified by induction factors, *a* and *a'*, as:

$$a = \frac{v_i}{V_0} \Rightarrow v_i = aV_0, a' = \frac{v_{i,t}}{2\Omega y} \Rightarrow v_{i,t} = 2a'\Omega y. \tag{33}$$

Local increments of the thrust force and torque appearing along the elemental ring (from MT) are:

$$\begin{aligned} dT &= 4\pi\rho V_0^2(1+a)aydy, \\ dQ &= 4\pi\rho V_0\Omega a'(1+a)y^3dy. \end{aligned} \tag{34}$$

The local induced angle φ and angle-of-attack α are respectively:

$$tg\,\varphi = \frac{V_0(1+a)}{\Omega y(1-a')}, \alpha = \theta - \varphi. \tag{35}$$

The relative (total) local velocity is:

$$\begin{aligned} V &= \sqrt{V_0^2(1+a)^2 + \Omega^2 y^2 (1-a')^2} = \\ &= \frac{V_0(1+a)}{\sin\varphi} = \frac{\Omega y(1-a')}{\cos\varphi}. \end{aligned} \tag{36}$$

On the other hand, from BET:

$$\begin{aligned} dT &= \frac{N_b}{2}\rho V^2(c_L\cos\varphi - c_D\sin\varphi)cdy, \\ dQ &= \frac{N_b}{2}\rho V^2(c_L\sin\varphi + c_D\cos\varphi)cydy. \end{aligned} \tag{37}$$

By equating expressions (35) and (37), it is possible to compute implicitly defined induction factors

as:

$$a = \frac{1}{G-1}, G = \frac{4\sin^2\varphi}{(c_L\cos\varphi - c_D\sin\varphi)\sigma'},$$
$$a' = \frac{1}{1+G'}, G' = \frac{4\sin\varphi\cos\varphi}{(c_L\sin\varphi + c_D\cos\varphi)\sigma'}, \quad (38)$$

for known local values of φ, $c_L(\alpha)$ and $c_D(\alpha)$ where $\sigma' = N_b c/(2y\pi)$ denotes local solidity. In general, eq.38 can be iteratively solved by conducting the following steps:

- initial assumption of a and a' (e.g. 0),
- calculation of local φ and α (eq.35),
- estimation of local $c_L(\alpha)$ and $c_D(\alpha)$,
- computation of new a and a' (eq.38).

The process is repeated until reaching converged values of induction factors, which is followed by the computation of relative velocity (eq.36) and aerodynamic contributions (eq.37). In the end, global values of thrust and torque are obtained by integration (summing) along the blade. If necessary, dimensionless coefficients of the propeller can also be computed:

$$C_T = \frac{T}{\rho n^2 D^4}, C_Q = \frac{Q}{\rho n^2 D^5}, C_P = \frac{P}{\rho n^3 D^5},$$
$$J = \frac{V_0}{nD}, \eta = \frac{TV_0}{P} = \frac{C_T J}{C_P}. \quad (39)$$

Although simpler than vortex methods or computational fluid dynamics (CFD) techniques (that could also be used when more computational power is at disposal), it is the best option for a preliminary optimization study in cruising conditions.

9.2.3 Airfoil characteristics

The lift and drag coefficients of airfoils at low Reynolds numbers (due to both low air density and small blade chords), which are required for successful propeller aerodynamic computation by BEMT, are first obtained using XFOIL [99] and then extrapolated to the full range of angles-of-attack by Montgomerie method [145]. This method combines a 2D potential flow trend at lower angles of attack with a flat plat behavior at higher angles of attack, while also including various 3D flow adjustments. In general, lift and drag coefficients can be approximated by an odd or even function. At this point,

the consequences of compressibility are ignored. An illustration of the computation and extrapolation of lift and drag coefficients is shown in Figure 9-5.

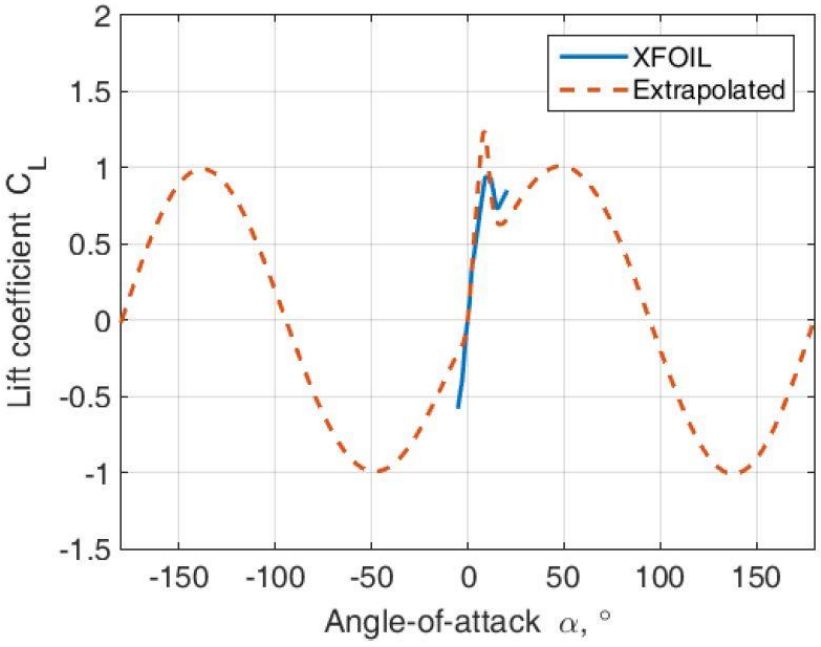

(a)

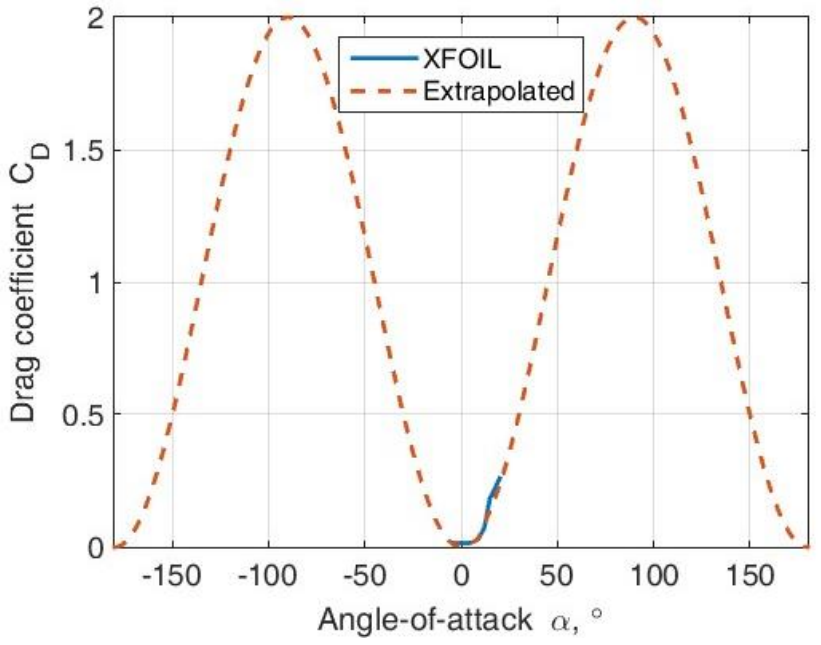

(b)

Figure 9- 5: An example of the used a) lift, b) drag coefficient [142]

9.2.4 Possible outcomes

The estimated values of thrust force T (or its coefficient C_T), required mechanical power P (or its coefficient C_P), and aerodynamic efficiency η at specific working conditions, such as collective angle and advance ratio, are among the most interesting and useful global results of aerodynamic computation of propellers. However, some local results (e.g., radial distributions around the blade)

that are typical for either optimal (nominal) or worst-case operating conditions can be extracted, providing greater insight into local flow occurrences and the quality of the intended airfoils. The estimated axial and tangential induction factors along the operating region of the blade are shown in

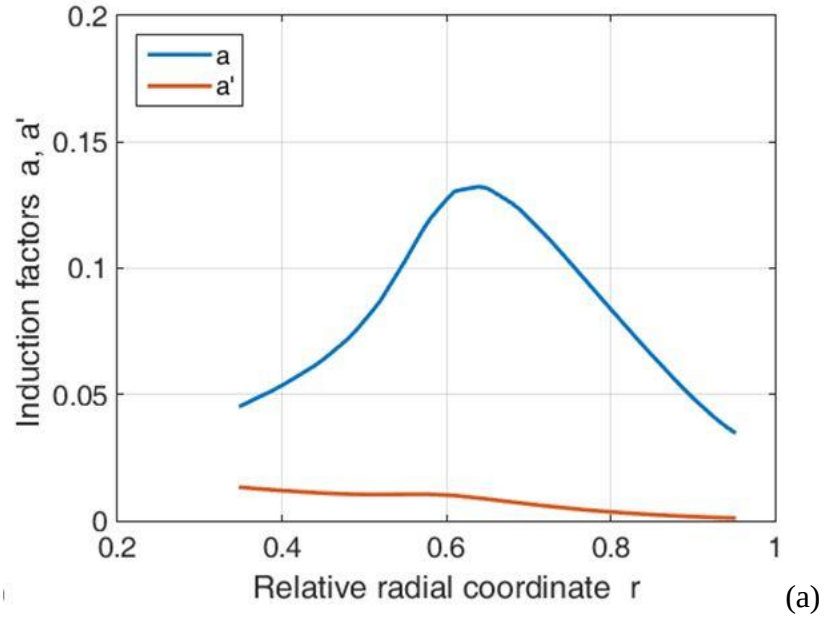

(a)

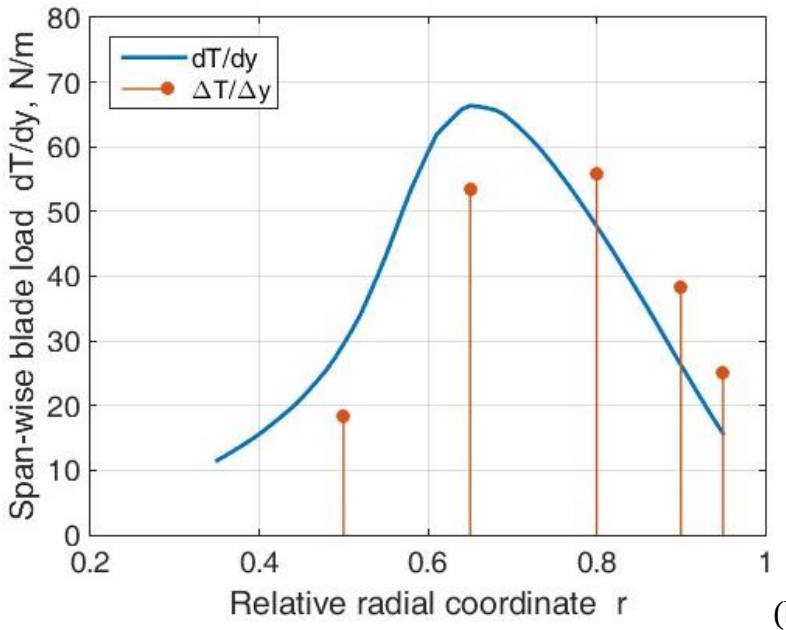

(b)

Figure 9- 6: Estimated: a) induction factors, b) load along the blade [142]

Figure 9-6(a). The outer portions of the blades may be seen to gain significant axial flow acceleration (indicating that the propeller operates as designed). Figure 9-6 (b) depicts the aerodynamic load distribution, which can be employed in the future structural study of the blade. That is to say, a one-way connection (interaction) between flow (fluid) and structural (solid) computation can be relatively

easily achieved. Simplified, discrete load distribution that was actually imported into the structural analysis is colored in red in Figure 9-6 (b).

Additionally, it is possible to consider a greater number of operating regimes, better estimate airfoil aerodynamic characteristics, employ a more complex flow model, perform aero-acoustic simulations, consider the effects of propellers on the remainder of the aircraft (i.e. its wing and fuselage), etc.

9.3 Blade structural analysis

The outer shell of the blade is assumed to be the only laminated composite component in the structural model, in an effort to simplify manufacture and save costs. In Table 33, the mechanical parameters of the uni-axial glass or carbon plies are listed, while their single ply thickness of 0.1 mm is assumed to be constant. Since two different lay-up sequences are tried:

• constant (uniform) along the blade described by $[\theta_{1_{n1}}/\theta_{2_{n2}}/\theta_{3_{n3}}/\ \theta_{2_{n2}}\ /\theta_{1_{n1}}]$, or

• dropped ply lay-up sequence (going from the root to the tip) described by$[\theta_{1_{n1}}/\theta_{2_{n2}}/\theta_{3_{n3}}/\theta_{4_{n4}}$,

the number of additional structural input parameters varies between 6 $(\theta_1, n_1, \theta_2, n_2, \theta_3, n_3)$ and 8 $(\theta_1, n_1, \theta_2, n_2, \theta_3, n_3, \theta_4, n_4)$. In the second case, the blade is divided into 4 segments as illustrated in Fig. 7, and the number of plies decreases from the root to the tip. Also, inverted lay-up sequences are applied along the upper and lower blade surfaces. Number of plies n_i ranges from 1 to 20 (or 25 in the case of dropped plies), whereas ply orientation θ_i can take the values from the set [−90° : 15° : 90°] where 0° denotes the longitudinal axis of the blade.

The blade is constrained (clamped) along the 1st (root) cross-section. A safety factor of 1.25 is applied to the assumed structural model throughout the remaining five outer cross-sections after the aerodynamic loads, inertial forces, and gravitational forces have been estimated using BEMT (as previously explained). Each generated blade model's static and dynamic structural behavior is estimated using the finite element method (FEM).

Table 33. Mechanical properties of uniax fiberglass and carbon plies [142].

Property	Fiberglass	Carbon
ρ, kg/m^3	1737	1540
$E1$, GPa	42	209
$E2$, GPa	9.72	9.45
$G12$, GPa	6.48	5.50
$\upsilon 12$	0.30	0.27
$F1t$, MPa	710	1979
$F1e$, MPa $F2t$, MPa	-343 16	-893 26
$F2e$, MPa $F6$, MPa	-16 25	-139 100

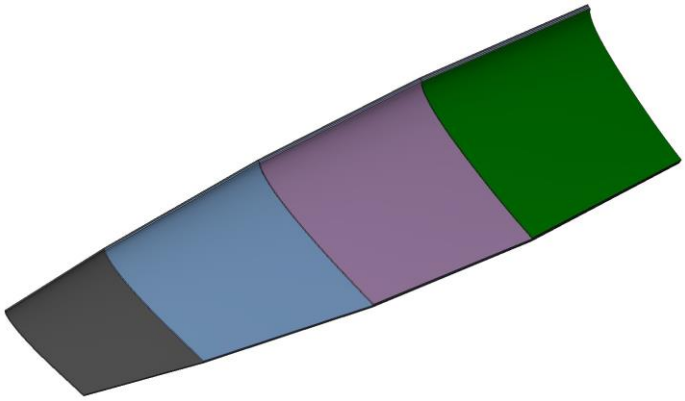

Figure 9- 7: Illustration of the dropped ply lay-up sequence along the lower surface [142].

An example of the generated finite element model together with the applied loads and constraints is illustrated in Figure 9-8.

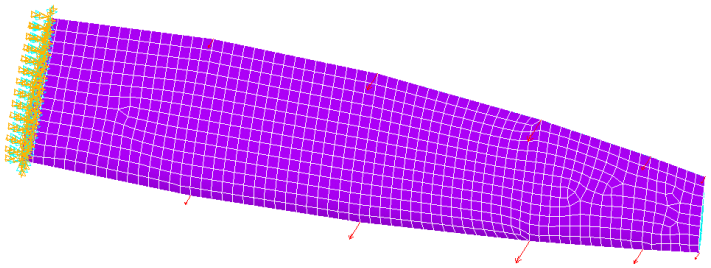

Figure 9- 8: An example of the finite element model [142].

Along with the aerodynamic efficiency and blade mass, other output parameters (i.e. goal functions) and constraints may include the maximum tip deflection (shown in Figure 9-9a), the maximum failure criterion along the blade (shown in Figure 9-9b), or the first few blade natural frequencies (both flexural and torsional shapes are shown in Figure 9-10, i.e. their differences to integer multiplies of nominal rotor angular frequency Ω. To the extent that it is practicable, it may also be worthwhile to attempt to quantify blade fatigue or manufacturing and maintenance costs.

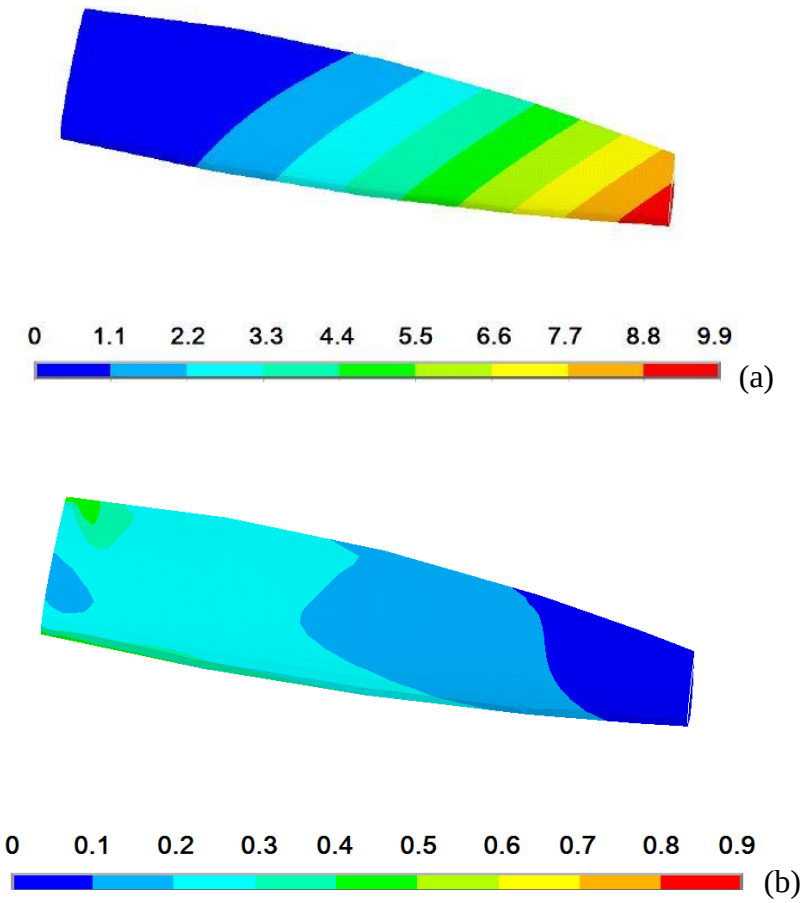

Figure 9- 9: Estimated: a) blade deflection in [mm], b) failure criteria along the blade [142].

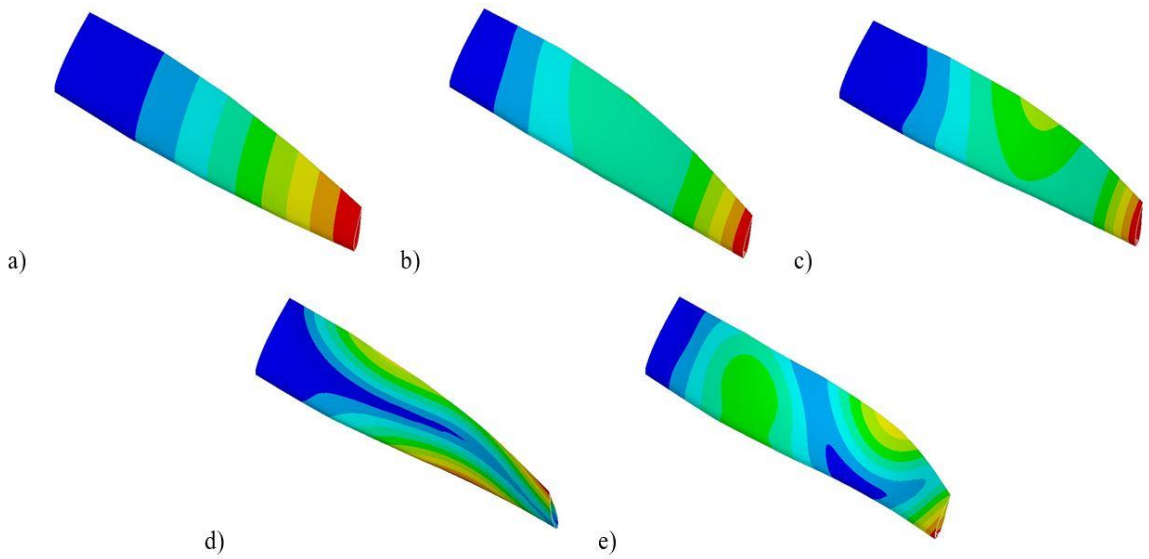

Figure 9- 10: Estimated natural modes: a) 1st, b) 2nd, c) 3rd, d) 4th, e) 5th [142].

9.4 Coupled multi-objective aero-structural optimization

The multi-objective optimization loop depicted in Figure 9-11 incorporates all of these individual (flow and structural) analyses (i.e. design phases). Due to its ability to be applied to a wide range of engineering challenges, the genetic algorithm (GA) was selected as a method for optimizing a wide range of engineering problems.

In this study, the number of input parameters is either 23 or 25. Two outputs (goal functions) are considered:

- aerodynamic efficiency (maximal value is desired), and
- blade mass (minimal value is desired).

Numerous geometric, aerodynamic and structural constraints are introduced. Few of them are listed below:

- Blade chord must have positive values and should decrease along the last third of the blade,
- Thrust force must be higher than 55 N,
- Relative tip deflection must be below 5%,
- Failure criteria must have satisfactory values (below 1) along the complete blade skin,
- Relative differences between blade natural and rotor angular frequencies must be over 20%, etc.

The population size is determined at 200 based on past studies and repeated calculations, and 25 generations (iterations) are generated (computed). The Pareto front (defined by the cost functions of the best individuals) and Pareto set (containing the best individuals described by the input parameters) are continuously formed throughout the iterative optimization procedure because a multi-objective approach was adopted.

It's also conceivable to use a different set of goal functions and constraints, use a different optimization strategy, use a novel, surrogate, or predictive model (based on artificial intelligence technologies) to speed up or improve the coupled computing, and so on.

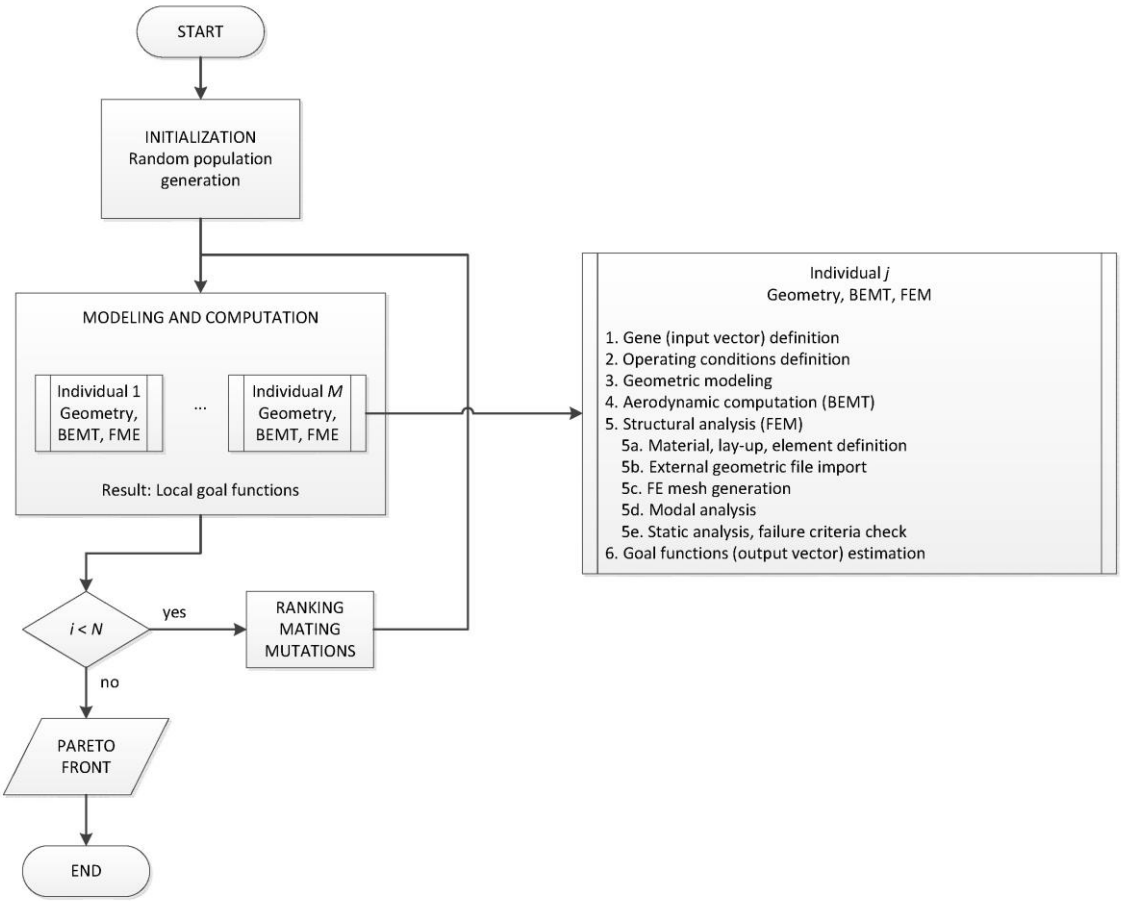

Figure 9- 11: Flowchart of the optimization loop [142].

9.5 Results and discussion

A short repetition of the initial HALE aircraft is performed prior to the examination of the collected results. To begin with, its takeoff weight is estimated to be 150 kilograms, with an estimated lift-to-drag ratio of 16. Figure 9-12 shows the finalized Pareto fronts. The estimated mass of the blades is generally between 0.4 and 0.8 kilograms, resulting in propellers weighing between 1 and 2 kilograms, which is a good fit for the aircraft's takeoff weight.

Surprisingly, both fiberglass and carbon dropped ply lay-up sequences appear to be capable of providing similar optimal results (blade mass as low as 0.4 kg at preserved high aerodynamic efficiency of nearly 0.9 can be achieved). However, despite the lower mechanical qualities of uniaxial glass plies in comparison to those of carbon plies, the results of the study show that, with the suitable dropped lay-up sequence, high-quality fiberglass blades can be built, even for high-altitude aircrafts.

When it comes to glass fibers, uniform lay-up sequences lead to a slightly heavier blade mass. To reduce production costs and complexity, it is ideal to use the uniformly layered carbon plies that have a streamlined blade that weighs approximately 0.64 kg.

Obtained optimal solutions can be presented in several different ways. E.g., Table 34 lists a portion of the Pareto set in the case of dropped ply fiberglass blades.

Due to the difficulty in understanding a tabular (purely numerical) representation, an illustration of some of the generated root and tip airfoil shapes (shown in Figure 9-13) may be more useful (where the numeration corresponds to the rows of Table 34). As expected, there are some similarities among the produced optima when using an evolutionary optimization technique such as GA. There are noticeable variances in root airfoils on the lower airfoil side. Additionally, all root airfoils have negative curvature, and their relative thickness ranges from around 14% to 17%.

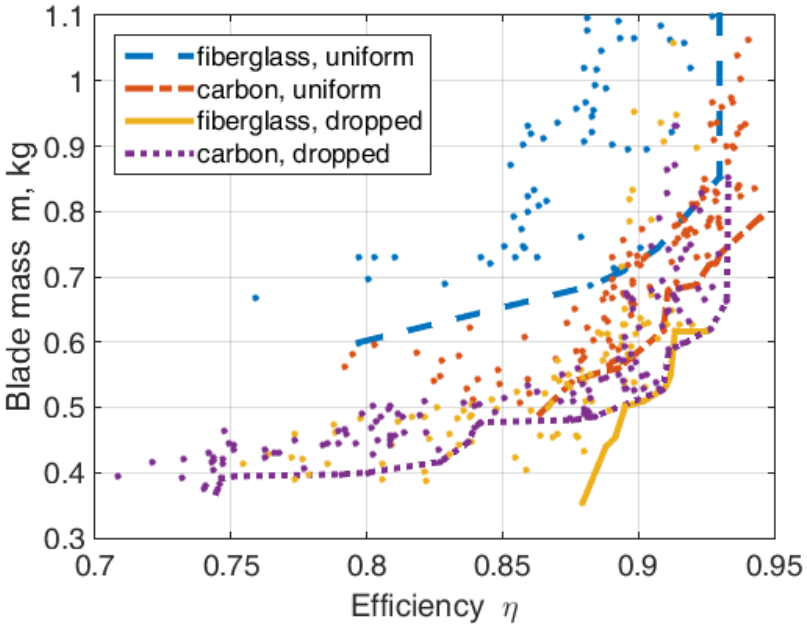

Figure 9- 12: Obtained Pareto fronts [142].

Table 34. Part of the Pareto set for dropped ply fiberglass blades [142].

x_1	…	$x_{18} = n_1$	$x_{19} = \theta_1$	$x_{20} = n_2$	$x_{21} = \theta_2$	$x_{22} = n_3$	$x_{23} = \theta_3$	$x_{24} = n_4$	$x_{25} = \theta_4$	$\sum n_i$
−0.3142	…	7	−15	8	−15	6	15	15	−30	36
−0.3142	…	7	−15	8	−15	6	15	15	−30	36
−0.3338	…	7	−15	5	−15	5	15	13	−75	30
−0.4212	…	6	−15	3	15	5	15	12	−90	26
−0.4085	…	7	−15	4	0	6	15	13	−75	30
−0.4112	…	7	−15	4	15	5	15	13	−75	29
−0.3220	…	8	−15	5	−15	7	15	14	−45	34
−0.2768	…	8	−15	7	−15	7	15	14	0	36
−0.3598	…	7	−15	6	−15	6	15	14	−60	33
−0.4041	…	7	−15	4	0	6	15	13	−75	30
−0.2768	…	6	−15	7	−15	7	15	14	0	36

On the other hand, generated tip airfoils mostly differ in the shape of the suction side, although the distinctions are almost negligible. On the other hand, generated tip airfoils mostly differ in the shape of the suction side, but the differences are insignificant. Tip airfoils have a positive but minor curvature, with a relative thickness of around 12 %.

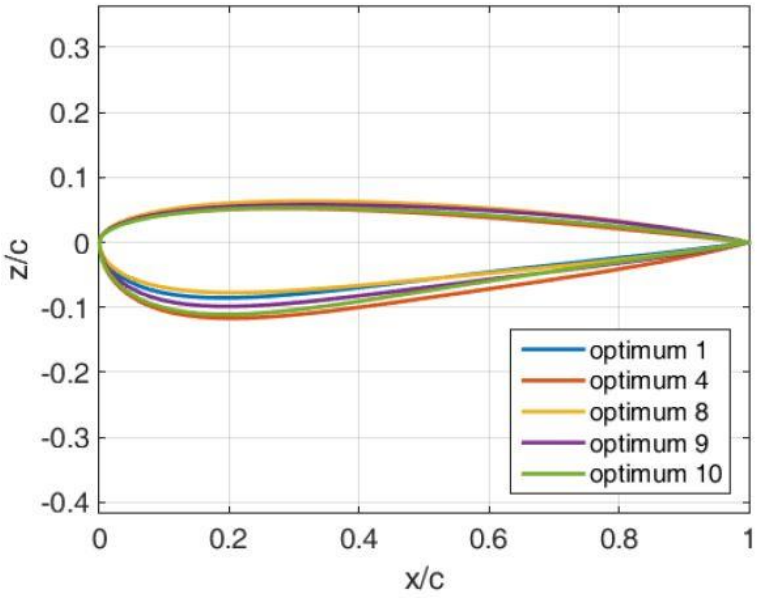

(a)

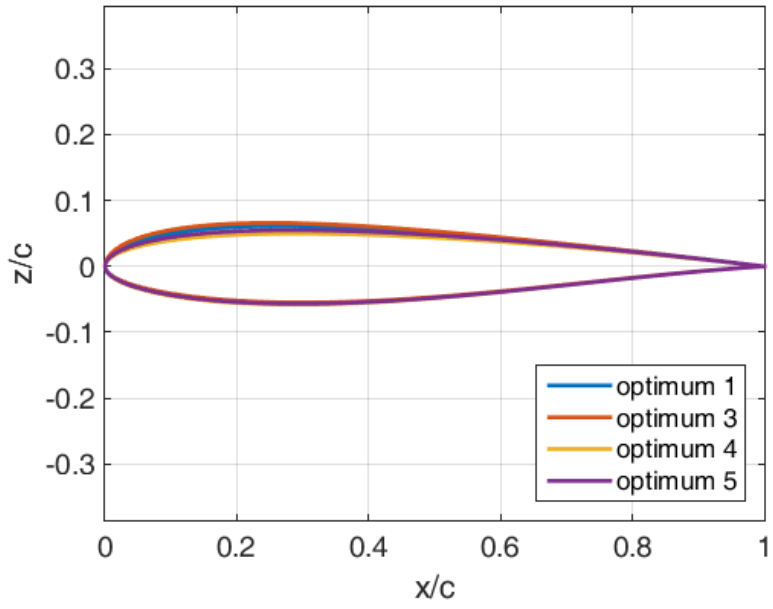

(b)

Figure 9- 13: Optimized: a) root, b) tip airfoils for dropped ply fiberglass blades [142].

For dropped ply fiberglass blades, the distributions of pitch and chord can be seen in Figure 9-14, which illustrates what the input parameter values actually signify. While the pitch distributions' gradients don't dip below −20° degrees in any direction, it can be seen that they are all descending in form. Blades with aspect ratios ranging from 6 to 8 tend to be the most popular, as are roughly rectangular shapes.

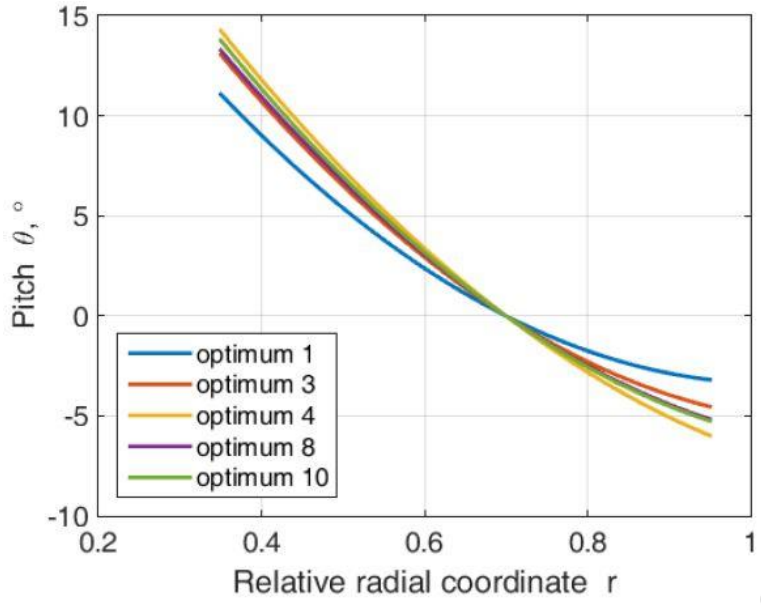

(a)

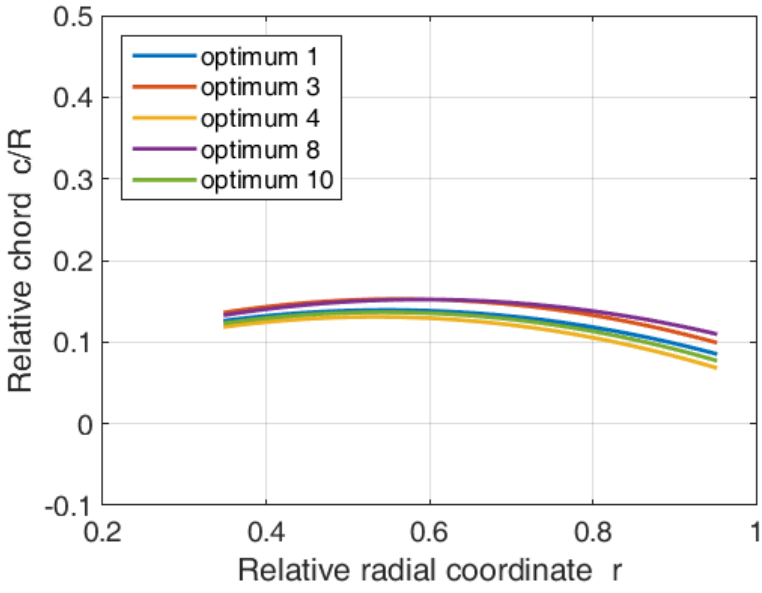

(b)

Figure 9- 14: Optimized: a) pitch, b) chord distributions for dropped ply fiberglass blades [142]

Figures 9-15 and 9-16 show histograms depicting the optimal structural parameter values for the best lay-up sequences for the dropped fiberglass and carbon plies, respectively. Plies marked by (n_1, θ_1) extend along the whole blade, while plies (n_4, θ_4) exist only in the root section.

For dropped fiberglass plies, it can be observed that the total skin thickness varies between 2.6 and 3.6 mm. All optimal blades have increased thickness in the root vicinity (recommended value of 4 is 14), while the other three numbers of plies are significantly lower. Also, ply orientations $\theta_1 = -15°, \theta_2 = -15°, \theta_3 = 15°$ are almost uniformly distributed, whereas the orientation of plies in the root section is quite dispersed (interestingly, all values are negative).

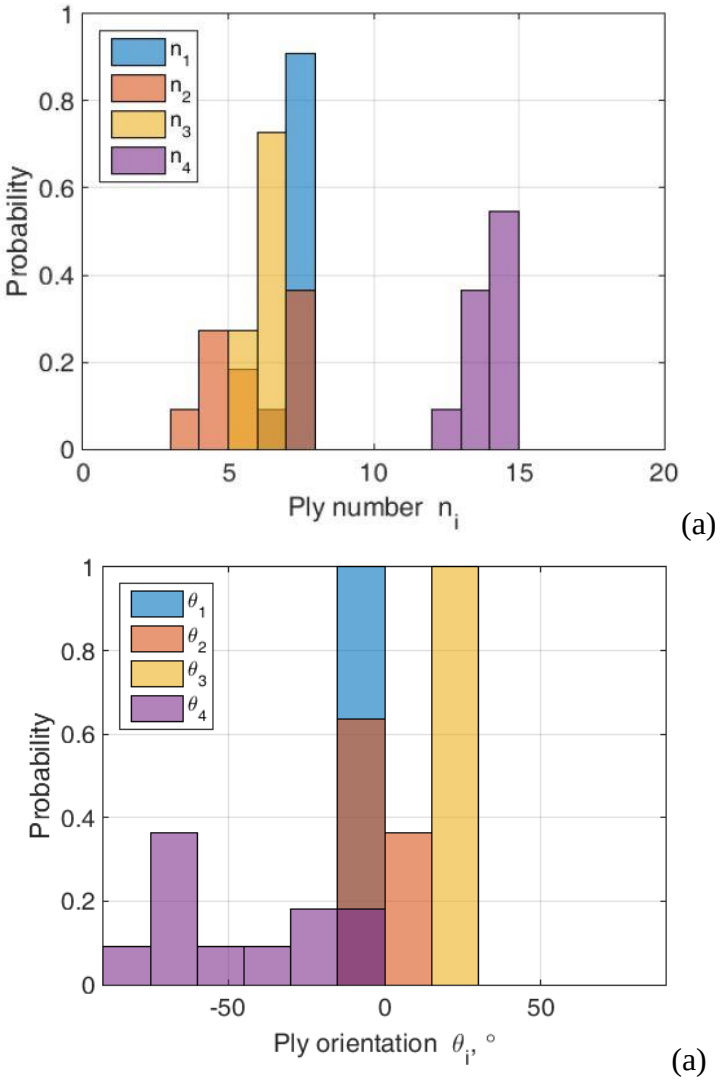

Figure 9- 15: Distribution of: a) number of plies, b) orientation of plies for dropped fiberglass ply blades [142].

Dropped carbon ply blades are in a different scenario. The root section of all optimal solutions should be further thickened, although the number of plies is much more distributed than in the previous case (and the total skin thickness ranges from 2 to 4.4 mm). For all laminae, however, the ply orientation tends to 0° and never deviates from [−45°, 45°].

Finally, as shown in Figure 9-17, the aerodynamic characteristics of "optimal" propellers at a wider range of working points (advance ratios) but constant collective angle can be compared. Fascinatingly, the optimization loop is so "smart" that it can pick (define) the blades with virtually maximum efficiency at the designed advance ratio. Instead of having to consider an entire array, it appears that using a single operational regime is adequate to provide "optimal" performance at a predefined collective. Only the streamlined portion of the blade in uniform (axisymmetric) flow was considered in the calculation of efficiency.

It's important to keep in mind that selecting a final solution from among a Pareto set of equally desirable optima is neither simple nor unique. Many factors come into play, but one of the most important is the designer's, i.e. engineer's, point of view. As a result, we leave the reader's decision up to them.

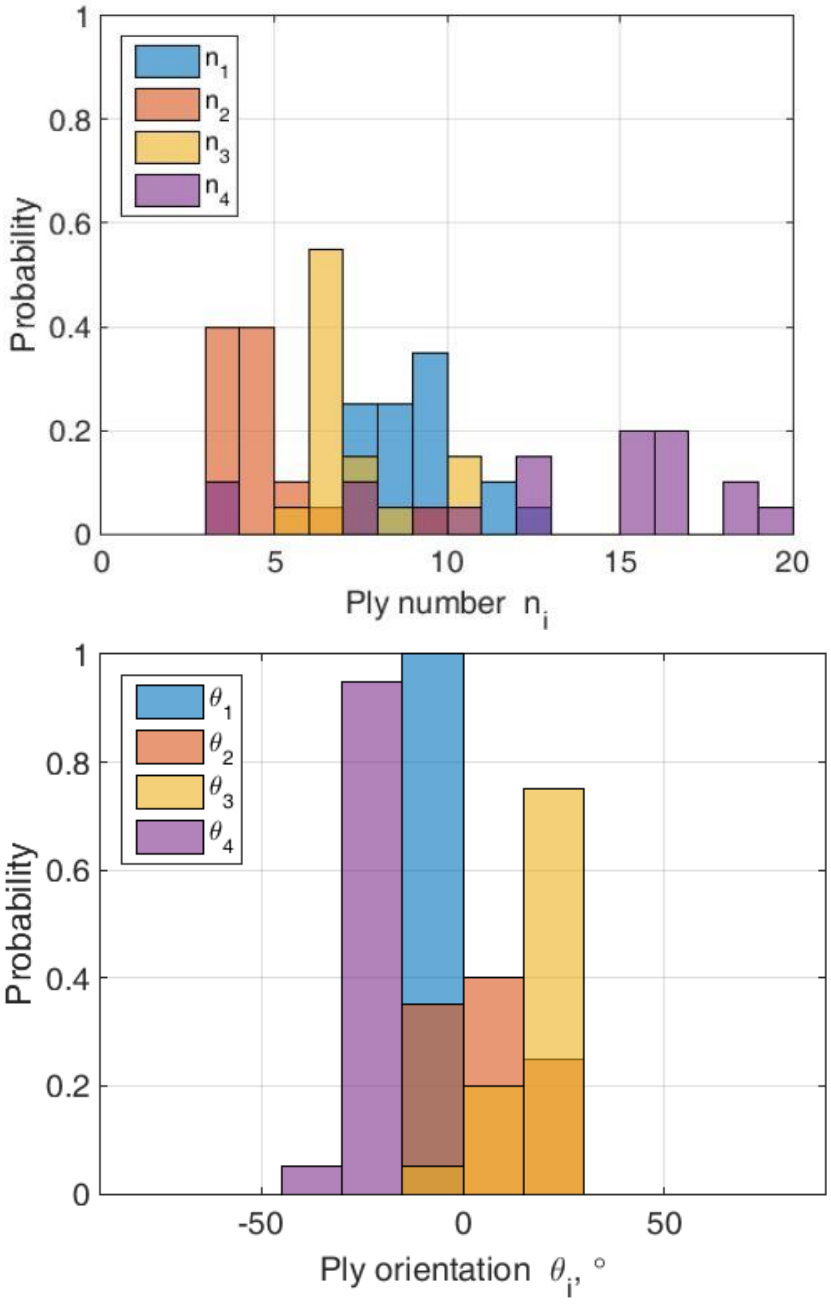

Figure 9- 16: Distribution of: a) number of plies, b) orientation of plies for dropped carbon ply blades [142].

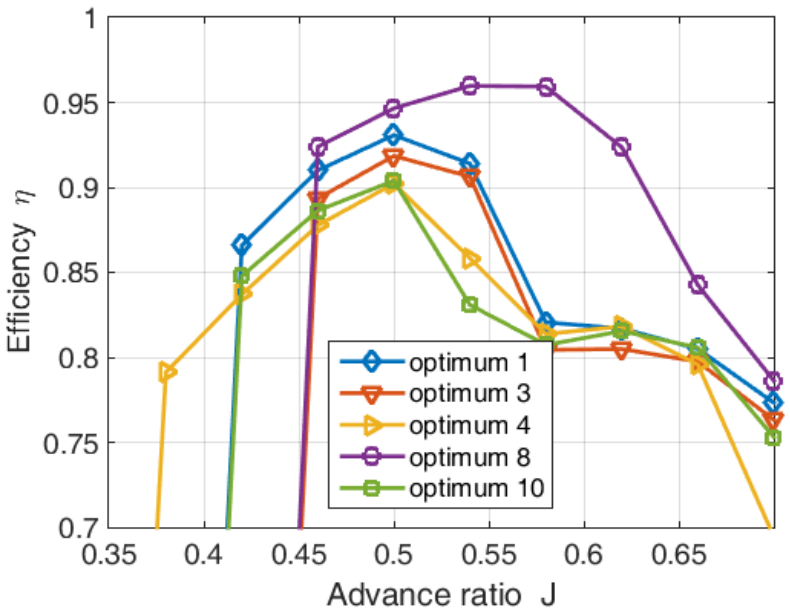

Figure 9- 17: Aerodynamic performances of “optimal” dropped fiberglass propeller blades [142]

10. Conclusion

This thesis presented some important findings in relation to the raised questions of HAPS design. Certainly, there are numerous challenges of HALE aircraft and their successful operation such as: the necessity of extremely low airframe weight, low air pressure and density cruising at high altitudes where air pressure and density are much lower than in the Earth's vicinity, sub-zero temperatures, exposure to increased radiation, low Re implying accentuated viscosity effects and decreased aerodynamic characteristics, assuring complete flight autonomy, need to generate the required energy for flight solely from solar energy, adequate sizing and control of rechargeable batteries, etc.

Finding the optimal relation for estimating the right empty mass for this sort of aircraft was one of the main challenges. The assessment of airframe mass is performed for HAPS UAV using all available and prevailing relations provided by Rizzo, Stender and A. Noth for solar-powered aircraft. For this kind of aircraft Stender equation gave the best results on finding airframe weight or empty weight. This study also aimed to investigate and accurately estimate the daily power requirements and battery mass. Although just a portion of solar energy can be converted to electricity, the performed investigation indicates that thin-film solar cells distributed along the upper surface of the wing (where at least 75% wing surface is used) can provide sufficient power for long endurance flight over Serbia and Bangladesh if their efficiency is 0.23-0.31. In the future, their performance can be additionally improved by developing smart control strategies.

The use of a high lift airfoil in the design of a long endurance UAV is critical since it not only allows the aircraft to fly for extended periods of time, but it also enhances payload capacity and reduces stall speeds. Three low Reynolds number airfoils were examined by using XFLR5 and then a novel airfoil was introduced by using optimization process. Definition of novel airfoils specially designed for low-Re high-altitude flight through multi- objective optimization can significantly improve overall aerodynamic performances of HAPS. This multidisciplinary approach also enables the enhancement of particular aerodynamic characteristics, such as lift gradient, maximal lift coefficient, minimal drag coefficient, maximum glide ratio, behavior near stall, etc. When different optimization and computational methods are combined, streamlined geometries with significantly improved aerodynamic efficiencies and lower power demands can be achieved which is exceptionally important for this kind of aircraft. Even though the obtained results should be taken with some reserve (particularly when simpler computational models are employed), significantly greater flexibility in engineering design can be achieved and a large number of possible designs can be analyzed and compared in a relatively short amount of time. A multi- section wing with rectangular inner part is employed in order to increase the useful reference area, which is extremely important for solar panels,

while the reduction of induced drag is achieved by adopting high aspect-ratio wings. In this case, it is recommended to use an airfoil whose maximal relative thickness and curvature are 12.5 % and 5%, respectively, located around the 1st third of the chord length.

Following the design phases that included mass estimation and aerodynamic analysis, structural analysis of the HALE wing was performed. A detailed study on different components of wing structure is also presented in this thesis. At first, in accordance with the contemporary trends in mechanical and aerospace engineering, four different plastic materials obtained through 3D printing techniques were chosen to analyze their mechanical characteristics and then material with the highest tensile strength (PLA) was selected for aging and heat treatment analysis since it can be expected that the wing of a HALE aircraft operates in harsh conditions, with more pronounced variations in temperatures and higher levels of radiation. It was discovered that the mechanical properties of PLA parts decrease with time and are more apparent when the printing resolution is lower, i.e. with a higher layer height. It was particularly intriguing to see the decrease in elastic modulus caused by aging in the 0.3 mm layer specimens because it means that nearly the same deformation may be accomplished with substantially less force. The effect of printing orientation on specimen plasticity has been demonstrated, with the 0/90[°] being the most brittle and the -45/45[°] withstanding the most deformations before break. Though heat treatment increases the strength of the specimens, it was discovered that while it delays the degradation process in the 0.1 mm specimens, it accelerates it in the 0.3 mm specimens. Because there is a lot of uncertainty due to material anisotropy as well as local influence of flaws caused by the printing process, the obtained results should be approached conservatively. Some of these flaws and their effects were discovered during the microscope inspection and are highlighted here as well. Overall, it can be concluded that 3D printed parts can be applied in HALE aircraft if sufficient care/attention is paid to their design, manufacturing and testing.

In continuation, experimental analysis of composite materials based on carbon fibers and epoxy resin is also conducted. Following the completion of the experimental test and examination of the results it was concluded that he orientation of the layers of the composite structure has a significant impact on the mechanical properties' behavior. The precision of the manufacturing process is crucial in the production of composite laminates, i.e. avoiding irregularities in the arrangement of laminates (creating gaps and cracks with inappropriate adhesives, inadequate drying conditions when laying layers, non-automated manufacturing processes), as this reduces load capacity and the quality of the fabricated structure.

Due to the numerous and diverse novel materials and manufacturing techniques (including composites and 3D printed plastics), there is great freedom in designing the HALE wing structure.

However, one should always keep in mind two basic constraints: mass and structural reliability. For structural analyses, 1-way Fluid-Structure Interaction analyses approach was employed, with computed aerodynamic pressures from fluid analyses serving as an input load for the half-wing structural study. To demonstrate the great variety of possible structural designs, two different HALE wing structures were designed and dimensioned. Both considered structures seem sufficiently reliable to bear the operational loads. As expected, rectangular wing 1 is slightly stiffer than the two-segmented wing 2 if stress levels are compared. However, the computed tip deformation of wing 1 is much higher. Supplementary considerations in structural design may involve: manufacturing effort and cost (which would, in this case, be lower for wing 2 since it is constructed from standard and not customized parts) as well as the availability of materials, modal characteristics of the whole (e.g. natural frequencies and oscillation modes, since they affect the way structure responds to disturbances. Here, it was also demonstrated how different inner structures of the two wings affected their dynamic characteristics). Additional options not considered here include other types of fibres (e.g. glass), structures (e.g. sandwich, honeycomb), more resilient plastics or lightweight metal parts.

Regarding the propeller, an important component of the HALE propulsion system that should also possess excellent aerodynamic characteristics as well as being able to carry substantial loads, it is possible to drastically speed up and shorten its conceptual design using the methods given, even though it is based on very simple computational models. It is possible to apply the described aero-structural design method to a wide range of small and large-scale propeller, helicopter, and wind turbine blades as well as wing and tail surfaces, complete aircrafts, etc. with minor modifications and with the same level of success. In addition, the used coupled fluid-structure technique allows for the observation of previously unknown peculiarities and relationships between input and output parameters.

Scientific Contribution

The original scientific contribution of this dissertation is primarily reflected in the complete definition of the appropriate model of high-altitude long-endurance drone wing, which is optimized from the aspects of aerodynamics and structure. However, within this realization, it was necessary to:

- accurately estimate the mass of the aircraft and wing (as its main component),

- perform sizing of solar panels and rechargeable batteries

- define a new airfoil through a multi-criteria optimization procedure and conduct detailed flow simulations of HAPS wing, which improved the aerodynamic efficiency of the main lifting surfaces of the aircraft

- define all the elements of the internal structure of the wing, make the selection of appropriate materials and conduct an experimental examination of the characteristics of the material,

- conduct structural analyses of the wing exposed to the combined action of gravitational and aerodynamic loads,

- define a modern complex propulsion system through the optimization of the propeller for high-altitudes long-endurance aircraft.

Future Work

Regarding future work that may give continuity to the present thesis, the following steps are suggested:

- detailed mass estimation of different parts of the aircraft (e.g. fuselage, empennage, electric motors, equipment) and accurate estimation of center of gravity and all moments of inertia,

- wind tunnel experiment of wing and comparison of the results with the results from CFD simulation,

- experimental analyses of advanced 3D printed plastic and composite materials used in aviation industry,

- further optimization of the design by utilizing “topology optimization” which will probably result in further change to the geometries of both the ribs and spars,

- two-way fluid-structure interaction studies to better understand the behaviour of the assumed thin wing, optimization of its geometric features to reduce negative aeroelastic effects, inclusion of

polyhedral wing, optimization of structural components, selection of the remaining aircraft components, etc.

- structural analyses should be expanded to more complex operational regimes, including unsteady loads (gusts, manoeuvres), as well as aeroelastic occurrences (divergence, control reversal, flutter),

- supplementary extension (augmentation) of the optimization loop by considering the aspects of blade noise, fatigue, manufacturing, maintenance,

- combining CFD simulations with artificial neural networks to make more accurate estimations of propeller aerodynamic performances in real-time, etc.

11. References

[1] "Unmanned Aerial Vehicle (UAV) Market by Point of Sale, Systems, Platform (Civil & Commercial, and Defense & Governement), Function, End Use, Application, Type, Mode of Operation, MTOW, Range, and Region - Global Forecast to 2026." https://www.researchandmarkets.com/reports/5350868 (accessed Sep. 15, 2021).

[2] D. Raymer, *Aircraft Design: A Conceptual Approach, Sixth Edition*. 2018. doi: 10.2514/4.104909.

[3] R. Austin, "UNMANNED AIRCRAFT SYSTEMS UAVS DESIGN, DEVELOPMENT AND DEPLOYMENT."

[4] M. Sadraey, *Unmanned Aircraft Design*. 2010.

[5] R. Abdallah, "Reliability approaches in networked systems : Application on Unmanned Aerial Vehicles," 2019.

[6] "Airbus' solar-powered aircraft Zephyr successfully beams broadband | Daily Mail Online." https://www.dailymail.co.uk/sciencetech/article-10203561/Airbus-solar-powered-aircraft-Zephyr-successfully-beams-broadband.html?ito=1490 (accessed Nov. 18, 2021).

[7] "The History of Solar U.S. Department of Energy, Energy Efficiency and Renewable Energy [Online]." https://www1.eere.energy.gov/solar/pdfs/solar_timeline.pdf (accessed Jul. 10, 2021).

[8] E. E. and R. E. [Online] U.S. Department of Energy, "The History of Solar," *AIP Conference Proceedings,* 2019.

[9] R. J. Boucher and M. Rey, "Sunrise , the World ' s First Solar-Powered Airplane," vol. 22, no. 10, pp. 840–846, 1975.

[10] R. BOUCHER, "Project Sunrise<149>solar-powered aircraft flight demonstration," 1979, doi: 10.2514/6.1979-1264.

[11] R. J. Boucher, A. Flight, M. Rey, A. I. A. R. F. High, A. Airplane, and M. del Rey, "AlAA / SAE / ASME 21 st Joint Protlulsion Conference," 1985.

[12] R. J. Boucher and R. J. Boucher, "A I AA-84-1429 AIAA / SAE / ASME 20th Joint Propulsion Conference," 1984.

[13] a. Noth, R. Siegwart, and W. Engel, “Design of Solar Powered Airplanes for Continuous Flight,” *Environmental Research*, no. 18010, p. 18, 2007, doi: DISS. ETH NO. 18010.

[14] “NASA Armstrong Fact Sheet: Solar-Power Research | NASA.” https://www.nasa.gov/centers/armstrong/news/FactSheets/FS-054-DFRC.html (accessed Sep. 07, 2021).

[15] X. Zhu, Z. Guo, and Z. Hou, “Solar-powered airplanes: A historical perspective and future challenges,” *Progress in Aerospace Sciences*, vol. 71, pp. 36–53, 2014, doi: 10.1016/j.paerosci.2014.06.003.

[16] Y. Gibbs, “NASA Dryden Fact Sheet - Helios Prototype,” 2015.

[17] T. E. Noll, J. M. Brown, M. E. Perez-davis, S. D. Ishmael, G. C. Tiffany, and M. Gaier, “Investigation of the Helios Prototype Aircraft Mishap,” *Volume I Mishap Report*, vol. I, no. January, p. 100, 2004.

[18] G. Romeo, G. Frulla, E. Cestino, and G. Corsino, “HELIPLAT: Design, aerodynamic, structural analysis of long-endurance solar-powered stratospheric platform,” *Journal of Aircraft*, vol. 41, no. 6, pp. 1505–1520, 2004, doi: 10.2514/1.2723.

[19] G. Romeo, M. Pacino, and F. Borello, “First flight of scaled electric solar powered UAV for mediterranean sea border surveillance and forest fire monitoring,” *The Journal of Aerospace Science*, vol. 88, pp. 1–16, 2009.

[20] E. Cestino, “Design of solar high altitude long endurance aircraft for multi payload & operations,” *Aerospace Science and Technology*, vol. 10, no. 6, pp. 541–550, 2006, doi: 10.1016/j.ast.2006.06.001.

[21] S. Neu, “AC Propulsion’s Solar Electric Powered SoLong UAV Alan Cocconi with SoLong at El Mirage Dry Lake in California SoLong landing at the end of its 48 hour flight at Desert Center,” 2005.

[22] “My Ups and Downs with Solar Impulse.” https://www.linkedin.com/pulse/my-ups-downs-solar-impulse-bertrand-piccard (accessed Sep. 09, 2021).

[23] A. Rapinett, “Zephyr: A High Altitude Long Endurance Unmanned Air Vehicle,” *Dissertations*, no. April, pp. 1–83, 2009.

[24] “Zephyr - UAV - Airbus.” https://www.airbus.com/defence/uav/zephyr.html (accessed Apr. 27, 2020).

[25] Airbus Defence & Space, “Zephyr focus of an aircraft. Endurance of a satellite,” p. 2, 2017.

[26] “Zephyr - UAV - Airbus.” https://www.airbus.com/defence/uav/zephyr.html (accessed Sep. 09, 2021).

[27] “BBC NEWS | Science/Nature | Solar plane makes record flight.” http://news.bbc.co.uk/2/hi/science/nature/7577493.stm (accessed Sep. 09, 2021).

[28] “Airbus Zephyr Solar High Altitude Platform System (HAPS) reaches new heights in its successful 2021 summer test flights - Space - Airbus.” https://www.airbus.com/newsroom/press-releases/en/2021/10/airbus-zephyr-solar-high-altitude-platform-system-haps-reaches-new-heights-in-its-successful-2021-summer-test-flights.html (accessed Oct. 24, 2021).

[29] “Vulture.” https://www.darpa.mil/program/vulture (accessed Sep. 13, 2021).

[30] F. A. D’Oliveira, F. C. L. De Melo, and T. C. Devezas, “High-altitude platforms — Present situation and technology trends,” *Journal of Aerospace Technology and Management*, vol. 8, no. 3, pp. 249–262, 2016, doi: 10.5028/jatm.v8i3.699.

[31] “Solara 50 Atmospheric Satellite - Aerospace Technology.” https://www.aerospace-technology.com/projects/solara-50-atmospheric-satellite/ (accessed Sep. 13, 2021).

[32] “Flying Aquila: Early lessons from the first full-scale test flight and the path ahead - Facebook Engineering.” https://engineering.fb.com/2016/07/21/connectivity/flying-aquila-early-lessons-from-the-first-full-scale-test-flight-and-the-path-ahead/ (accessed Sep. 13, 2021).

[33] “PHASA-35 successfully completes critical endurance trials with sensor payload - sUAS News - The Business of Drones.” https://www.suasnews.com/2020/10/phasa-35-successfully-completes-critical-endurance-trials-with-sensor-payload/ (accessed Sep. 13, 2021).

[34] “BAE Plans U.S. PHASA-35 Demonstrations | Aviation Week Network.” https://aviationweek.com/defense-space/space/bae-plans-us-phasa-35-demonstrations (accessed Sep. 13, 2021).

[35] T. C. d’Oliveira, F. A., Melo, F. C. L. D., & Devezas, “High-Altitude Platforms — Present Situation and Technology Trends,” *Journal of Aerospace Technology and Management*, vol. 8, no. 3, pp. 249–262, 2016, doi: 10.5028/jatm.v8i3.699.

[36] A. A. M. Alsahlani, “Design of a Swept-Wing High-Altitude Long-Endurance Unmanned Air Vehicle (HALE UAV),” no. May, p. 289, 2017.

[37] Snorri Gudmundsson, *General Aviation Aircraft Design : Applied Methods*. 2013.

[38] S. P. Aircraft, L. Missiles, and S. Company, “NASA Contractor Report 172313 .,” no. January, 1984.

[39] E. Rizzo and A. Frediani, “A model for solar powered aircraft preliminary design,” *Aeronautical Journal*, vol. 112, no. 1128, pp. 57–78, 2008, doi: 10.1017/S0001924000002001.

[40] D. F. Colas, N. H. Roberts, and V. S. Suryakumar, “Hale multidisciplinary design optimization part II: Solar-powered flying-wing aircraft,” *2018 Aviation Technology, Integration, and Operations Conference*, pp. 1–11, 2018, doi: 10.2514/6.2018-3029.

[41] T. Mcdonnell and A. Ning, “Gradient-Based Optimization of Solar-Regenerative High-Altitude Long-Endurance Aircraft,” pp. 1–10, 2019.

[42] K. Park, J. W. Han, H. J. Lim, B. S. Kim, and J. Lee, “Optimal design of airfoil with high aspect ratio in unmanned aerial vehicles,” *World Academy of Science, Engineering and Technology*, vol. 40, no. July, pp. 182–188, 2009, doi: 10.5281/zenodo.1077456.

[43] R. Mukesh, K. Lingadurai, and U. Selvakumar, “Airfoil shape optimization using non-traditional optimization technique and its validation,” *Journal of King Saud University - Engineering Sciences*, vol. 26, no. 2, pp. 191–197, 2014, doi: 10.1016/j.jksues.2013.04.003.

[44] I. M. Viola, V. Chapin, N. Speranza, and M. E. Biancolini, “Optimal airfoil’s shapes by high fidelity CFD,” *Aircraft Engineering and Aerospace Technology*, vol. 90, no. 6, pp. 1000–1011, 2018, doi: 10.1108/aeat-09-2017-0210.

[45] S. Peigin, N. Pushchin, and S. Timchenko, “Unmanned air vehicle 3-D wing aerodynamical design and algorithm stability with respect to initial shape,” *Thermal Science*, vol. 23, pp. S599–S605, 2019, doi: 10.2298/TSCI19S2599P.

[46] S. A. Brandt, R. J. Stiles, J. J. Bertin, and R. Whitford, *Introduction to Aeronautics: A Design Perspective, Third Edition*. 2015. doi: 10.2514/4.103278.

[47] T. H. G. Megson, *Aircraft Structures for Engineering Students*. 2013. doi: 10.1016/b978-0-08-096905-3.00050-4.

[48] A. Sanchez Ramirez, M. E. Islán Marcos, F. Blaya Haro, R. D’Amato, R. Sant, and J. Porras, “Application of FDM technology to reduce aerodynamic drag,” *Rapid Prototyping Journal*, vol. 25, no. 4, pp. 781–791, 2019, doi: 10.1108/RPJ-09-2018-0251.

[49] X. Zhu, Z. Guo, and Z. Hou, “Solar-powered airplanes: A historical perspective and future challenges,” *Progress in Aerospace Sciences*, vol. 71, pp. 36–53, 2014, doi: 10.1016/j.paerosci.2014.06.003.

[50] J. Jiao, B. F. Song, Y. G. Zhang, and Y. bin Li, “Optimal design and experiment of propellers for high altitude airship,” *Proceedings of the Institution of Mechanical Engineers, Part G: Journal of Aerospace Engineering*, vol. 232, no. 10, pp. 1887–1902, 2018, doi: 10.1177/0954410017704217.

[51] J. Gonzalo, D. López, D. Domínguez, A. García, and A. Escapa, “On the capabilities and limitations of high altitude pseudo-satellites,” *Progress in Aerospace Sciences*, vol. 98, no. March, pp. 37–56, 2018, doi: 10.1016/j.paerosci.2018.03.006.

[52] T. D. Ngo, A. Kashani, G. Imbalzano, K. T. Q. Nguyen, and D. Hui, “Additive manufacturing (3D printing): A review of materials, methods, applications and challenges,” *Composites Part B: Engineering*, vol. 143, no. February, pp. 172–196, 2018, doi: 10.1016/j.compositesb.2018.02.012.

[53] G. Hou, J. Wang, and A. Layton, “Numerical methods for fluid-structure interaction - A review,” *Communications in Computational Physics*, vol. 12, no. 2, pp. 337–377, 2012, doi: 10.4208/cicp.291210.290411s.

[54] P. Wernberg and P. Davidsson, *Fundamentals of Fluid-Structure Interaction Fundamentals of Fluid-Structure Interaction*, no. June. 2009. doi: 10.1007/978-3-211-89651-8.

[55] L. Zhang and C. Sun, “Simulation analysis of fluid-structure interaction of high velocity environment influence on aircraft wing materials under different mach numbers,” *Sensors (Switzerland)*, vol. 18, no. 4, 2018, doi: 10.3390/s18041248.

[56] S. H. Son, B. L. Choi, W. J. Won, Y. G. Lee, C. W. Kim, and D. H. Choi, “Wing design optimization for a long-endurance UAV using FSI analysis and the kriging method,” *International Journal of Aeronautical and Space Sciences*, vol. 17, no. 3, pp. 423–431, 2016, doi: 10.5139/IJASS.2016.17.3.423.

[57] Z. QU and Y. YANG, “Aeroelastic Analysis for the High Altitude Propeller by Using Fluid-Structure Interaction Method,” *Transactions of the Japan Society for Aeronautical and Space Sciences, Aerospace Technology Japan*, vol. 16, no. 3, pp. 236–241, 2018, doi: 10.2322/tastj.16.236.

[58] X. Liu, W. He, and F. Wei, “Design of high altitude propeller using multilevel optimization,” *International Journal of Computational Methods*, vol. 17, no. 4, 2020, doi: 10.1142/S021987621950004X.

[59] A. García-Gutiérrez, J. Gonzalo, D. Domínguez, D. López, and A. Escapa, “Aerodynamic optimization of propellers for High Altitude Pseudo-Satellites,” *Aerospace Science and Technology*, vol. 96, no. December, 2020, doi: 10.1016/j.ast.2019.105562.

[60] “Boeing: Phantom Eye.” https://www.boeing.com/defense/phantom-eye/ (accessed Oct. 18, 2021).

[61] C. L. Nickol, M. D. Guynn, L. L. Kohout, and T. A. Ozoroski, “High altitude long endurance air vehicle analysis of alternatives and technology requirements development,” *Collection of Technical Papers - 45th AIAA Aerospace Sciences Meeting*, vol. 18, no. March, pp. 12653–12669, 2007, doi: 10.2514/6.2007-1050.

[62] “web_globalobserver_bg.jpg (1050×551).” https://www.nasa.gov/sites/default/files/thumbnails/image/web_globalobserver_bg.jpg (accessed Oct. 19, 2021).

[63] “729943main_mcf13-0015-20294_full.jpg (3000×1236).” https://www.nasa.gov/sites/default/files/729943main_mcf13-0015-20294_full.jpg (accessed Oct. 19, 2021).

[64] “339698main_ED96-43785-21_full.jpg (1600×2003).” https://www.nasa.gov/sites/default/files/images/339698main_ED96-43785-21_full.jpg (accessed Oct. 19, 2021).

[65] “Global Hawk - Northrop Grumman.” https://www.northropgrumman.com/what-we-do/air/global-hawk/ (accessed Oct. 19, 2021).

[66] “Bayraktar TB2 Tactical UAV - Army Technology.” https://www.army-technology.com/projects/bayraktar-tb2-tactical-uav/ (accessed Oct. 19, 2021).

[67] “SATCOM aircraft : Heron - Strategic & Tactical Missions MALE UAS.” https://www.iai.co.il/p/heron (accessed Oct. 19, 2021).

[68] “MQ-1B Predator > U.S. Air Force > Fact Sheet Display.” https://www.af.mil/About-Us/Fact-Sheets/Display/Article/104469/mq-1b-predator/ (accessed Oct. 19, 2021).

[69] C. L. Nickol, M. D. Guynn, L. L. Kohout, and T. A. Ozoroski, “High altitude long endurance air vehicle analysis of alternatives and technology requirements development,” *Collection of Technical Papers - 45th AIAA Aerospace Sciences Meeting*, vol. 18, no. March 2007, pp. 12653–12669, 2007, doi: 10.2514/6.2007-1050.

[70] F. Y. Silitonga and M. A. Moelyadi, “Comparative Study of Wing Lift Distribution Analysis for High Altitude Long Endurance (HALE) Unmaned Aerial Vehicle,” *Journal of Physics: Conference Series*, vol. 1005, no. 1, 2018, doi: 10.1088/1742-6596/1005/1/012036.

[71] N. Baldock and M. R. Mokhtarzadeh-Dehghan, “A study of solar-powered, high-altitude unmanned aerial vehicles,” *Aircraft Engineering and Aerospace Technology*, vol. 78, no. 3, pp. 187–193, 2006, doi: 10.1108/17488840610663648.

[72] B. S. de Mattos, N. R. Secco, and E. F. Salles, “Optimal design of a high-altitude solar-powered unmanned airplane,” *Journal of Aerospace Technology and Management*, vol. 5, no. 3, pp. 349–361, 2013, doi: 10.5028/jatm.v5i3.223.

[73] B. Morrisey and R. McDonald, “Multidisciplinary design optimization of an extreme aspect ratio HALE UAV,” *9th AIAA Aviation Technology, Integration and Operations (ATIO) Conference, Aircraft Noise and Emissions Reduction Symposium (ANERS)*, no. September, pp. 1–15, 2009, doi: 10.2514/6.2009-6949.

[74] “solar cell | Definition, Working Principle, & Development | Britannica.” https://www.britannica.com/technology/solar-cell (accessed Dec. 10, 2021).

[75] “Solar Photovoltaic Cell Basics | Department of Energy.” https://www.energy.gov/eere/solar/solar-photovoltaic-cell-basics (accessed Dec. 10, 2021).

[76] B. Parida, S. Iniyan, and R. Goic, “A review of solar photovoltaic technologies,” *Renewable and Sustainable Energy Reviews*, vol. 15, no. 3, pp. 1625–1636, 2011, doi: 10.1016/j.rser.2010.11.032.

[77] “Best Research-Cell Efficiency Chart | Photovoltaic Research | NREL.” https://www.nrel.gov/pv/cell-efficiency.html (accessed Sep. 15, 2021).

[78] “Your questions answered: solar-powered flight | The Engineer The Engineer.” https://www.theengineer.co.uk/your-questions-answered-solar-powered-flight/ (accessed Dec. 11, 2021).

[79] “MicroLink Devices, Inc. - News.” http://mldevices.com/index.php/news (accessed Dec. 11, 2021).

[80] “MicroLink’s solar sheets power Zephyr S UAV maiden flight.” https://www.airforce-technology.com/news/microlink-solar-sheets-zephyr-s-uav/ (accessed Dec. 11, 2021).

[81] Deutsche Energie-Agentur GmbH (dena) German, “Renewables made in Germany,” *English*, 2015.

[82] “PVinsights: Solar PV Principle.” http://pvinsights.com/Knowledge/Principle.php (accessed Dec. 11, 2021).

[83] “Charged EVs | Amprius’s silicon nanowire batteries power the Zephyr S HAPS solar aircraft - Charged EVs.” https://chargedevs.com/newswire/ampriuss-silicon-nanowire-batteries-power-the-zephyr-s-haps-solar-aircraft/ (accessed Dec. 11, 2021).

[84] B. D. Safyanu, M. N. Abdullah, and Z. Omar, “Review of power device for solar-powered aircraft applications,” *Journal of Aerospace Technology and Management*, vol. 11, pp. 1–16, 2019, doi: 10.5028/jatm.v11.1077.

[85] X. Z. Gao, Z. X. Hou, Z. Guo, J. X. Liu, and X. Q. Chen, “Energy management strategy for solar-powered high-altitude long-endurance aircraft,” *Energy Conversion and Management*, vol. 70, pp. 20–30, 2013, doi: 10.1016/j.enconman.2013.01.007.

[86] A. M. S. Mohammad Sakib Hasan, Jelena M Svorcan, “OPTIMAL AIRFOIL DESIGN AND WING ANALYSIS FOR SOLAR-POWERED HIGH-ALTITUDE PLATFORM STATION,” *Thermal Science*, vol. 50, no. 6, p. 241, 2021, doi: doi.org/10.2298/TSCI210419241S.

[87] G. Zubi, R. Dufo-López, M. Carvalho, and G. Pasaoglu, “The lithium-ion battery: State of the art and future perspectives,” *Renewable and Sustainable Energy Reviews*, vol. 89, no. October 2017, pp. 292–308, 2018, doi: 10.1016/j.rser.2018.03.002.

[88] A. A. M. Alsahlani, “Design of a Swept-Wing High-Altitude Long-Endurance Unmanned Air Vehicle (HALE UAV),” University of Salford, 2017.

[89] M. S. Hasan, J. Svorcan, D. Tanovic, G. Baş, and N. M. Durakbasa, “Conceptual Design and Fluid Structure Interaction Analysis of a Solar Powered High-Altitude Pseudo-Satellite (HAPS) UAV Wing Model,” *Lecture Notes in Mechanical Engineering*, vol. 1, pp. 93–105, 2021, doi: 10.1007/978-3-030-62784-3_8.

[90] W. H. Phillips, “Some design considerations for solar-powered aircraft,” 1980.

[91] M. S. Selig and J. J. Guglielmot, “High-lift low Reynolds number airfoil design,” *Journal of Aircraft*, vol. 34, no. 1, pp. 72–79, 1997, doi: 10.2514/2.2137.

[92] “XFLR5.” http://www.xflr5.tech/xflr5.htm (accessed Apr. 30, 2020).

[93] Z. Goraj, “Design challenges associated with development of a new generation UAV,” *Aircraft Engineering and Aerospace Technology*, vol. 77, no. 5, pp. 361–368, 2005, doi: 10.1108/00022660510617086.

[94] B. Allen Gardner and M. S. Selig, “Airfoil design using a genetic algorithm and an inverse method,” *41st Aerospace Sciences Meeting and Exhibit*, no. January, 2003, doi: 10.2514/6.2003-43.

[95] S. N. Leloudas, G. A. Strofylas, and I. K. Nikolos, “Constrained airfoil optimization using the area-preserving free-form deformation,” *Aircraft Engineering and Aerospace Technology*, vol. 90, no. 6, pp. 914–926, 2018, doi: 10.1108/aeat-10-2016-0184.

[96] L. Qiu, R. Wang, X. D. Chen, and D. P. Wang, “Airfoil profile optimization of an air suction equipment with an air duct,” *Thermal Science*, vol. 19, no. 4, pp. 1217–1222, 2015, doi: 10.2298/TSCI1504217Q.

[97] K. Natarajan, S. Thomas, and A. Ramachadran Bhagavathi Ammal, “Numerical investigation of airfoils for small wind turbine applications,” *Thermal Science*, vol. 20, pp. S1091–S1098, 2016, doi: 10.2298/TSCI16S4091N.

[98] I. A. K. Toni D. Ivanov, Aleksandar M. Simonović, Nebojša B. Petrović, Vasko G. Fotev, “INFLUENCE OF SELECTED TURBULENCE MODEL ON THE OPTIMIZATION OF A CLASS-SHAPE TRANSFORMATION PARAMETERIZED AIRFOIL,” *Thermal Science*, vol. 21, pp. 737–744, 2017, [Online]. Available: http://thermalscience.vinca.rs/2017/supplement-3/16

[99] M. Drela, “XFOIL: an analysis and design system for low Reynolds number airfoils.,” *Low Reynolds Number Aerodynamics. Proc. Conf., Notre Dame, U.S.a., June 5-7, 1989 }Edited By T.J. Mueller]. (Lecture Notes in*, no. 54), Berlin, Germany, Springer-Verlag, 1989, pp. 1–12, 1989, doi: 10.1007/978-3-642-84010-4_1.

[100] R. B. Langtry and F. R. Menter, “Transition modeling for general CFD applications in aeronautics,” *43rd AIAA Aerospace Sciences Meeting and Exhibit - Meeting Papers*, no. January, pp. 15513–15526, 2005, doi: 10.2514/6.2005-522.

[101] B. M. Kulfan, “Universal parametric geometry representation method,” *Journal of Aircraft*, vol. 45, no. 1, pp. 142–158, 2008, doi: 10.2514/1.29958.

[102] A. M. Zetina, S. Jeong, and S. Obayashi, “Airfoil aerodynamic optimization for a high-altitude long-endurance aircraft using multi-objective genetic-algorithms,” *2013 IEEE Congress on Evolutionary Computation, CEC 2013*, pp. 2314–2320, 2013, doi: 10.1109/CEC.2013.6557845.

[103] A. Shahrokhi and A. Jahangirian, “Airfoil shape parameterization for optimum Navier-Stokes design with genetic algorithm,” *Aerospace Science and Technology*, vol. 11, no. 6, pp. 443–450, 2007, doi: 10.1016/j.ast.2007.04.004.

[104] D. Beasley, D. R. Bull, and R. R. Martin, “An overview of genetic algorithms : Part 1, fundamentals,” *University Computing*, vol. 2, no. 15, pp. 1–16, 1993.

[105] D. Beasley, D. R. Bull, and R. R. Martin, “An Overview of Genetic Algorithms : Part 2 , Research Topics 1 Introduction 2 Crossover techniques,” *University Computing*, vol. 15, no. 4, pp. 1–15, 1993.

[106] M. S. Selig and B. D. McGranahan, *Wind tunnel aerodynamic tests of six airfoils for use on small wind turbines*, no. October. 2004. doi: 10.2514/6.2004-1188.

[107] ANSYS Inc (Release-15.0), “ANSYS Fluent Theory Guide,” *ANSYS Inc., USA*, vol. 15317, no. January, pp. 1–759, 2015.

[108] Reddy, *MECHANICS of LAMINATED COMPOSITE PLATES and SHELLS Theory and Analysis*, SECOND. 2004.

[109] B. João and J. Miguel, “Design and Optimization of a Wing Structure for a UAS Class I 145 kg A thesis to obtain the Master Degree in Military Science,” no. July, 2017.

[110] G. D. Goh, S. Agarwala, G. L. Goh, V. Dikshit, S. L. Sing, and W. Y. Yeong, “Additive manufacturing in unmanned aerial vehicles (UAVs): Challenges and potential,” *Aerospace Science and Technology*, vol. 63, no. December, pp. 140–151, 2017, doi: 10.1016/j.ast.2016.12.019.

[111] S. Junk and W. Schröder, “Application of sustainable design in additive manufacturing of an unmanned aerial vehicle,” *Smart Innovation, Systems and Technologies*, vol. 52, pp. 375–385, 2016, doi: 10.1007/978-3-319-32098-4_32.

[112] I. S. Pascariu and S. M. Zaharia, “Design and Testing of an Unmanned Aerial Vehicle Manufactured by Fused Deposition Modeling,” *Journal of Aerospace Engineering*, vol. 33, no. 4, p. 06020002, Jul. 2020, doi: 10.1061/(ASCE)AS.1943-5525.0001154.

[113] C. Ferro, R. Grassi, C. Seclì, and P. Maggiore, “Additive Manufacturing Offers New Opportunities in UAV Research,” *Procedia CIRP*, vol. 41, pp. 1004–1010, 2016, doi: 10.1016/j.procir.2015.12.104.

[114] S. Junk, W. Schröder, and S. Schrock, “Design of Additively Manufactured Wind Tunnel Models for Use with UAVs,” *Procedia CIRP*, vol. 60, pp. 241–246, 2017, doi: 10.1016/j.procir.2017.02.027.

[115] B. Rutkay and J. Laliberté, “Design and manufacture of propellers for small unmanned aerial vehicles,” *Journal of Unmanned Vehicle Systems*, vol. 4, no. 4, pp. 228–245, 2016, doi: 10.1139/juvs-2014-0019.

[116] M. S. Hasan *et al.*, “Impact of Aging Effect and Heat Treatment on the Tensile Properties of PLA (Poly Lactic Acid) Printed Parts,” *Materiale Plastice*, vol. 57, no. 3, pp. 147–159, Sep. 2020, doi: 10.37358/MP.20.3.5389.

[117] “Ultimaker 3 FDM 3D Printer : Washington and Lee University.” https://my.wlu.edu/iq-center/equipment/prototyping/3d-printing/ultimaker-3 (accessed Nov. 08, 2021).

[118] M. S. Hasan, “Dimensional Accuracy and Experimental Investigation on Tensile Behavior of Various 3D Printed Materials,” in *INTERNATIONAL SCIENTIFIC CONFERENCE ON DEFENSIVE TECHNOLOGIES*, pp. 1–6.

[119] A. Rodríguez-Panes, J. Claver, and A. M. Camacho, “The influence of manufacturing parameters on the mechanical behaviour of PLA and ABS pieces manufactured by FDM: A comparative analysis,” *Materials*, vol. 11, no. 8, 2018, doi: 10.3390/ma11081333.

[120] AMERICAN SOCIETY FOR TESTING AND MATERIALS, “D638 − 14,” *Standard Test Method for Tensile Properties of Plastics*, p. 17, 2014, doi: 10.1520/D0638-14.1.

[121] A. W. Gebisa and H. G. Lemu, “Influence of 3D printing FDM process parameters on tensile property of ultem 9085,” *Procedia Manufacturing*, vol. 30, no. May, pp. 331–338, 2019, doi: 10.1016/j.promfg.2019.02.047.

[122] B. Banjanin *et al.*, “Consistency analysis of mechanical properties of elements produced by FDM additive manufacturing technology,” *Revista Materia*, vol. 23, no. 4, 2018, doi: 10.1590/s1517-707620180004.0584.

[123] M. Baltić *et al.*, “Investigation of mechanical characteristics of composite plates under tensile loading,” 2020.

[124] “Standard Test Method for Tensile Properties of Polymer Matrix Composite Materials,” *ASTM International*.

[125] G. Belingardi, D. S. Paolino, and E. G. Koricho, “Investigation of influence of tab types on tensile strength of E-glass/epoxy fiber reinforced composite materials,” *Procedia Engineering*, vol. 10, pp. 3279–3284, 2011, doi: 10.1016/j.proeng.2011.04.541.

[126] L. L. Wei *et al.*, “Tensile behaviour of carbon fabric reinforced cementitious matrix composites as both strengthening and anode materials,” *Composite Structures*, vol. 234, no. March 2020, 2020, doi: 10.1016/j.compstruct.2019.111675.

[127] F. Ning, W. Cong, J. Qiu, J. Wei, and S. Wang, “Additive manufacturing of carbon fiber reinforced thermoplastic composites using fused deposition modeling,” *Composites Part B: Engineering*, vol. 80, pp. 369–378, 2015, doi: 10.1016/j.compositesb.2015.06.013.

[128] F. Laurin, P. Paulmier, and F. X. Irisarri, “Determination of the longitudinal compressive strength of a CFRP ply through a tensile test on a laminate,” *Composites Part A: Applied Science and Manufacturing*, vol. 113, no. September 2017, pp. 209–219, 2018, doi: 10.1016/j.compositesa.2018.07.026.

[129] G. Marsh, “Best endurance under the sun,” *Renewable Energy Focus*, vol. 11, no. 5, pp. 24–27, 2010, doi: 10.1016/S1755-0084(10)70111-3.

[130] O. Montagnier and L. Bovet, “Optimisation of a solar-powered high altitude long endurance UAV,” *27th Congress of the International Council of the Aeronautical Sciences 2010, ICAS 2010*, vol. 1, pp. 177–186, 2010.

[131] Ansys MFX, “Advanced FSI Technology: ANSYS MFX Multi-field^{TM} Solver,” pp. 010–4456, 2006.

[132] a. Noth, R. Siegwart, and W. Engel, “Design of Solar Powered Airplanes for Continuous Flight,” *Environmental Research*, no. 18010, p. 18, 2007, doi: DISS. ETH NO. 18010.

[133] J. Morgado, M. Abdollahzadeh, M. A. R. Silvestre, and J. C. Páscoa, “High altitude propeller design and analysis,” *Aerospace Science and Technology*, vol. 45, pp. 398–407, 2015, doi: 10.1016/j.ast.2015.06.011.

[134] P. C. Teixeira and C. E. S. Cesnik, “Propeller effects on the response of high-altitude long-endurance aircraft,” *AIAA Journal*, vol. 57, no. 10, pp. 4328–4342, 2019, doi: 10.2514/1.J057575.

[135] X. Liu and W. He, “Performance Calculation and Design of Stratospheric Propeller,” *IEEE Access*, vol. 5, pp. 14358–14368, 2017, doi: 10.1109/ACCESS.2017.2725303.

[136] C. R. Coe-al, “BEMT Algorithm for the Prediction of the Performance of Arbitrary Propellers,” no. March, 2004.

[137] L. Koch, *Design and performance calculations of a propeller for very high altitude flight*, no. February. 1998. [Online]. Available: http://gltrs.grc.nasa.gov/reports/1998/TM-1998-206637.pdf

[138] J. Tang, X. Wang, D. Duan, and W. Xie, “Optimisation and analysis of efficiency for contra-rotating propellers for high-altitude airships,” *Aeronautical Journal*, vol. 123, no. 1263, pp. 706–726, 2019, doi: 10.1017/aer.2019.14.

[139] D. F. Colas, N. H. Roberts, and V. S. Suryakumar, “Hale multidisciplinary design optimization part I: Solar-powered single and multiple-boom aircraft,” *2018 Aviation Technology, Integration, and Operations Conference*, pp. 1–30, 2018, doi: 10.2514/6.2018-3028.

[140] H. Zhang, B. Song, F. Li, and J. Xuan, “Multidisciplinary design optimization of an electric propulsion system of a hybrid UAV considering wind disturbance rejection capability in the quadrotor mode,” *Aerospace Science and Technology*, vol. 110, p. 106372, 2021, doi: 10.1016/j.ast.2020.106372.

[141] J. Svorcan, S. Hasan, M. Baltić, and A. Simonović, “Optimal Propeller design for future HALE UAV,” *Scientific Technical Review*, vol. 69, no. 2, pp. 25–31, 2019, doi: 10.5937/str1902025s.

[142] J. Svorcan, M. S. Hasan, A. Kovačević, and T. Ivanov, “Design of HALE Propeller through Multi-objective Optimization,” in *AIAA Propulsion and Energy 2021 Forum*, 2021, p. 3730.

[143] A. García-Gutiérrez, J. Gonzalo, D. Domínguez, D. López, and A. Escapa, “Aerodynamic optimization of propellers for High Altitude Pseudo-Satellites,” *Aerospace Science and Technology*, vol. 96, p. 105562, 2020, doi: 10.1016/j.ast.2019.105562.

[144] B. Montgomerie, “Methods for Root Effects, Tip Effects and Extending the ANgle of Attack Range to +- 180, with application to Aerodynamics for Blades on Wind Turbines and Propellers.pdf,” no. June, p. 53, 2004.

Биографија

Mohammad Sakib Hasan, дипл. инж. маш, рођен је 01. марта 1991. године у Тангаилу, Бангладеш. По завршетку средњег образовања у Бангладешу са одличним успехом добио је стипендију Владе Србије у оквиру пројекта „Свет у Србији". Након завршеног курса српског језика на Филолошком факултету, 2011. године уписао је Машински факултет у Београду где је завршио основне (2014. године) и мастер студије на смеру ваздухопловство. Мастер рад насловљен *Концептуални дизајн ултра-лаке летелице „СБ"*, под менторством проф. др Златка Петровића, одбранио је септембра 2017. године са оценом 10, док нешто касније исте године уписује докторске студије.

Током 2016. и 2017. године, обавио је вишемесечне праксе у фирмама Prince Aviation и Air Serbia где је радио на организацији и управљању документима везаним за одржавање ваздухоплова. Све време студија показује склоност ка научно-истраживачком раду као и велику самосталност у истраживању. Такође је члан Ротари клуба и бави се хуманитарним радом. Активни је члан и играчког кадра крикет клуба „Стари Град" (најтрофејнијег клуба у Србији) са којим редовно учествује на такмичењима.

Течно говори бенгалски, енглески и српски језик, а споразумева се и на немачком. Успешно се служи следећим инжењерским софтвером и алатима: ANSYS, MATLAB, XFLR5, XFOIL, PHOTRON, ARAMIS, 3D Printing, CNC Machining, Catia V5, Auto CAD.

Прилог 1.

Изјава о ауторству

Потписан **Mohammad Sakib Hasan**

број индекса **Д41/2017**

Изјављујем

да је докторска дисертација под насловом

Analysis, modeling and optimization of solar-powered high-altitude platform-station (HAPS)

Анализа, моделирање и оптимизација беспилотне летелице за велике висине на соларни погон

- резултат сопственог истраживачког рада,
- да предложена дисертација у целини ни у деловима није била предложена за добијање било које дипломе према студијским програмима других високошколских установа,
- да су резултати коректно наведени и
- да нисам кршио/ла ауторска права и користио интелектуалну својину других лица.

Потпис докторанда

У Београду, 28. 02. 2022

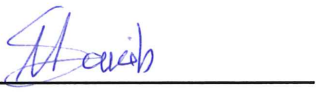

Прилог 2.

Изјава о истоветности штампане и електронске верзије докторског рада

Име и презиме аутора	**Mohammad Sakib Hasan**
Број индекса	**Д41/2017**
Студијски програм	**Докторске академске студије**
Наслов рада	**Analysis, modeling and optimization of solar-powered high-altitude platform-station (HAPS)** **Анализа, моделирање и оптимизација беспилотне летелице за велике висине на соларни погон**
Ментор	**Јелена Сворцан**
Потписан	**Mohammad Sakib hasan**

Изјављујем да је штампана верзија мог докторског рада истоветна електронској верзији коју сам предао/ла за објављивање на порталу **Дигиталног репозиторијума Универзитета у Београду.**

Дозвољавам да се објаве моји лични подаци везани за добијање академског звања доктора наука, као што су име и презиме, година и место рођења и датум одбране рада.

Ови лични подаци могу се објавити на мрежним страницама дигиталне библиотеке, у електронском каталогу и у публикацијама Универзитета у Београду.

Потпис докторанда

У Београду, 28.02.2022

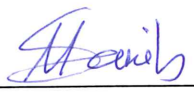

Прилог 3.

Изјава о коришћењу

Овлашћујем Универзитетску библиотеку „Светозар Марковић“ да у Дигитални репозиторијум Универзитета у Београду унесе моју докторску дисертацију под насловом:

Analysis, modeling and optimization of solar-powered high-altitude platform-station (HAPS)

Анализа, моделирање и оптимизација беспилотне летелице за велике висине на соларни погон

која је моје ауторско дело.

Дисертацију са свим прилозима предао/ла сам у електронском формату погодном за трајно архивирање.

Моју докторску дисертацију похрањену у Дигитални репозиторијум Универзитета у Београду могу да користе сви који поштују одредбе садржане у одабраном типу лиценце Креативне заједнице (Creative Commons) за коју сам се одлучио.

(1.) Ауторство

2. Ауторство - некомерцијално

3. Ауторство – некомерцијално – без прераде

4. Ауторство – некомерцијално – делити под истим условима

5. Ауторство – без прераде

6. Ауторство – делити под истим условима

(Молимо да заокружите само једну од шест понуђених лиценци, кратак опис лиценци дат је на полеђини листа).

Потпис докторанда

У Београду, 28.02.2022

Бакић

1. Ауторство - Дозвољавате умножавање, дистрибуцију и јавно саопштавање дела, и прераде, ако се наведе име аутора на начин одређен од стране аутора или даваоца лиценце, чак и у комерцијалне сврхе. Ово је најслободнија од свих лиценци.

2. Ауторство – некомерцијално. Дозвољавате умножавање, дистрибуцију и јавно саопштавање дела, и прераде, ако се наведе име аутора на начин одређен од стране аутора или даваоца лиценце. Ова лиценца не дозвољава комерцијалну употребу дела.

3. Ауторство - некомерцијално – без прераде. Дозвољавате умножавање, дистрибуцију и јавно саопштавање дела, без промена, преобликовања или употребе дела у свом делу, ако се наведе име аутора на начин одређен од стране аутора или даваоца лиценце. Ова лиценца не дозвољава комерцијалну употребу дела. У односу на све остале лиценце, овом лиценцом се ограничава највећи обим права коришћења дела.

4. Ауторство - некомерцијално – делити под истим условима. Дозвољавате умножавање, дистрибуцију и јавно саопштавање дела, и прераде, ако се наведе име аутора на начин одређен од стране аутора или даваоца лиценце и ако се прерада дистрибуира под истом или сличном лиценцом. Ова лиценца не дозвољава комерцијалну употребу дела и прерада.

5. Ауторство – без прераде. Дозвољавате умножавање, дистрибуцију и јавно саопштавање дела, без промена, преобликовања или употребе дела у свом делу, ако се наведе име аутора на начин одређен од стране аутора или даваоца лиценце. Ова лиценца дозвољава комерцијалну употребу дела.

6. Ауторство - делити под истим условима. Дозвољавате умножавање, дистрибуцију и јавно саопштавање дела, и прераде, ако се наведе име аутора на начин одређен од стране аутора или даваоца лиценце и ако се прерада дистрибуира под истом или сличном лиценцом. Ова лиценца дозвољава комерцијалну употребу дела и прерада. Слична је софтверским лиценцама, односно лиценцама отвореног кода.